

HIGHER RESOLUTION STUDIES OF  
JUPITER'S DECAMETRIC RADIO EMISSIONS

By

JAMES RICHARD THIEMAN

A DISSERTATION PRESENTED TO THE GRADUATE COUNCIL  
OF THE UNIVERSITY OF FLORIDA  
IN PARTIAL FULFILLMENT OF THE REQUIREMENTS FOR THE  
DEGREE OF DOCTOR OF PHILOSOPHY

UNIVERSITY OF FLORIDA

1977

To Barbara, my parents,  
and all the others who waited so patiently

## ACKNOWLEDGMENTS

Accolades must begin with Professor Alex G. Smith, my advisor, who suggested the topic of research and then allowed me the freedom to pursue my directions of interest. I have greatly benefited from his expertise not only in scientific endeavors, but also in the realm of technical communication. He has patiently reviewed many offerings by this author, and his suggestions have improved the manuscripts and the English education of the writer. I will greatly miss his guidance when I leave the University of Florida.

The other members of my Supervisory Committee, Thomas D. Carr, George R. Lebo, Stephen T. Gottesman, and Charles F. Hooper, have made the oral examinations enjoyable learning experiences. Their aid throughout my graduate school years will not be forgotten.

I am grateful for the technical assistance rendered in preparation of this dissertation. Woody Richardson has always gone out of his way to supply information on the Florida data collection and to aid in the drafting of the illustrations. In the same way Hans Schrader lent his time and advice in the often difficult photographic tasks. I wholeheartedly recommend Beth Beville as a typist for dissertations. Her typing skill and knowledge of acceptable formats have eased the burden of finishing this work.

Many useful suggestions resulted from discussions with Michael Desch. He has also contributed a large amount of time in the punching and processing of the Texas data. I am also indebted to the radio astronomy group at the University of Texas for the use of their data catalog.

I would like to thank Thomas C. Collins who employed me in my undergraduate years, encouraged me to attend the University of Florida, and continuously provided help and recommendations for furthering my career.

Computing support from the Department of Physics and Astronomy and the Northeast Regional Data Center of the University of Florida was indispensable. I have been fortunate to receive financial assistance and valuable experience in my years as a teaching assistant for the Department of Physics and Astronomy. I am also grateful to the National Science Foundation for financial support as a research assistant on several consecutive grants. Most of all, I thank Barbara for her many years of sustenance both financial and emotional.

## TABLE OF CONTENTS

	PAGE
ACKNOWLEDGMENTS .....	iii
ABSTRACT .....	vi
CHAPTER	
I INTRODUCTION .....	1
1.1 The Decametric Jupiter Puzzle in Plain Language ...	1
1.2 Decametric Jupiter: A Brief Technical Summary .....	6
II THE DATA BASE .....	16
2.1 Introduction .....	16
2.2 University of Florida Data .....	25
2.3 University of Texas Data .....	50
III ONE-DIMENSIONAL STUDIES .....	58
3.1 Histogram Accuracy .....	58
3.2 Decametric Spectral Analysis .....	64
3.3 Source Chronology .....	75
IV TWO-DIMENSIONAL STUDIES .....	97
4.1 Projection Methods and Problems .....	97
4.2 Spectral Analysis .....	102
4.3 Io-Related Source Chronology .....	138
V THEORETICAL IMPLICATIONS .....	154
5.1 Introduction .....	154
5.2 The Source B Anomaly .....	155
5.3 Beaming of the Sources .....	175
5.4 Radiation Obscuration .....	187
5.5 Summary .....	194
LIST OF REFERENCES .....	195
BIOGRAPHICAL SKETCH .....	200

Abstract of Dissertation Presented to the  
Graduate Council of the University of Florida  
in Partial Fulfillment of the Requirements for the  
Degree of Doctor of Philosophy

HIGHER RESOLUTION STUDIES OF  
JUPITER'S DECA-METRIC RADIO EMISSIONS

By

James Richard Thieman

August 1977

Chairman: Alex G. Smith  
Major Department: Physics and Astronomy

Synoptic monitoring of Jupiter's decameter-wavelength emissions over many years has yielded a considerable accumulation of data. This dissertation summarizes an analysis of the data for effects not readily apparent from the study of small subsets of the observations. The data base is a merger of the observations collected by the Universities of Florida and Texas. It is contained on magnetic tape in punched card format and it has been processed into an intermediate form more suitable for direct analysis. Information necessary for use of the raw data and intermediate data magnetic tapes has been provided, as well as details of the variety of punched card formats.

The data in each of ten frequencies in the range from 5.6 to 30 MHz are summarized in histograms of occurrence probability for  $2^\circ$  intervals in System III longitude or the position of Io from superior geocentric conjunction (phase of Io). Apparent in the high-resolution longitude histograms are spectral changes in profile and position of the three probability peaks, often called radio sources A, B, and C. Examination

of the data comprising each source for dependence of occurrence probability on the phase of  $I_0$  reveals asymmetries in the dominant peaks, often accompanied by proximate secondary maxima. High-resolution occurrence probability versus longitude histograms for each apparition of the merged 18, 20, and 22-MHz observations confirm the sinusoidal drift of source A with time, and further studies emphasize the responsibility of the non- $I_0$ -related radiation for this effect. No significant trend of changes in the longitude positions of sources B and C has been found, but the  $I_0$ -related parts of these sources do exhibit a twelve-year cyclic drift in  $I_0$  phase, while source A shows no consistent  $I_0$ -phase motion.

Histograms of occurrence probability calculated for intervals in both longitude and  $I_0$  phase provide a much deeper insight into the source structure. Data at eight frequencies from 10 to 30 MHz have been reduced in this manner, four with interval sizes of  $2^\circ$  by  $2^\circ$  and the other four with  $5^\circ$  resolution in each variable. The diagrams reveal many frequency-dependent changes in the sources, such as the varying appearance of two projections on the lower  $I_0$ -phase side of  $I_0$ -related source B, a bridge of radiation connecting sources A and C through the source B longitudes at lower frequencies, and a large modulation of the source positions and shapes between 15 and 10 MHz. Similar histograms were constructed for the isolated  $I_0$ -related source regions from combined 18, 20, and 22-MHz data for individual apparitions. The connection of the motion of sources B and C in  $I_0$  phase with changes in their morphology is evident from the results.

The phenomena uncovered in the histogram analyses can be compared with theories of beaming of the radiation from the emission region. Few

theories treat this subject in numerical detail, but correspondence of some of the source structure with predictions by McCulloch, Goertz, and Cavaliere and Speranza is found. Calculations of the expected Io-phase and System III longitude angles for which Io-related source radiation will be received on earth have been made using the magnetic field models of Acuna and Ness and Smith et al. in combination with the beaming geometry of the Goldreich and Lynden-Bell theory. In general, agreement with the observed source characteristics is good, but further calculations indicate that more of the high-resolution phenomena can be explained by occultation of the emission regions by the dense Jovian atmosphere near the top of the cloud layer.



## CHAPTER I

### INTRODUCTION

#### 1.1 The Decametric Jupiter Puzzle in Plain Language

Over 20 years ago Burke and Franklin (1955) first realized that the source of interference falling on their new radio telescope was the planet Jupiter. Since that time millions have been spent on observation sites around and above the world to record every facet of the radio noise from Jupiter.

Should the emissions be called noise? Noise implies a hodgepodge of data, a random mixture of the electromagnetic waves. Although Jupiter is certainly not perfectly predictable, it exhibits regularities which make it one of the most interesting paradoxes in the solar system.

All planets emit radio noise as a natural consequence of the thermal motion of their molecules. Jupiter, the sun, the earth, and possibly Saturn show emission far exceeding that explainable by temperature alone. On the earth we know that part of this is due to our communications network and the rest to lightning storms and the interaction of electrons and ions with the earth's magnetic field. Extrapolating this to Jupiter implies the existence of Jovian magnetic fields, lightning storms, and/or intelligent life. Could the emissions be untranslated communication? Since planetary conditions are inhospitable to life as we know it, theories based on natural origins prevail. Some of the characteristics of the radiation, however, seem very unnatural.

Consider the following facts.

1) The excessive radio noise from Jupiter which is detected on earth occurs mostly in the wavelengths around 7-60 meters, referred to as decameter wavelengths. The corresponding radio frequencies are 5-40 megahertz (MHz), which are in the shortwave radio band. It is interesting that these are the bands which are used for our long distance communications. They are very prone to static interference and, sometimes, the swishing sound breaking up communications originates from Jupiter.

Jupiter's decametric radiation is not heard continuously. The probability of receiving it depends on which side of the planet is toward the earth. Unfortunately, the "side" of the planet which faces the earth is not as easily defined as people living on a solid surface would expect. Gaseous orbs, like Jupiter and the sun, rotate at different rates in different latitudes. In the case of Jupiter, a complete rotation takes approximately 9 hours and 50.5 minutes for the equatorial cloud band, and 9 hours and 55.5 minutes for the clouds away from the equator (see Table I-1). The major amount of radio emission occurs regularly at a period close to 9 hours 55.5 minutes, so that at first, the non-equatorial regions seem to be a likely point of origin.

The radio period is a small but significant amount different from that of the cloud bands, however, and very regular. Since the period does not match that of the visible features, this regularity suggests equating the period to that of a rotating, solid object, perhaps the core of Jupiter if one exists. Carrying this further one could speculate that the radio signals may be related to a particular surface area or "side" of the core of Jupiter. This is often called the source region or just a source.

Table I-1  
Important Jovian Parameters

Equatorial Radius	( $R_J$ )	71372 km	(1)
Ellipticity	( $\epsilon$ )	0.06466	(2)
Semimajor Axis of Orbit		5.202803 A.U.	(3)
Eccentricity of Orbit		0.04845	(3)
Sidereal Period		11.86223 yrs	(3)
Synodic Period		398.88 days	(3)
Inclination of Orbit to Ecliptic		1° 18' 17"	(3)
Inclination of Equator to Orbit		3° 5'	(3)
Sidereal Rotation Periods			
System I Epoch 1897.0	( $\lambda_I$ )	9 <sup>h</sup> 50 <sup>m</sup> 30 <sup>s</sup> .003	(4)
System II Epoch 1897.0	( $\lambda_{II}$ )	9 <sup>h</sup> 55 <sup>m</sup> 40 <sup>s</sup> .632	(4)
System III Epoch 1957.0	( $\lambda_{III}$ )	9 <sup>h</sup> 55 <sup>m</sup> 29 <sup>s</sup> .37	(5)
System III Epoch 1965 proposed		9 <sup>h</sup> 55 <sup>m</sup> 29 <sup>s</sup> .711	(6)

#### Satellite Data

Satellite No.	Name	Sidereal Period (days) (4)	Incl. (°) (3)	Ecc. (3)	Orbit Mean Dist. ( $R_J$ ) (3)	Radius (km) (3)
I	Io	1.76986049	0	0.000	5.91	1810
II	Europa	3.55409417	1	0.000	9.40	1480
III	Ganymede	7.16638722	0	0.001	14.99	2600
IV	Callisto	16.75355227	0	0.007	26.38	2360
V	Amalthea	0.49823633	0	0.003	2.54	80

#### References:

- (1) Opp, 1975
- (2) Anderson et al., 1974
- (3) Allen, 1973
- (4) American Ephemeris and Nautical Almanac, 1976
- (5) I.A.U. Information Bulletin, 1962
- (6) Riddle and Warwick, 1976

2) Receiving radiation from certain sides of Jupiter is unusual but not necessarily unnatural. For example, the earth has regions which are more prone to lightning storms. This type of radiation occurs somewhat periodically, but it is not nearly as regular as the radiation from particular source regions of Jupiter. These are considerably enhanced at very regular intervals. Bigg (1964) discovered that the intervals were actually the times when Io, the first Galilean moon, was near one of two positions in its orbit as observed from the earth. If this is not strange enough, the orbital positions at which the enhancements take place are not symmetrical. If we consider the time Io is directly behind Jupiter, as viewed from the earth, as a starting point (i.e., superior geocentric conjunction) then one of the enhancement positions is one-fourth of the way around Io's orbit and the other is two-thirds of the way. Dependence of radio events on the orbital phase of a moon sounds not only unnatural, but astrological.

3) According to Desch and Carr (1974) and Brown (1974a), Jupiter is most active at a frequency of approximately 8 MHz. The earth's ionosphere interferes with observations at frequencies below this value. At higher frequencies, Jupiter's activity drops off at a steady rate—until a value of 39.5 MHz is reached. Beyond this point no abnormal decametric radiation has ever been received.

4) Although not as severe as the earth's  $23.5^\circ$  angle, Jupiter's rotation axis has a  $3^\circ$  tilt so that as Jupiter orbits the sun the northern and southern hemispheres are tipped toward the earth in 12-year cycles. When the northern hemisphere is dominant, radiation is received more often, and the area of the sources appears to be larger. It is as

though the radiation were being beamed like a searchlight from the northern hemisphere and, when this hemisphere is tipped toward the earth, the searchlight is aimed more directly at us. Also, the positions of the radio sources shift slightly in longitude depending upon how much the northern hemisphere is tipped toward or away from the earth.

5) The natural thermal radio noise emitted by a planet is composed of electromagnetic waves having random vibrational directions of the electric and magnetic components. The decametric radiation from Jupiter, however, is polarized so that the vibrations of the electric and magnetic waves appear to move in an elliptical path as the electromagnetic wave propagates toward the observer. For most of the radiation sources the vibrations appear to be right elliptically polarized; that is, they appear to the observer to travel counterclockwise around the elliptical path. For the other source regions the predominant mode is in the opposite sense or left elliptically polarized.

6) The radio signals are not confined to a single frequency. On a loudspeaker connected to a single frequency receiver Jupiter radio storms sound like ocean waves breaking on a shore. These "swishing storms" drift slowly upward or downward in frequency in a manner which depends upon the longitude of Jupiter and often the orbital position of Io as well. At times, events are received which sound like "pops" on a speaker. When slowed down about a hundred times these pops sound more like whistles of rapidly decreasing pitch, usually one right after another. These are detected only when Io and Jupiter are in particular orientations to each other.

Combining all of the six sections together one could argue for Jovian-manned, frequency-modulated radio stations in the northern hemisphere of Jupiter which transmit narrow beams of polarized radiation when Io passes over them. Such a situation is possible, but it is part of man's nature to look for the simplest explanation first. Indeed many plausible theories have explained the above phenomena in terms of the natural ingredients of charged particles and magnetic fields, although so far no one theory has satisfactorily explained everything. The lack of dominance for any particular theory is due partially to the indefinite characteristics of the decametric sources. This allows a wide range of source mechanisms to yield the same general results. The aim of the research presented in this dissertation is to study the source phenomena with higher resolution and so put greater constraints on the theoretical models. The results of this endeavor will be discussed in the following chapters, but first, there is a need to step back and see the overall picture from a more scientific viewpoint.

## 1.2 Decametric Jupiter: A Brief Technical Summary

In order to familiarize the reader with the terms and generally accepted hypotheses in Jovian decametric study the characteristics outlined in the previous section will be presented again in more technical language.

### 1.2.1 Longitude Dependence

The reception of decametric radiation (often referred to as DAM) depends on which Jovian longitude is on the central meridian as viewed from the earth. It should be mentioned that measurement of longitude on Jupiter is based on the definition of  $0^\circ$  longitude coinciding with the

central meridian as viewed from earth at a particular point in time or epoch. Longitude measurement differs from the earth's longitude system in that longitude increases westward from the  $0^\circ$  meridian up to a maximum of  $360^\circ$ . The rotational dependence of activity is normally presented in the form of a histogram, as in Figure I-1. This figure shows the probability of receiving DAM at 22 MHz for each  $5^\circ$  interval of longitude as averaged over the years 1962-1967. The occurrence probability (o.p.) is usually defined as the ratio of the number of activity events to the number of listening times for each histogram interval. Although the histograms change slightly in appearance with frequency and time, Figure I-1 represents a typical plot for the middle decametric frequency range. Labeled A, B, and C in the order of their prominence, the three probability peaks are referred to as sources, although the name implies more individuality than it should. In some of the literature A, B, and C are called the main, early, and late sources. At lower frequencies a fourth source sometimes appears in the  $20^\circ$ - $100^\circ$  longitude range, called appropriately D, or the fourth source.

As mentioned before there is a period, different from the cloud layer rotation periods, which best represents the rotation of the radio sources. The longitude system based on this period is called System III longitude or, symbolically ( $\lambda_{III}$ ). Systems I and II are the optically observed periods of the equatorial and non-equatorial region cloud bands, respectively (see Table I-1). The exact period of  $\lambda_{III}$  has been the subject of much discussion (Carr, 1971; Alexander, 1975; Duncan, 1971; Lecacheux, 1974). At a recent meeting in Tucson, many of those concerned agreed upon a consensus value of  $9^h 55^m 29^s.711$  to be submitted to the International Astronomical Union for adoption as the official System III longitude epoch 1965 to replace the epoch 1957 value of  $9^h 55^m 29^s.37$ .

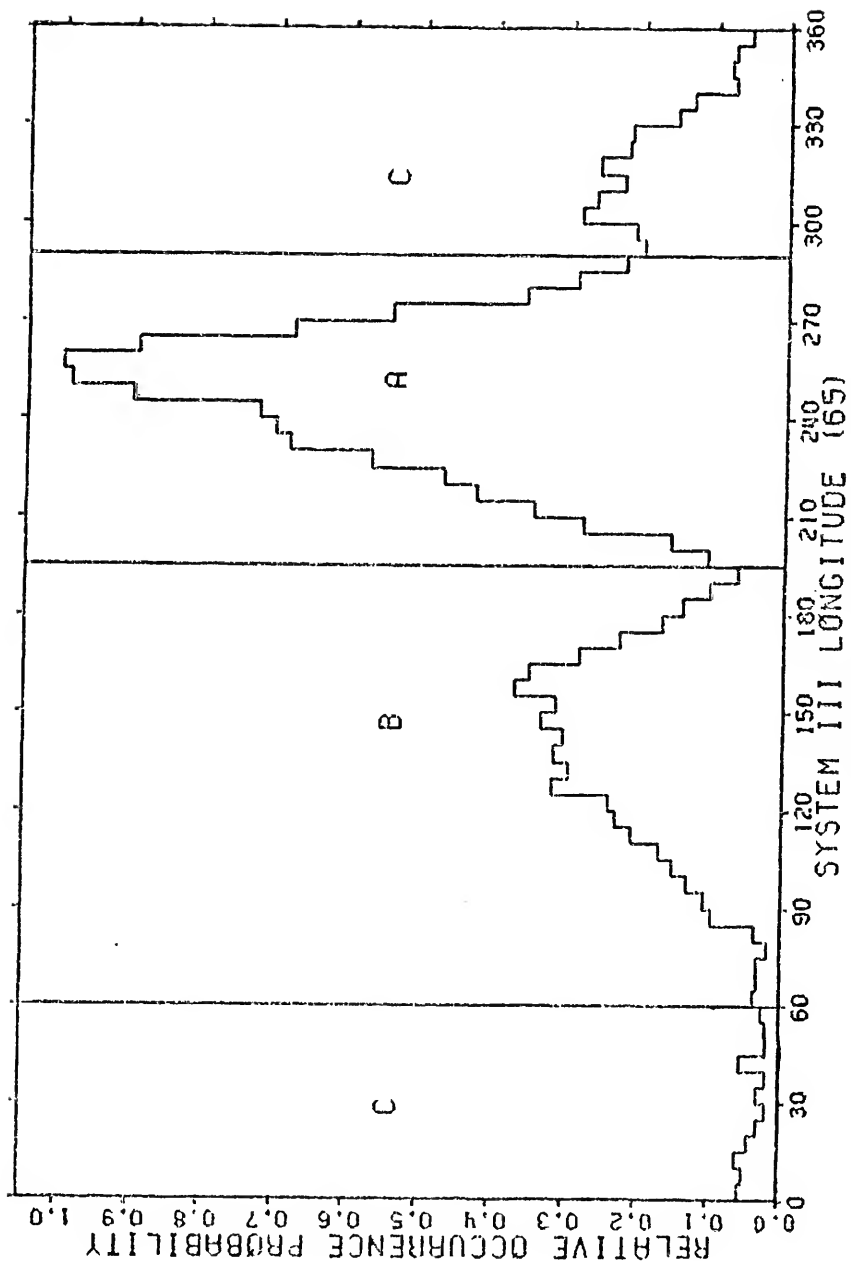


Figure I-1. Histogram of relative occurrence probability of 22-MHz radio storms for 5° intervals in System III Longitude (65) as recorded in Florida during the years 1962-1967.



Since  $\lambda_{III}$  differs from  $\lambda_I$  and  $\lambda_{II}$  the source of the radio signals should not be related to the visible cloud surface. Radio observations in the decimetric (DIM) frequency range (Drake and Hvatum, 1959; Roberts and Ekers, 1966; Berge, 1966; Branson, 1968) indicated the presence of radiating charged particles. Changes in the polarization and intensity of the emission imply the presence of a rotating dipolar magnetic field. The period of this rotation corresponds to the  $\lambda_{III}$  period (Carr, 1971). The particles are apparently trapped by and radiate in a Jovian dipole-like field, which would mean the System III period represents the rotation of the magnetic field. Pioneer 10 and 11 satellite data (Smith et al., 1975; Van Allen et al., 1975) have confirmed that periodic increases in energetic particle intensity were in synchronism with the time of rotation for Jupiter's magnetic field. The magnetic field of Jupiter, like that of the earth, is believed to arise from electric currents circulating deep in the planet. On Jupiter the pressure is sufficient that the currents may be electric charges attached to a rotating solid core of metallic hydrogen. Thus, in their relation to the magnetic field, the radio signals may yield information about the hypothetical solid surface of Jupiter.

### 1.2.2 Io Dependence

By far the most unusual characteristic of DAM is its dependence on the position of the first Galilean satellite, Io, as discovered by Bigg (1964). This dependence is best described by adding a new dimension to the histogram of Figure I-1. Figure I-2 is a smoothed contour plot of 1962-1967, 22-MHz data computed from values of occurrence probability for  $5^\circ$  intervals in System III longitude and the phase of Io from superior geocentric conjunction ( $\phi_{Io}$ ).

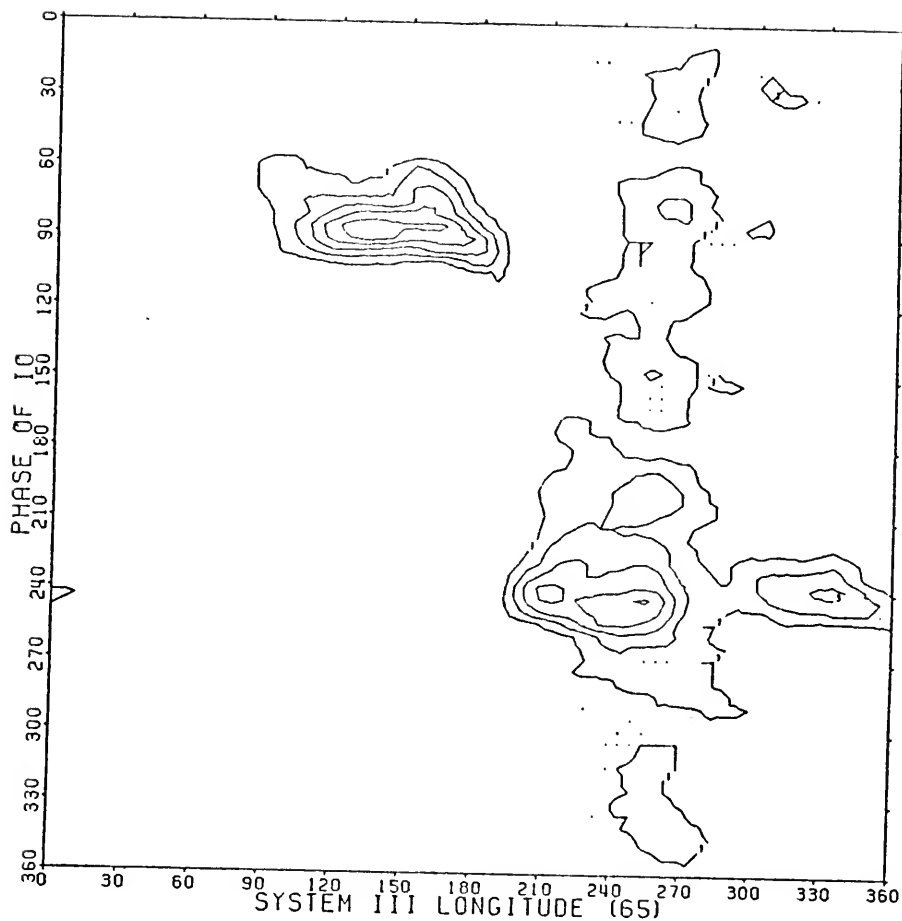


Figure I-2. Smoothed contour plot of the number of radio storms in each  $5^\circ$  interval of System III Longitude (65) and the phase of Io from superior geocentric conjunction. The graph is based on Florida 22-MHz data for the years 1962-1967. The contour interval is 6.

The features in Figure I-2 are typical for the 20-MHz frequency range. The eye is naturally drawn to source B ( $60^\circ < \lambda_{III} < 200^\circ$ ), which is conspicuous in its  $I_o$  dependence. Only when  $I_o$  is near  $90^\circ$  from superior geocentric conjunction, or  $90^\circ$  west of the central meridian as seen from the earth, can source B longitude region emission normally be detected. The source A region ( $200^\circ < \lambda_{III} < 290^\circ$ ) is quite different. Radiation is often received regardless of the position of  $I_o$ , as can be seen from the vertical smear in the A longitudes. This is usually labeled the non- $I_o$ -A radiation. There is an enhancement in the region  $180^\circ < \phi_{I_o} < 270^\circ$  where the occurrence probability is a factor of 4 to 5 larger than the non- $I_o$ -A. This  $I_o$ -A region has the same  $I_o$ -phase dependence as the  $I_o$ -C enhancement just to the right of it. In the C longitudes ( $290^\circ < \lambda_{III} < 360^\circ$ ,  $0^\circ < \lambda_{III} < 40^\circ$ ) there is some non- $I_o$ -related emission, although it is not nearly as prominent as non- $I_o$ -A. Thus, source C is more like B in its isolation. Source D is only seen at frequencies below 18 MHz in the range of  $20^\circ$ - $100^\circ$  of longitude and it is isolated in the  $95^\circ$ - $115^\circ$  region. The other sources also change with frequency, as will be seen in the next section.

### 1.2.3 Source Frequency and Sensitivity Dependence

The two-dimensional histogram changes gradually with frequency. When frequency is increased the  $I_o$ -C source slowly shrinks until it disappears around 26 MHz. The non- $I_o$ -A vanishes at 28 MHz, and the  $I_o$ -A disappears at approximately 36 MHz. Finally, no decametric storms have ever been found to exceed 39.5 MHz (Warwick, 1970). A decrease in frequency brings a decrease in the  $I_o$ -related radiation and a growth in non- $I_o$ -related radiation such that a histogram like that of Figure I-2 would have contours

in all regions. Data below 10 MHz are difficult to acquire because of the increasing opacity of the earth's ionosphere to these frequencies. Satellite studies are beginning to fill in this gap (Brown, 1974b; Desch and Carr, 1974). There is still insufficient data to say much about the dependence of emission on longitude and moon phase at these lower frequencies although some interesting trends have been found. For further details on the satellite dependence of the sources, the summary by Carr and Desch (1975) is excellent.

Bozyan and Douglas (1975) report that they have discovered a separate peak of the non-Io-related radiation in the C region. According to them, there is a distinct non-Io-C source rather than a spillover of the non-Io-A radiation into the C longitudes. If sources A and C each have a non-Io-related component then maybe the other sources do also.

In support of this statement, Desch and Carr (1974) have found a spread of non-Io-B related radiation using a 640-element dipole array at 26.3 MHz. This non-Io-B evidence suggests that each source does indeed have a non-Io-related component which can be detected with sufficiently sensitive apparatus when source B longitudes face the earth.

#### 1.2.4 Twelve-Year Periodicities

The average amount of Jupiter's DAM radiation received on the earth oscillates with a period between 11 and 12 years. At first, this fluctuation seemed to correlate with the eleven year solar activity cycle (Smith et al., 1965), which was reasonable since the sun is a likely candidate as an energy source for DAM. Douglas (1964) and Carr (1962) had already noticed, however, that the rhythm also approximated Jupiter's sidereal period of 11.89 years. Carr suggested

the periodicity could be explained by the changing aspect of Jupiter as seen from the earth, caused by the  $3^\circ$  angle between Jupiter's equatorial and orbital planes. From the point of view of Jupiter this angle is the Jovicentric declination of the earth as symbolized by  $D_E$ . Maximum or minimum activity occurs when the Jovian north pole is pointed toward or away from the earth respectively. The increased activity can be noticed especially in source A. During the active years, the width of the source A occurrence probability peak in  $\lambda_{III}$  coordinates increases, as does the overall reception probability. According to Carr (1972) this indicates a beaming of the DAM from the northern hemisphere such that when this hemisphere is canted toward the earth a greater portion of the radiation beam is received. The previously-mentioned suggestion of a pencil beam radio station in the northern hemisphere is not too far-fetched, although in this case the station appears to have naturally-occurring cyclotron or synchrotron radiation as its source. This is inferred primarily from the polarization of the DAM.

#### 1.2.5 Polarization

The predominant sense of polarization in the source A and B longitude regions is right elliptical or right circular (Kennedy, 1969). This is consistent with the theory of cyclotron or synchrotron radiation beamed from the northern hemisphere in the extraordinary mode (Dulk, 1965). The magnetic field of Jupiter has the opposite sense to that of the earth, and the field in the northern hemisphere will be pointing out of the planet and toward the earth-bound viewer. In the same manner, sources C and D, which are predominantly left elliptically polarized, are speculated to originate in the southern hemisphere. The polarization argument does

not preclude the sources from being in either hemisphere or even far away from Jupiter's surface, but this evidence, together with the magnetic field values to be discussed later, make a convincing argument for assuming sources A and B come from the northern half of Jupiter.

#### 1.2.6 Dynamic Spectra

The simplest approach to the study of DAM makes use of narrow-band receiving equipment. A single Jupiter storm usually covers a wide range of frequencies; however, and a wealth of information can be gained from broad-band antennas and receivers. This is especially true when the storms are examined with high time resolution. These analyses generally involve very small subsets of the data base. Since this dissertation is concerned mainly with large volumes of narrow-band data, only a brief mention of the field of dynamic spectra study will be made.

Jupiter radiation can be divided into the categories of long and short events or L-bursts and S-bursts. The L-bursts are events of relatively long duration compared to S-bursts, usually on the order of several seconds. These were mentioned previously as "swishing" storms. The swishing sound comes from the reception of a succession of L-burst waves by narrow bandwidth equipment. The appearance of modulation lanes in adjacent waves or envelopes indicates that they were once part of a continuous disturbance (Riihimaa, 1974). The separation into envelopes occurs in interplanetary space where solar plasma winds perturb the DAM waves (Douglas and Smith, 1967). Although the L-bursts drift up and down in frequency at a rate of a few MHz/sec, the modulation lanes within L-bursts have drift rates around 100 kHz/sec. The rate and direction of

frequency drift correlate with the longitude of the central meridian and the position of Io (Warwick, 1967).

On a loudspeaker connected to a narrow-band receiver, S-bursts are millisecond-length events often described as spitting, although percolating might be more acoustically accurate. The tendency for S-bursts to come in groups results in a repetitive popping noise. With high time resolution the pop is seen to result from the combination of narrow instantaneous bandwidth and rapid frequency drift. The drift is always negative and proportional to frequency. The S-bursts have been observed only during Io-controlled storms, especially in the B and C longitude regions. For more detailed information on the dynamic spectra phenomena the summary by Carr and Desch (1975) is a good starting point.

Jupiter radio astronomy basics have now been presented both speculatively and technically. Chapters III and IV will expand the previous discussion of Sections 1.2.1-1.2.4, while the material in Sections 1.2.5 and 1.2.6 must be considered in the theory discussion of Chapter V. For the moment let us digress from the fundamental facts to the basis for these facts, namely the data.

## CHAPTER II

### THE DATA BASE

#### 2.1 Introduction

Despite the accumulation of many astute theories, none of them can as yet satisfactorily explain all of the quirks inherent in the Jovian radiation process. Part of the problem in establishing a comprehensive theory of Jovian radiation is the intermittent behavior of the radio events. Their nature changes not only with the rotation of Jupiter and the phase of Io, but also with the 11.86 year orbital period of Jupiter. Therefore, two decades of radio monitoring have yielded only about two cycles of data. This is complicated by the fact that ground-based decametric radio observations are favorable only during ionospherically quiescent times, usually the late nighttime hours. The irregularity of good conditions for reception together with the periodicities make it difficult for any single observing site to get an overall picture of Jupiter's activity.

The obvious step of combining the data from several observatories fills in some of the gaps and gives a better statistical representation of the emission pattern. Several institutions such as NASA and the Universities of Texas and Florida have helped to establish multiple observing sites for this purpose. Some individuals have accomplished the same result by merging data obtained from separate groups. Duncan (1971) gathered one of the most comprehensive collections of the earliest



years of Jupiter decametric observation. Although his list of observing groups is extensive, the amount of data is small since most of the groups listed observed only in the mid-1950's. Intensive synoptic monitoring of Jupiter did not begin until the late fifties and early sixties, during the rising segment of the Jupiter activity cycle.

The amount of decametric data swelled geometrically in the mid-sixties because of increased government support as well as the rise in Jovian emission probability. Exhaustive collections of observations have, therefore, become difficult to establish. Duncan includes only small subsets of the data from groups observing in the sixties, since he was interested in studying only the higher frequencies. In most cases recent publications have used the data acquired by a single group.

This dissertation is based upon a combination of surveillance gathered by groups at the Universities of Florida and Texas. The University of Florida has collected data from sites in Maipo and Huanta, Chile, as well as from its own observatories in Florida. In the interest of brevity, this assemblage will often be referred to as Florida data. Likewise, the term Texas data will mean the catalogued collection (Bozyan, et al., 1972) of data from observatories at the University of Texas, Yale, and Kodaikanal, India. Both Florida and Texas began synoptically monitoring Jupiter around 1957. Both have continued to accumulate observations up to the present time from many widely-spaced sites, so that the collection from just these two institutions involves over 145,000 hours of data. Figures II-1 and II-2 are plots of the listening and storm times through all the years and for all frequencies. The four-character codes along the ordinate axis are the data set names. These names are listed in Table II-8 and are derived from the card codes explained in Table II-1.

Figure II-1. Plot of listening and storm times for all Florida and Chile 5° intermediate data cards on magnetic tape. The codes on the ordinate axis are interpreted in Table II-1. The vertical lines are placed along the Julian data axis at the times of Jupiter's conjunction with the sun. See Figure II-3 for an explanation of the horizontal bands.

[illegible]

Figure II-2. Plot of listening and storm times for all Texas intermediate data on magnetic tape. The codes on the ordinate axis are interpreted in Table II-1. The vertical lines are placed along the Julian date axis at the times of Jupiter's conjunction with the sun. See Figure II-3 for an explanation of the horizontal axis.

JULIAN DATE (24...) 2000 197000

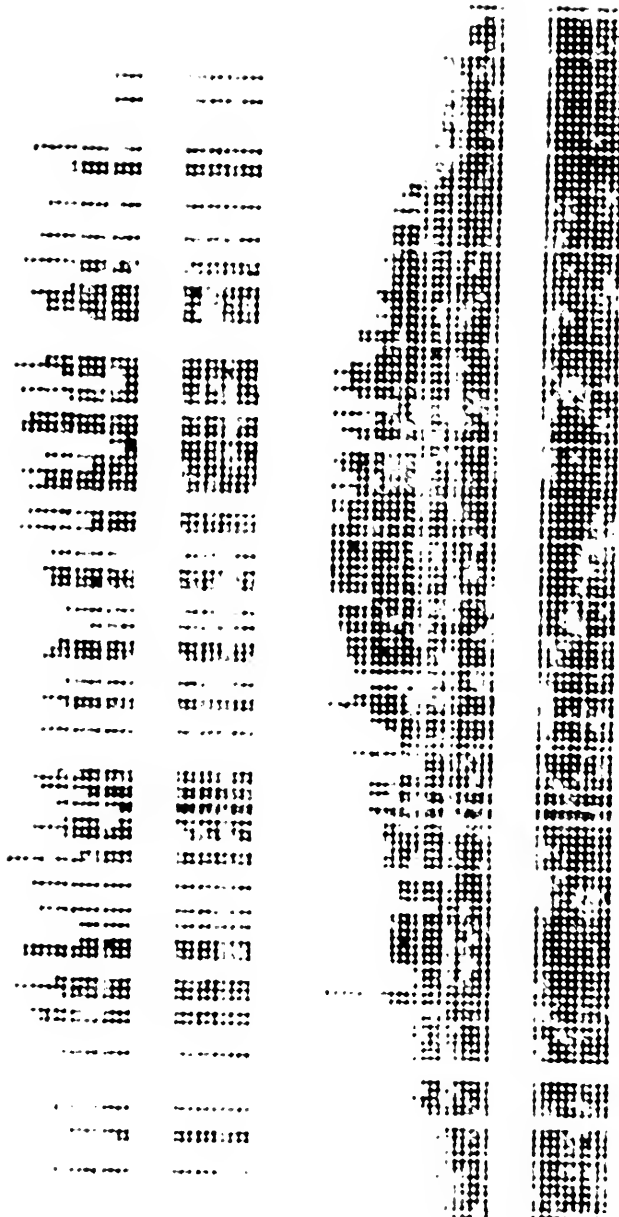
The data are plotted according to Julian date and separated into apparitions by vertical lines representing Jupiter's times of conjunction with the sun.

Figure II-3 shows a blowup from Figure II-1 of one apparition for one frequency. The fine detail reveals that the graph is made of electrostatically printed dots of 0.01 inch diameter produced by a Gould plotter. The four horizontal bands can be divided into the two upper bands which present information on activity, and the two lower bands concerning listening times. The horizontal axis is the time axis, and in order to keep the plot dimensions reasonable, each vertical line of dots represents the maximum listening and storm times for two consecutive Julian dates. If there was any listening time on either of the two days there will be a vertical line of dots in the lowest horizontal band. The band above it represents the maximum listening time for either of the two days by a vertical line of from 0 to 20 dots. The number of dots is directly proportional to the amount of listening time from 0 to 600 minutes. In the same way, the two activity bands give first the presence of activity, and then a line of 0 to 20 dots proportional to the logarithm of the maximum activity from 0 to 600 minutes. The logarithm was used since the amount of activity for a given date varies greatly among the frequencies.

The rest of this chapter will describe the initial processing and characteristics of the data base. First, the data gathered by the University of Florida will be examined.

Figure II-3.

An enlargement of the F2Y, 1965-1966 section of Figure II-1. Each vertical line of dots represents two consecutive Julian dates. The presence of a vertical line in the lowest horizontal band means observations were made on either or both dates. The larger of the two days' observing time is proportional to the length of the vertical line in the horizontal band second from the bottom. In a similar way, the presence of Jupiter radio events and the logarithm of the larger amount of activity for the two-day period are represented in the upper two horizontal bands.





## 2.2 University of Florida Data

### 2.2.1 Initial Processing

The means of processing the Florida data has not changed significantly since the early sixties. All of the observations from Florida as well as those from Chile have been reduced according to the method described below. There are some nonuniformities in the processed data which will be listed later.

Signals from the radio receiving systems are recorded on roll charts either directly or through the intermediary of magnetic tape. The observer aurally distinguishes Jupiter storms from interference and marks them as such. Upon reduction, any activity on the records is divided into five-minute intervals to facilitate recording changing storm patterns. According to the format of Table II-1, the time and characteristics of the storm within each interval are punched on a computer card. Observation times having no Jupiter activity are summarized on a single card. As can be seen, most of the card is used for calibration data in order to obtain flux density information on the storm.

In 1973, a 640-element phase-steerable dipole array operating at 26.3 MHz was completed at the University of Florida (Desch and Carr, 1974). The many differences between the new array and the older receiving equipment made a different raw data card format more convenient. Table II-2 explains the format used for that situation.

The actual determination of the longitude of Jupiter and the phase of its satellites for the listening and storm times, in addition to the flux density calculation for each storm interval, was done by a program developed by H.I. Register (1968). The program figures planetary and satellite orientation using information from the appropriate day's

Table II-1  
Raw Data Card  
Florida Card

0000	Year
0000	Month
0000	Day
0000	Listening beginning time - hours (1)
0000	" " " - minutes "
0000	" ending " - hours "
0000	" " " - minutes "
0000	Activity beginning time - hours
0000	" " " - minutes
0000	" ending " - hours
0000	" " " - minutes
0000	Galactic background level - percent of full scale
0000	Largest Jupiter pulse - percent of full scale
0000	Quality of data - 0, certain; 1, probable; 2, possible
0000	Calibration input step No. 1 - dB
0000	" " " " 2 - "
0000	" " " " 3 - "
0000	" " " " 4 - "
0000	" " " " 5 - "
0000	" " " " 6 - "
0000	System response to cal. step No. 1 - percent of full scale
0000	" " " " " " 2 - " " " "
0000	" " " " " " 3 - " " " "
0000	" " " " " " 4 - " " " "
0000	" " " " " " 5 - " " " "
0000	" " " " " " 6 - " " " "
0000	Number of calibration steps (2)
0000	Cal. step matching output of standard noise diode - dB
0000	Code identifying calibrator in use (3)
0000	Flux density matching standard noise diode - $10^{-22}$ watts/m <sup>2</sup> -Hz
0000	Code indicating baseline of measurement (4)
0000	Code indicating meaning of date on card (5)
0000	Difference between times on card and Universal Time - Hours
0000	Card code (6)

FORTRAN Format (11I2,2PF2.0,0PF3.2,11,6F3.1,2P6F3.1,11,0PF3.2,  
11,F4.2,3I1,A4)

Notes for Table II-1:

- (1) These fields may be blank, indicating the listening time is the same as the corresponding activity time. This method is used for long continuous storms, usually in the later years.
- (2) This field has been neglected in the later years.
- (3) For further information on calibrators consult Miller (1970), Register (1968), and Lebo (1964).
- (4) A 0 indicates measurement from the galactic level and a 1 signifies use of the recorder baseline.
- (5) For code 1 observation periods extending through midnight cards are often punched with the second day's calendar date. Code 0 cards should be split at midnight to avoid this problem.
- (6) The card code is a four character field containing information on the observing site, frequency, and type of antenna according to the following format:

1st character - observing site

F - Florida  
 H - Huanta, Chile  
 K - Kodaikanal, India  
 M - Maipu, Chile  
 T - Texas  
 Y - Yale

2nd and 3rd characters - frequency

05 or 5 - 5.6 MHz  
 10 - 10.0 MHz  
 12 - 12.5 MHz  
 13 - 13.1 MHz  
 15 - 15.0 MHz  
 16 - 16.0 MHz for Maipu, Chile and 16.7 MHz for  
       Texas or Yale  
 18 - 18.0 MHz  
 19 - 19.2 MHz  
 20 - 20.0 MHz  
 22 - 22.2 MHz  
 23 - 23.0 MHz  
 25 - 25.2 MHz  
 26 - 26.3 MHz  
 27 - 27.6 MHz  
 30 - 30.0 MHz

4th character - antenna type

A - array  
 B - broadside  
 H - dual full-wave dipoles in an H pattern,  
       essentially a broadside  
 I - interferometer  
 P - polarimeter  
 S - south half of interferometer only  
 Y - Yagi

FORTTRAN Format (2I2,4(2I2,2X),2I1,F4.1,1X,F4.1)

Notes for Table II-2:

## (1) Character of storm:

1 - S bursts; spitting

2 - L bursts; swishing

3 - scintillating; period greater than 30 sec.

ephemeris card (Table II-3). Each raw data card is converted on a one-to-one basis into an intermediate data card structured according to Table II-4. The position of Jupiter and its satellites is expressed in zones rather than degrees. For the cards using the format of Table II-4 each zone represents a  $5^\circ$  segment of orbit or longitude. In later years, and in reprocessing some of the data from earlier years, the card format was modified to that of Table II-5, which eliminates some unimportant fields and adds information on the newly-proposed System II longitude epoch 1965 (see Table I-1). With  $5^\circ$  zones, orientation can be expressed in two digits, allowing more room for other information. At first, with a small amount of data, accuracy within  $5^\circ$  was sufficient. With time the storm counts in each zone accumulated to the point where smaller zones would be statistically significant and therefore desirable.

Leacock (1971) modified the Register program to replace the  $5^\circ$  zones with  $2^\circ$  zones. The modified intermediate data card (Table II-6) contains less information on the outer Galilean satellites, but the increased positional accuracy led to several discoveries which will be discussed later. Why weren't  $1^\circ$  or even smaller zones used, since three card columns would be needed in each case? As mentioned before, storm characteristics are recorded in five minute intervals. In particular, the flux density calculations are an average for the storms in each interval. Jupiter rotates through  $2^\circ$  in approximately 3.3 minutes. The accuracy of the data reduction, therefore, put a natural limit on zone size, in the range of  $2^\circ$ . This number is used as a compromise giving good positional information without stretching the accuracy of the reduction process too far.



Notes for Table II-3:

- (1) Invalid day numbers such as 00 and 32 were included in the early years for extrapolation purposes.
- (2) The first two digits of the Julian date are always 24 and are excluded in the FORTRAN format.
- (3) These fields are often filled with zeroes in the early years at times near the conjunction of Jupiter and the sun or when no observations were made.
- (4) Prior to 1961 System II longitude was used.
- (5) The abbreviation s.g.c. stands for superior geocentric conjunction. These values are uncorrected for light time through 1967.
- (6) After 1967 these fields are not used.
- (7) These data were included starting in 1970. Times are expressed according to Eastern Standard Time.

The data set containing all of the ephemeris cards (currently up to 1975) is at the end of tape volumes JRID1 and JRID2. The data set name is EPH and the number is 48.



FORTRAN Format (A4,3I2,I5,24I2,1X,I1,1X,F7.2,5X,2I1)

Notes for Table II-4:

- (1) For card code, see Table II-1.
- (2) The abbreviation s.g.c. stands for superior geocentric conjunction.
- (3) In some years data for Jovian moon V, Amalthea, were substituted in the Europa fields. Table II-8 lists the exceptions.
- (4) Activity greater than 9 minutes often occurs in the early years or as a result of errors in the data. The result is an asterisk in column 65. In some of the earlier apparitions the asterisks have been replaced by zeroes.
- (5) All of the data listed in Table II-8 have been reduced geocentrically.

FORTTRAN Format (A4,3I2,I5,24I2,1X,I1,I2,F6.2,3I2)

Notes for Table II-5:

- (1) For card code, see Table II-1.
- (2) The abbreviation s.g.c. stands for superior geocentric conjunction.
- (3) Activity greater than 9 minutes sometimes occurs resulting in an asterisk in column 65.
- (4) The flux density field is smaller than the field used in the early years format. A greater frequency of field overflows, and therefore asterisks, is to be expected.

Card Code (1)  
Year  
Month  
Day  
Julian Date - 24 \_\_\_\_\_  
System III Longitude - listening beginning zone (2)  
" " " " ending " "  
" " " " activity beginning " "  
" " " " ending " "  
Position of Io from s.g.c. - listening beginning zone (3)  
" " " " " " ending " "  
" " " " " activity beginning " "  
" " " " " ending " "  
Sub-Io System III Longitude - listening beginning zone (2)  
" " " " " ending " "  
" " " " activity beginning " "  
" " " " ending " "  
Length of activity in minutes  
Maximum flux density for activity -  $10^{-22}$  watts/m<sup>2</sup>-Hz (4)  
Quality of data - 0, certain; 1, probable; 2, possible  
Basis for angular measurement - 0, geocentric; 1, heliocentric (4,5)

FORTTRAN Format (A4,3I2,I5,12I3,11X,I3,1X,F7.2,5X,2I1)

Notes for Table II-6:

- (1) For card code, see Table II-1.
- (2) These fields may be in epoch 1957.0 or epoch 65 coordinates depending on the data set used. See Table II-8 for listing of data sets.
- (3) The abbreviation s.g.c. stands for superior geocentric conjunction.
- (4) These fields are not used in epoch 65 data.
- (5) All of the data listed in Table II-8 are reduced geocentrically.

Desch developed the program to produce the 26-MHz array intermediate cards from the raw data cards. Again, the characteristics of the array make more desirable an intermediate card format differing from that of the other frequencies (Table II-7). For example, the sensitivity of the array can result in storm times greater than 100 minutes, requiring three card columns for storm length. Also, increased accuracy in data reduction permitted the use of  $1^\circ$  zones.

### 2.2.2 Data Characteristics

Almost 20 years of observation have yielded over 80,000 raw data cards and an even larger number of intermediate cards. Such a profusion of cards made multi-year analyses quite difficult. In 1973, the obvious step of organizing and loading the data onto magnetic tape was completed. The raw data cards have been placed on tape volume JRRD1 (Jupiter Radio Raw Data #1). JRID1 (Jupiter Radio Intermediate Data #1) was the name selected for the intermediate card tape volume. JRID2 is an exact copy of JRID1.

The cards had been produced by many people over the long span of years. As can be expected, they are not uniform in their content since the information they contain reflects what was considered important at the time of their generation. Table II-8 summarizes the characteristics of the data contained on the tapes. An overall summary for each frequency is shown in Table II-9.

To access any of the data sets listed in Table II-8 it is necessary to know the local tape file management system. For the IBM 370/165 computer at the Northeast Regional Data Center (NERDC), the following three data definition cards are suggested for reading from any of the three tape volumes:

Table II-7  
Intermediate Data Card  
Florida 26.3 MHz Data - 1° Zones

0000	Card code (1)
0000	Year
0000	Month
0000	Day
0000	Julian Date - 24 _____
0000	System III Longitude (57.0) - listening beginning zone
0000	" " " " " ending "
0000	" " " " activity beginning "
0000	" " " " " ending "
0000	Position of Io from s.g.c. - listening beginning zone (2)
0000	" " " " " ending " "
0000	" " " " " activity beginning " "
0000	" " " " " ending " "
0000	Position of Europa from s.g.c. - listening beginning zone (2)
0000	" " " " " ending " "
0000	" " " " " activity beginning " "
0000	" " " " " ending " "
0000	Position of Ganymede from s.g.c. - listening beginning zone (2)
0000	" " " " " ending " "
0000	" " " " " activity beginning " "
0000	" " " " " ending " "
0000	Length of activity in minutes
0000	Maximum flux density for activity - Janskys
0000	Character of storm (3)
0000	Credibility - 1, certain; 2, probable; 3, possible
0000	Basis for angular measurement - 0, geocentric; 1, heliocentric (4)

FORTTRAN Format (A4,3I2,I5,17I3,1X,F6.0,4X,3I1)



Notes for Table II-7:

- (1) The card code is F26A. See Table II-1 for an explanation of the code.
- (2) The abbreviation s.g.c. stands for superior geocentric conjunction.
- (3) Character of storm:
  - 1 - S bursts; spitting
  - 2 - L bursts; swishing
  - 3 - scintillating; period greater than 30 seconds
- (4) All of the 26.3-MHz data listed in Table II-8 are reduced geocentrically.

Table II-8  
Characteristics of Florida Data on Magnetic Tape

DSN (1)	C.C. (2)	Dates (3)	Raw Data			5° Data			2° Data		
			DS# (4)	Ca1 (5)	Q (6)	DS# (4)	Flx (7)	Q (6)	DS# (4)	Flx (7)	Q (6)
M05	M05	4/19/61- 8/ 7/61	1			13		x			
"	M 5B	6/14/62-11/26/62	"	x	x	"		x			
"	"	5/25/63-10/ 2/63	"	x	x	"		x			
M10	M10	3/ 4/61- 9/13/61	2			14					
M10	M10B	5/ 8/62-12/ 7/62	"	x	x	"		x			
"	"	5/18/63- 1/20/64	"	x	x	"		x			
"	M10P	8/ 7/64- 1/26/65	"			"					
"	M10B	9/19/65- 1/12/66	"	x	x	"		x			
H10I	H10I	10/11/65- 1/ 3/66	3	x	x	15		x			
F10P	F10P	8/26/65- 3/31/66	4			16					
"	"	10/20/66- 2/27/67	"	x	x	"		x			
F12H	F12H	10/16/65- 4/ 3/66	5	x	x	17		x			
"	"	10/28/66- 3/ 5/67	"	x	x	"		x			
M13P	M13P	5/ 7/74-11/15/74	6	x	x	18	x		x		
M15	M15	3/18/61-11/ 1/61	7			19					20
"	M15B	4/ 1/62-12/20/62	"	x	x	"		x			"
F15Y	F15C	3/ 4/61- 1/10/62	8			21					23
"	"	6/17/62-12/31/62	"	x	x	"	x	x	22	"	"
"	"	5/31/63- 2/11/64	"	x	x	"	x	x	"	"	"
"	F15Y	6/28/64- 4/30/65	"	x	x	"	x	x	"	"	"
"	"	7/15/65- 4/30/66	"	x	x	"	x	x	"	"	"
"	"	9/ 2/66- 4/11/67	"	x	x	"	x	x	"	"	"

Table II-8 - continued.

DSN (1)	C.C. (2)	Dates (3)	Raw Data			5° Data			2° Data		
			DS# (4)	Cal (5)	Q (6)	DS# (4)	Flx (7)	Q (6)	DS# (4)	Flx (7)	Q (6)
F15Y	F15Y	10/10/67- 4/10/68	8	X	X	21	X	X	22		23
"	"	10/23/68- 3/25/69	"	X	X	"	X	X	"		"
"	"	2/ 8/72- 6/18/72	"	X		"	X		"		"
"	"	3/12/73-12/25/73	"	X		"	X		"		"
M16	M16Y	3/22/60- 8/ 6/60	9			24					
"	"	8/19/65- 9/30/65	"		X	"		X			
"	M16P	10/ 1/65- 3/30/66	"		X	"		X			
"	"	9/ 2/66- 4/15/67	"	X	X	"	X				
"	"	10/ 8/67- 5/10/68	"	X	X	"	X	X			
"	"	12/23/69- 7/ 6/70	"	X	X	"	X	X			
"	"	6/19/73-10/27/73	"	X	X	"	X	X			
"	"	5/ 7/74-11/15/74	"	X	X	"	X	X			
M18Y	M18Y	2/19/60- 8/ 6/60	10			25					26
"	"	2/12/61-11/19/61	"			"					"
"	"	4/ 1/62-12/20/62	"	X	X	"		X			"
"	"	5/ 9/63- 1/25/64	"	X	X	"		X			"
"	"	10/ 1/64- 2/11/65	"		X	"		X			"
"	"	9/ 3/65- 3/29/66	"		X	"		X			"
"	"	9/ 2/66- 4/13/67	"	X	X	"		X			"
"	"	10/ 3/67- 5/10/68	"	X	X	"	X				"
"	"	11/ 5/68- 6/20/69	"	X	X	"	X	X			"
"	"	12/10/69- 7/ 6/70	"	X	X	"	X	X			"
"	"	1/20/71- 8/16/71	"	X	X	"	X	X			"
"	"	3/30/72- 9/ 1/72	"	X	X	"	X	X			"
"	"	4/27/73-10/27/73	"	X	X	"	X	X			"
"	"	5/ 7/74-11/16/74	"	X	X	"	X	X			"

Table II-8 - continued.

DSN (1)	C.C. (2)	Dates (3)	Raw Data			5° Data			2° Data		
			DS# (4)	Ca1 (5)	Q (6)	DS# (4)	Flx (7)	Q (6)	DS# (4)	Flx (7)	Q (6)
H18Y	H18Y	6/18/64- 2/15/65	11	x	x	27		x			28
"	"	10/11/65- 3/29/66	"	x	x	"		x			"
F18Y	F18B	1/ 1/57- 4/28/57	12			29					31
"	F18Y	12/ 2/57- 4/ 1/58	"	x		"	x				"
"	"	1/ 1/59- 4/23/59	"			"					"
"	"	12/27/59- 5/21/60	"			"					"
"	"	2/ 1/61- 1/30/62	"			"			30		"
"	"	3/20/62- 2/26/63	"	x	x	"		x		x	"
"	"	3/21/63- 4/13/64	"	x	x	"		x			"
"	F18S	5/ 7/64- 5/ 8/65	"	x	x	"	x	x			"
"	F18Y	7/15/65- 5/ 7/66	"	x	x	"	x	x			"
"	"	9/ 2/66- 11/30/66	"	x	x	"	x	x			"
"	F18I	12/ 1/66- 5/ 7/67	"	x	x	"	x	x			"
"	F18Y	10/10/67- 6/16/68	"	x	x	"	x	x		x	"
"	"	10/23/68- 6/ 3/69	"	x	x	"	x	x		x	"
"	"	11/17/69- 6/18/70	"	x	x	"	x	x		x	"
"	"	12/ 8/70- 7/19/71	"	x	x	"	x	x		x	"
"	"	1/19/72- 8/28/72	"	x	x	"	x	x		x	"
"	"	3/ 5/73- 12/ 9/73	"	x	x	"	x	x		x	"
"	"	4/ 8/74- 2/14/75	"	x	x	"	x	x		x	"
M20	M20Y	3/30/60- 8/ 6/60	13			32					33
"	M20	3/ 7/61- 11/20/61	"			"					"
F20Y	F20Y	4/25/64- 5/11/65	14	x	x	34	x	x			35
"	"	7/15/65- 5/ 7/66	"	x	x	"	x	x			"
"	"	9/ 1/66- 5/ 7/67	"	x	x	"	x	x			"
"	"	10/10/67- 6/16/68	"	x	x	"	x	x			"



Table II-8 - continued.

DSN (1)	C.C. (2)	Dates (3)	Raw Data			5° Data				2° Data				65DS# (4)
			DS# (4)	Cal (5)	Q (6)	DS# (4)	Flx (7)	Q (6)	65 (8)	Eur (9)	DS# (4)	Flx (7)	Q (6)	
F22Y	F22Y	7/10/65- 5/ 7/66	16	x	x	38	x	x			39	x	x	40
"	"	9/ 2/66- 5/ 7/67	"	x	x	"	x	x			"	x	x	"
"	"	10/10/67- 6/19/68	"	x	x	"	x	x			"	x	x	"
"	"	10/21/68- 7/22/69	"	x	x	"	x	x			"	x	x	"
"	"	11/17/69- 7/22/70	"	x	x	"	x	x			"	x	x	"
"	"	12/ 7/70- 8/ 4/71	"	x	x	"	x	x			"	x	x	"
"	"	1/19/72- 8/28/72	"	x	x	"	x	x			"	x	x	"
"	"	3/ 5/73-12/25/73	"	x	x	"	x	x	x		"	x	x	"
"	"	4/ 8/74- 2/14/75	"	x	x	"	x	x	x		"	x	x	"
F25Y	F25Y	11/19/69- 7/22/70	17	x		41	x	x						
"	"	1/14/71- 8/ 4/71	"	x	x	"	x	x						
"	"	2/ 2/72- 8/28/72	"	x	x	"	x	x						
"	"	3/16/73-12/25/73	"	x	x	"	x	x	x					
F26A	F26A	4/16/73- 2/11/74	18	x	x	42	x	x						
"	"	5/10/74- 3/ 1/75	"	x	x	"	x	x						
M27Y	M27Y	2/19/60- 3/21/60	19			43								44
"	M27	8/17/61-11/19/61	"			"								"
"	M27Y	8/21/62-11/27/62	"	x	x	"		x						"
"	"	4/27/63- 1/25/64	"	x	x	"		x						"
"	"	9/ 1/65- 3/23/66	"	x	x	"		x						"
"	"	9/ 2/66- 4/15/67	"	x	x	"		x						"
"	"	10/ 1/67- 5/11/68	"	x	x	"	x	x	x					"
"	"	11/ 5/68- 6/20/69	"	x	x	"	x	x	x					"
"	"	12/11/69- 7/ 6/70	"	x	x	"	x	x	x					"
"	"	1/20/71- 8/16/71	"	x	x	"	x	x	x					"

Table II-8 - continued.

DSN (1)	C.C. (2)	Dates (3)	Raw Data			5° Data			2° Data		
			DS# (4)	Cal (5)	Q (6)	DS# (4)	Flx (7)	Q (6)	DS# (4)	Flx (7)	Q (6)
M27Y	M27Y	3/30/72- 9/ 1/72	19	x	x	43	x	x			44
"	"	4/27/73-10/28/73	"	x	x	"	x	x			"
"	"	5/ 9/74-11/16/74	"	x	x	"	x	x			"
F27Y	F27Y	1/16/58- 3/31/58	20			45					47
"	"	2/ 4/59- 4/23/59	"			"					"
"	"	12/26/59- 5/21/60	"			"					"
"	"	2/ 1/61- 1/31/62	"			"			46		"
"	"	3/20/62- 3/ 6/63	"	x	x	"	x	x			"
"	"	3/27/63- 4/15/64	"	x	x	"	x	x			"
"	"	4/25/64- 5/ 8/65	"	x	x	"	x	x			"
"	"	7/10/65- 5/ 7/66	"	x	x	"	x	x			"
"	"	9/ 2/66- 5/ 6/67	"	x	x	"	x	x			"
"	"	10/10/67- 6/20/68	"	x	x	"	x	x			"
"	"	10/21/68- 7/23/69	"	x	x	"	x	x			"
"	"	11/17/69- 6/18/70	"	x	x	"	x	x			"
"	"	12/17/70- 8/ 3/71	"	x	x	"	x	x			"
"	"	1/19/72- 8/28/72	"	x	x	"	x	x			"
"	"	5/ 4/73-12/25/73	"	x	x	"	x	x			"

## Notes for Table II-8:

- (1) DSN is the name of the data set on magnetic tape and should be used in the DSN= parameter of the data definition cards. The raw data sets are contained on tape volume JRRD1. All other data sets are on tape volumes JRID1 and JRID2. For 2° data sets (see Table II-6) the data set name is modified by adding a 2 or a 65 to the regular 5° data set name to get the appropriate epoch 57.0 or epoch 65 2° data group. For example, F18Y2 is the data set name for Florida 18-MHz, epoch 57.0, 2° data and to access Maipu, Chile 15-MHz, epoch 65, 2° data the name is M1565.

Table II-8 - continued.

DSN (1)	C.C. (2)	Dates (3)	Raw Data			5° Data			2° Data		
			DS# (4)	Ca1 (5)	Q (6)	DS# (4)	Flx (7)	Q (6)	DS# (4)	Flx (7)	Q (6)

- (2) C.C. stands for the card code which is punched on each card for basic identification. See Table II-1 for further explanation of the code. Apparitions may be subdivided if the card code changes during an apparition.
- (3) Listed are the earliest and latest observation dates within each apparition for all data sets with the given card code.
- (4) DS# refers to the number of the data set on magnetic tape. This number is used in the LABEL= parameter of the data definition cards. Note that the data set number for epoch 57.0 2° data is tabulated under DS# and for epoch 65 data under 65DS#.
- (5) The presence of sufficient calibration data on the raw data cards to permit flux density computations is indicated by an "x".
- (6) An "x" indicates that the quality code (see Tables II-1, II-4, and II-6) is included in the cards for that data set and apparition. In the 26.3-MHz data this quantity is called storm credibility (see Tables II-2 and II-7). Note that the epoch 65 2° data will have quality codes if they are included in the corresponding raw data.
- (7) These columns show the presence or absence of calculated flux density. The calculations have not been checked for accuracy by the author. More information on the flux densities can be found in Miller (1970).
- (8) An "x" in this column means the 5° data have been punched in the format of Table II-5 rather than that of Table II-4.
- (9) Calculation of the positions of Galilean Moon V (Amalthea) replaces the Europa positions for the 5° data marked in this field (see Table II-4).



Table II-9  
Summary of Frequency Statistics  
Florida Data

DSN	# Cards	Total List. (minutes)	Total Act. (minutes)	Prob.
(1)	(2)	(3)	(3)	(4)
M05	460	28815	1326	.046
M10	3063	135994	11490	.084
H10I	100	7363	194	.026
F10P	492	64958	686	.106
F12H	2163	74621	8855	.119
M13P	680	56321	2447	.043
M15	2211	121274	8191	.068
F15Y	5778	369284	20037	.054
M16	2701	223281	8059	.036
M18Y	9503	750464	30780	.041
H18Y	2291	91823	9499	.103
F18Y	15425	878970	56827	.065
M20	462	120425	489	.004
F20Y	7300	658540	23442	.036
M22Y	6162	720419	15159	.021
F22Y	10217	959295	32623	.034
F25Y	1222	130716	2059	.016
F26A	936	59541	9494	.159
M27Y	4049	685555	5166	.008
F27Y	4907	881709	7605	.009
Totals	80122	7019368	254428	.036

Notes for Table II-9:

- (1) DSN is the name of the data set (see Table II-8) which is a generalization of the card codes as explained in Table II-1. The 5° names are used since the rest of the table is based on these data.
- (2) The number of cards in the 5° data sets is listed. The number of cards in the corresponding raw data and 2° data sets will sometimes vary because of lost cards.
- (3) The activity and listening times are computed from the 5°-zone intermediate cards.
- (4) The probability shown is the average occurrence probability or simply the ratio of total activity time to total listening time.

```
//filename DD UNIT=(TAPE9,,DEFER),DISP=OLD,VOL=(,RETAIN,SER=vname),
//          DCB=(RECFM=FB,LRECL=80,BLKSIZE=3200),
//          LABEL=(ds#,,,IN),DSN=dsn
```

The appropriate tape volume name is substituted for vname and ds# and dsn are listed in Table II-8.

Naturally, there is a need for adding new data to the tape as it becomes available. The suggested system for doing this is shown in Figure II-4. JRID2 is the volume and serial number of the main tape kept in the NERDC tape library. JRID1 is the backup tape to be kept by the person in charge of the data. The program STLMY performs the conversion from raw to intermediate data in either 2° or 5° format. The new intermediate data are generated on a temporary disk data set and listed on the printer. The disk is merged with the old tape, JRID2, to yield an updated JRID1 tape volume. After the resulting tape has been carefully verified for accuracy, it is copied onto volume JRID2. Note that JRID1 and JRID2 currently contain ephemeris cards for 1957-1975, which are necessary for processing raw data (see Table II-3). If ephemeris cards later than 1975 are needed, either the ephemeris file on tape will have to be augmented or the ephemeris cards should be read in directly. In the same way, raw data may be put in on cards or merged with tape volume JRRD1 before use.

### 2.3 University of Texas Data

Thanks to the generosity of the decametric radio observers at the University of Texas, the University of Florida received a catalog of the Texas data (Bozyan, et al., 1972) at the same time the Florida data were being organized for tape loading. The Texas observing frequencies were often close to or equal to those of Florida, so that a merger of the

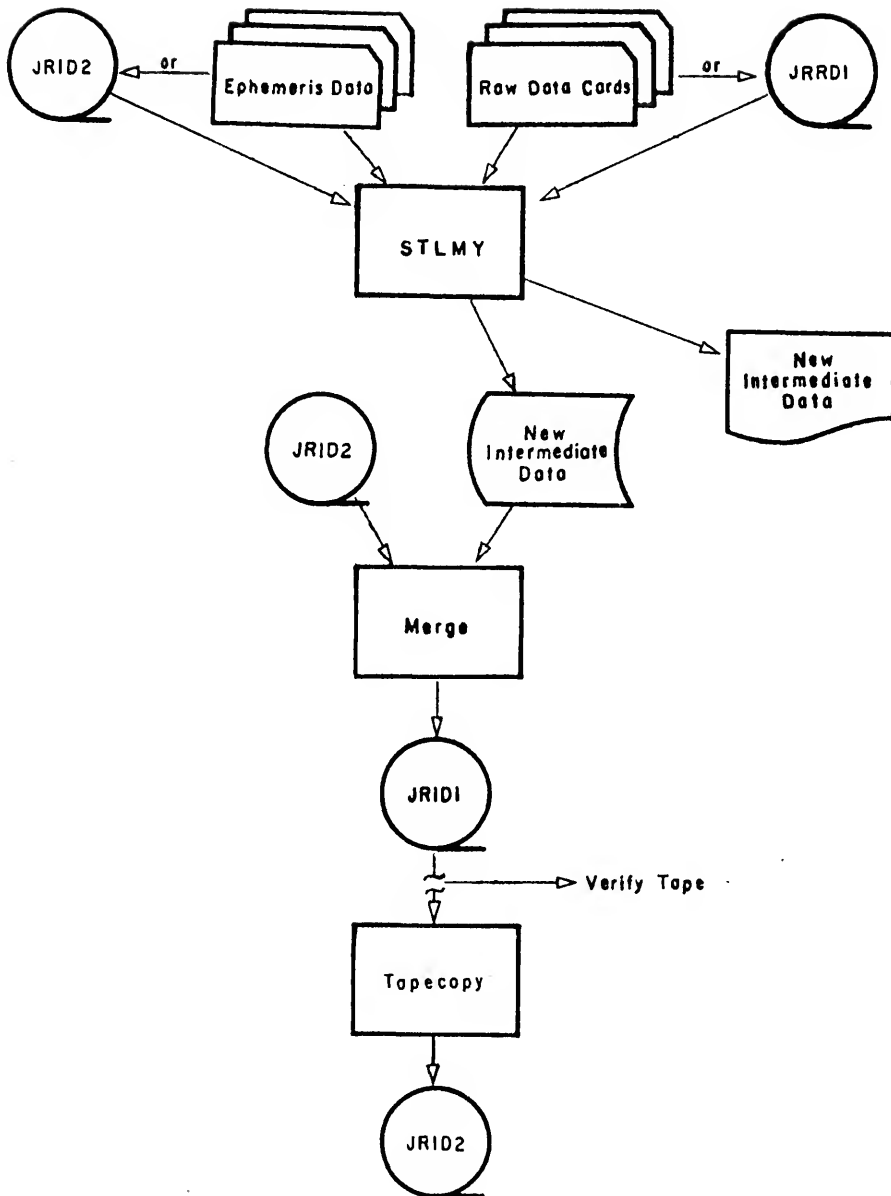


Figure II-4. System flowchart for update of intermediate data tapes.

two data sets was obviously advantageous. Raw data cards punched according to Table II-10 were converted to intermediate cards of the form shown in Table II-11 by a modification of the Florida reduction method. Note that the accuracy of the storm and listening times was deemed sufficient to justify expressing the positions of Jupiter and its satellites in  $1^\circ$  zones.

Besides the Florida data, the magnetic tapes JRID1 and JRID2 also contain the Texas intermediate cards. However, raw Texas data have not been loaded onto the JRRD1 tape. Some overall characteristics of the Texas observations are found in Table II-12. For more details the reader should consult the catalog.

In conclusion, the Texas and Florida intermediate cards are the foundation for this dissertation. The large amount of data is especially important for the higher resolution studies to be presented in the next few chapters.

FORTTRAN Format (10I2,3I1)

Notes for Table II-10:

(1) Storm type:

- 1 - Main storm in observing time
- 2 - Precursor in observing time
- 3 - Post-cursor in observing time
- 4 - Main storm outside observing time
- 5 - Precursor outside observing time
- 6 - Post-cursor outside observing time

(2) Storm strength:

- Blank - Not specified
- 1 - Strong (peak flux greater than 20 times Cygnus A)
- 2 - Moderate (peak flux 10-20 times Cygnus A)
- 3 - Weak (less than 10 times Cygnus A)

(3) Storm credibility:

- 1 - Certain (probability event is Jovian 99%)
- 2 - Probable ( " " " " 90%)
- 3 - Possible ( " " " " 50%)
- 4 - As in 1, but may be solar emission
- 5 - " " 2, " " " " "
- 6 - " " 3, " " " " "

All of the above are explained in greater detail in the catalog by Bozyan et al. (1972).

Table II-11  
Intermediate Data Card  
Texas - 1° zones

	Card code (1)
	Year
	Month
	Day
	Julian Date - 24
	System III Longitude (57.0) - listening beginning zone
	" " " " " ending "
	" " " " activity beginning "
	" " " " " ending "
	Position of Io from s.g.c. - listening beginning zone (2)
	" " " " " ending " "
	" " " " " activity beginning " "
	" " " " " ending " "
	Position of Europa from s.g.c. - listening beginning zone (2)
	" " " " " ending " "
	" " " " " activity beginning " "
	" " " " " ending " "
	Position of Ganymede from s.g.c. - listening beginning zone (2)
	" " " " " ending " "
	" " " " " activity beginning " "
	" " " " " ending " "
	Storm type (3)
	Storm strength (3)
	Storm credibility (3)
	Activity beginning time in Universal Time - hours and minutes
	" ending " " " " " " "
	Length of activity in minutes

FORTRAN Format (A4,3I2,I5,16I3,3I1,2I4,I3)

Notes for Table II-11:

- (1) For explanation of card code, see Table II-1.
- (2) The abbreviation s.g.c. stands for superior geocentric conjunction.
- (3) For explanation of these fields, see Table II-10.



Table II-12  
Summary of Frequency Statistics  
Texas Data

DSN	DS#	# Cards	Total List. (minutes) (4)	Total Act. (minutes) (4)	Prob.
(1)	(2)	(3)			(5)
Y10I	1	169	22638	3795	.168
T10I	2	73	4672	147	.031
Y16I	3	330	41815	7001	.167
T16I	4	724	78167	7542	.096
Y19I	5	117	9592	514	.054
Y20I	6	2509	437106	43727	.100
T20I	7	896	107993	7388	.068
Y22I	8	2755	570155	37945	.067
K22I	9	782	125931	8285	.066
T22I	10	1219	164561	7427	.045
Y23I	11	263	28931	1067	.037
T30I	12	1307	207296	1883	.009
Totals		11144	1798857	126721	.070

Notes for Table II-12:

- (1) DSN is the data set name to be used in the DSN= parameter of the data definition cards for magnetic tape volumes JRID1 and JRID2. It is a generalization of the card code which is explained in Table II-1.
- (2) The data set number in this column is used in the LABEL= parameter of the data definition cards for magnetic tape volumes JRID1 and JRID2.
- (3) Listed are the number of cards in the data set on magnetic tape volumes JRID1 and JRID2.
- (4) The activity and listening times are computed from the intermediate cards on magnetic tape.
- (5) The probability shown is the average occurrence probability or simply the ratio of total activity time to total listening time.

CHAPTER III  
ONE-DIMENSIONAL STUDIES

3.1 Histogram Accuracy

3.1.1 Statistical Significance

The usual method of categorizing Jupiter's discrete radio events has been the histogram, such as that of Figure I-1, in which the data are related to a single variable. In this sense, the radio storms are studied for single-dimensional dependence. Generally, the rotation of Jupiter or the orbit of its satellites is divided into intervals, and the number of events or the occurrence probability (the number of events divided by the total number of observations) is plotted for each zone. The representation is straightforward, but conclusions based on it must consider the statistical significance of the method.

Let us look at the typical occurrence probability histogram. The usual method of computation for Jupiter's decametric probability histograms is to set

$$p(x, \Delta x) = \sum_{i=1}^n a_i(x, \Delta x) / n \quad (\text{III-1})$$

where  $x$  is the System III longitude, Galilean moon phase, declination of the earth, or any other appropriate independent variable. The probability in the interval from  $x$  to  $x+\Delta x$  is symbolized by  $p(x, \Delta x)$ . A value of 1 or 0 for the  $a_i(x, \Delta x)$  represents, respectively, the presence or absence of a radio storm for each of  $n$  observations within the interval. The

main question is; Do the histograms closely approximate the functional curve expected from observing for an infinite amount of time and computing the probability for infinitely small intervals? Restating the question mathematically, if

$$p(x) = \lim_{\substack{n \rightarrow \infty \\ \Delta x \rightarrow 0}} \sum_{i=1}^n a_i(x, \Delta x) / n \quad (\text{III-2})$$

then is  $p(x) \approx p(x, \Delta x)$ ? There are two problems in answering this question. First, in any interval, how much statistical variation can be expected with a number of observations substantially less than infinite? Second, assuming no statistical fluctuation, is Jupiter's behavior sufficiently repetitive that the same curve will be continually retraced?

Consider the first problem. A multitude of factors affect the number of radio storms in any interval. Several critical examples are the sensitivity of the radio telescope, the transparency of the earth's ionosphere, and the separation of Jupiter emissions from non-Jovian interference. There will also be minor influences such as the relative state of repair of the detection equipment and the human error involved in identifying the beginning and ending of storms and in codifying the data. Of course, the exact influence of all of these factors cannot be calculated. The assumption will be made that their contribution is a random fluctuation about the limiting functional curve. Thus, if the number of independent observations is large, the standard deviation can be estimated as the square root of the number of events in any interval:

$$\sigma \approx \sqrt{\sum_{i=1}^n a_i(x, \Delta x)} \quad (\text{III-3})$$

$$\Delta p(x, \Delta x) = \sigma / n \quad (\text{III-4})$$

The second equation gives the corresponding variation in the probability. The credibility of this estimate is directly related to the amount of data.

It is possible that statistical variation may be blamed for what is actually a natural variation in the functional curve with time. To what extent are Jovian emission events predictably repeatable? This requires a knowledge of all independent variables which influence the emission. It is known that at middle and high decametric frequencies occurrence probability versus System III longitude histograms would change drastically for different ranges of the position of Io from superior geocentric conjunction (hereafter called the "phase" of Io and symbolized by  $\phi_{Io}$ ). Combining radiation from all of the positions of Io brings a measure of stability to the source probabilities, but they are still altered in a timespan of years due to the changing declination of the earth as viewed from Jupiter ( $D_E$ ). Therefore, the probability of receiving a radio storm depends on at least three variables,  $\lambda_{III}$ ,  $\phi_{Io}$ , and  $D_E$ . Since only about two cycles of the variable  $D_E$  have been observed, there is incomplete coverage of all of their possible combinations.

Bozyan and Douglas (1975) consider this problem in presenting the results of their decametric studies. They assume the probability to be a function of the three variables such that at any time,  $t$ ,  $p(t) = p(\lambda_{III}, \phi_{Io}, D_E)$ . To get a good estimate of this probability function Bozyan and Douglas state the need for simultaneous observations at many terrestrial longitudes, and the longest possible runs of synoptic monitoring. Obviously, simultaneous observations will improve the calculation of the occurrence probability for a given instant of time.

To assume that continuous monitoring is beneficial assumes also that the probability curve is cyclic. How can one be certain that the occurrence probability is a function of  $\lambda_{III}$ ,  $\phi_{IO}$ , and  $D_E$  only, such that several sets of observations of a given range of functional values will yield the same probability? The chances are that the probability does depend on other variables, but the data so far indicate first-order dependence on only  $\lambda_{III}$ ,  $\phi_{IO}$ , and  $D_E$ . The simplest model is, then, only dependent on these three.

This dissertation is based on a search for high-resolution, second-order effects. The term "second-order" is used loosely to classify those phenomena which are not immediately obvious upon inspection of the data, and which are barely separable from statistical fluctuation "noise." Although these phenomena may be more difficult to detect, the search for them should not be abandoned. More care must be taken in their identification. They may be related to the variables already mentioned, in which case they would recur with the appropriate periods, or they may have entirely different periods or no period at all. Since repetition of effects cannot be anticipated, obtaining the maximum number of independent observations for each instant of time becomes important. Simultaneous observations from several terrestrial longitudes have already been mentioned. This dissertation will also merge proximate frequency data obtained at the same observing site from different radio telescopes. Neither of these methods yields truly independent observations, since changes in the propagating medium at the earth, Jupiter, or anywhere between may affect all simultaneous observations. In general, the second-order effects will be assumed to persist from several months to several apparitions, so that with time the short-term fluctuations will be

eliminated by averaging. In cases where the effects are periodic, long-time-span analyses will be beneficial.

### 3.1.2 Time Vs. Event Histograms

In computing the occurrence probability for a histogram interval according to Equation III-1, accuracy is sometimes lost. Within a particular interval the listening time often exceeds the duration of activity, yet the occurrence probability will still be computed as unity. To avoid this, the time of activity should be divided by the listening time for each histogram zone.

$$p(t, x, \Delta x) = \frac{\sum_{i=1}^n a_i(t, x, \Delta x)}{\sum_{j=1}^m l_j(t, x, \Delta x)} \quad (\text{III-5})$$

Here  $a_i(t, x, \Delta x)$  represents the storm time for the  $i$ th event within the histogram zone  $x$  to  $x + \Delta x$ . The listening time for the  $j$ th observation of the zone is represented by  $l_j(t, x, \Delta x)$ . Since more than one storm can occur during a span of listening, these variables cannot be included in the same summation. For a large number of observations occurrence probability histograms computed from either Equation III-1 or Equation III-5 appear similar, although the individual probabilities computed from the former equation will be proportionally higher. For accurate probabilities and when data are scarce, Equation III-5 is more advantageous. This dissertation will use histograms based on time calculations exclusively.

Time-based histograms present some new difficulties. Usually, the beginning and ending listening times for a particular night are known only approximately. Since only the beginning and ending listening zones are given on the intermediate data card (see Table II-4), for ease of

computation the total computed listening time is expanded to correspond to the time between entering the first zone and exiting the last. This will slightly lower the probabilities in the endpoint intervals, but the error decreases as zone size shrinks, and it affects only two zones for each observation period. For activity, the intermediate data card usually has information only on the storm length and the beginning and ending zones. The storm time is adjusted so that the activity extends equally into the beginning and ending intervals. The error caused by this should average out as other storms are added to the zones, and it decreases with a reduction in interval size. For the Florida data continuous radio storms are usually split into five-minute increments. These divisions are rejoined before they are processed in the manner described above.

For time-based histograms the error estimate described in Equation III-4 no longer applies. It is difficult to figure any error without knowledge of the average time contribution per storm to each zone. Consequently, the number of events in each interval has still been recorded. With this information, the standard deviation of the probability can be computed as:

$$\sigma_t = \sigma \sum_{i=1}^n a_i(t, x, \Delta x) / \sum_{j=1}^n a_j(x, \Delta x) = \sum_{i=1}^n a_i(t, x, \Delta x) / \sqrt{\sum_{j=1}^n a_j(x, \Delta x)} \quad (\text{III-6})$$

$$\Delta p(t, x, \Delta x) = \sigma_t / \sum_{k=1}^m l_k(t, x, \Delta x) \quad (\text{III-7})$$

where  $\sigma$  is the standard deviation from Equation III-3 and the second equation is the error estimate for the probability. The error estimate of Equation III-7 will be lower than that defined in Equation III-4, but the time-based probability will also be lower than its event-based equivalent.

### 3.1.3 Decreasing the Histogram Interval Size

The previous chapter introduced the obvious method for increasing histogram resolution in presenting the smaller 2°-histogram-interval Florida data. The discoveries made by Leacock (1971) proved the value of reprocessing the Florida raw data into 2° zones. These findings will be presented later, but it will suffice to say that a subdivision of the histogram interval is necessary for observation of some second-order effects.

How much subdivision can be tolerated before the data within each zone are too sparse to make the results believable? This is a matter of opinion. One measure of the accuracy is the uniformity of listening time in the histogram intervals. Given a reasonable number of observation periods at random observing times, the amount of listening time in each of the intervals should be approximately equal. The percent standard deviation of the group of interval listening times has been monitored as a test of the uniformity.

## 3.2 Decametric Spectral Analysis

### 3.2.1 System III Longitude

The easiest way to display some important aspects of Jupiter emission throughout the decametric wavelength range is to construct a three-dimensional plot of occurrence probability for all System III longitudes over the appropriate span of frequencies. Figure III-1 is an attempt to simulate a diagram of this nature by combining System III longitude histogram data for the individually-observed frequencies having more than 100,000 minutes of observing time. Ninety probability values, obtained by averaging occurrence probabilities for odd-even pairs of



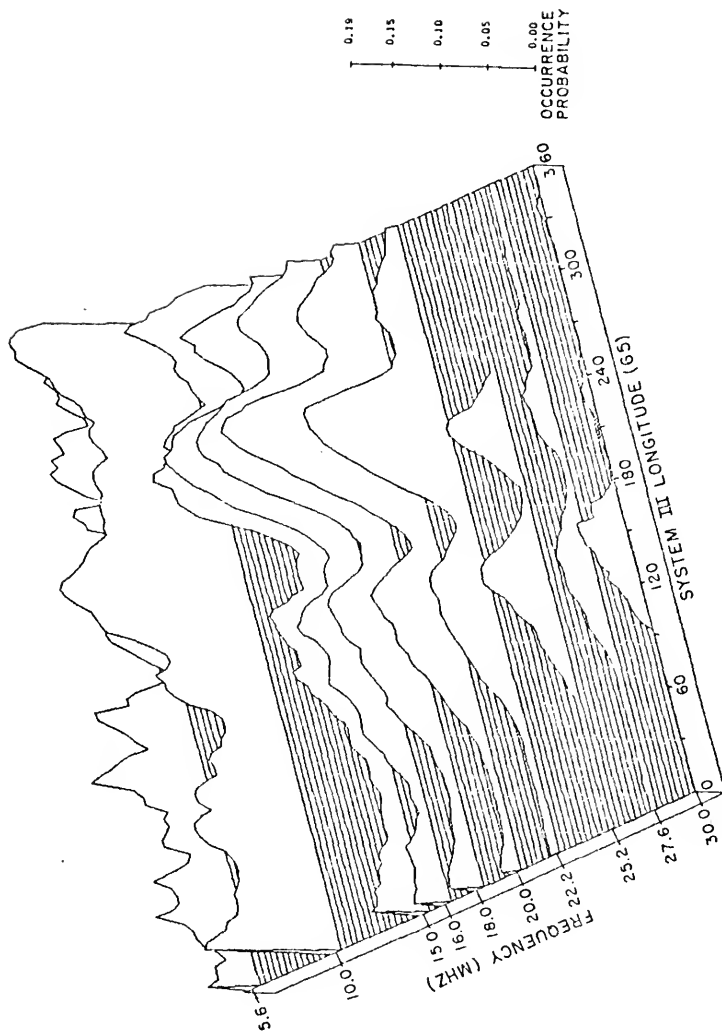


Figure III-1. Perspective view of occurrence probability vs. System III longitude (65) for selected frequencies.

zones in 180-zone histograms, are plotted for each frequency. The 5.0-MHz data are below the listening time cutoff and span only a limited number of years, but they are included as an indication of the lowest frequency results obtainable without satellites. Values of occurrence probability can be determined by comparing the vertical scale at the right of the figure with the height of the curve above the zero plane. It should also be noted that the Florida 16.0-MHz and Texas 16.7-MHz data have been combined and labeled as 16.0.

In this figure it is obvious that sources A, B, and C, as delineated in Figure I-1, are well-defined in the middle decametric frequencies. At first glance it appears that at 15 MHz and above the plots are like the profile of an island which is gradually sinking beneath the sea level of the zero plane. This is consistent with the fact that for similar receiving equipment Jovian activity decreases as frequency increases (Carr et al., 1964). Closer inspection discloses a disproportional decrease in the size of source C above 15 MHz. The same is true for source A above 22 MHz. Some process more complicated than an overall decrease in activity must be involved. The source-B region appears to decrease gradually and then increase at 30 MHz. This upward trend is an artifact resulting from data acquired solely from the Texas-based interferometer used at that frequency. All of the other frequencies involve single Yagi antennas, or a mixture of Yagis and interferometers, providing lower, more comparable sensitivities.

Below 15 MHz the sources no longer maintain their integrity. Two peaks are prominent at the 10-MHz level, and the 5-MHz data are too erratic for determination of any trend. The exact metamorphosis of the plot from 15 MHz to 10 MHz and beyond would be enlightening, but

lack of sufficient data in this void makes interpolation necessary. Figure III-2 suggests how the longitude positions of the source probability peaks change between 10 and 30 MHz. Similar graphs have been made before (Smith, et al., 1965; McCulloch and Ellis, 1966). Data at 5 MHz strongly influenced these earlier investigators, but they have been rejected from Figure III-2 as too sparse to be given credence. McCulloch and Ellis' results were based on relative flux-density plots and imply that sources A and B fade away below 10 MHz while a new source, positioned around  $180^\circ$ , appears near 15 MHz and continues, as does source C at approximately  $350^\circ$ , through 5 MHz and even lower. The occurrence-probability-based plots of Smith et al. suggest that at 5 MHz sources B and C combine into a single source located near  $270^\circ$  and source A moves to about  $120^\circ$ . Two modes of evolution into this lower-frequency configuration were proposed. Both groups of investigators used only two or three years of observations from the early sixties. In Figure III-2, the lines drawn through the source peaks give another interpretation based on (a) updated values for the locations of the maxima, (b) polarization information (Kennedy, 1969), and (c) two-dimensional plots to be presented in the next chapter. The 10-MHz peak located at  $70^\circ$  corresponds to the appearance of source D. This, too, will be more evident in Chapter IV.

What causes the changes in peak locations and the suggested merger of sources A and B at the lower frequencies? This and other theoretical questions will be saved until Chapter V, when the results of Chapters III and IV can be treated together.

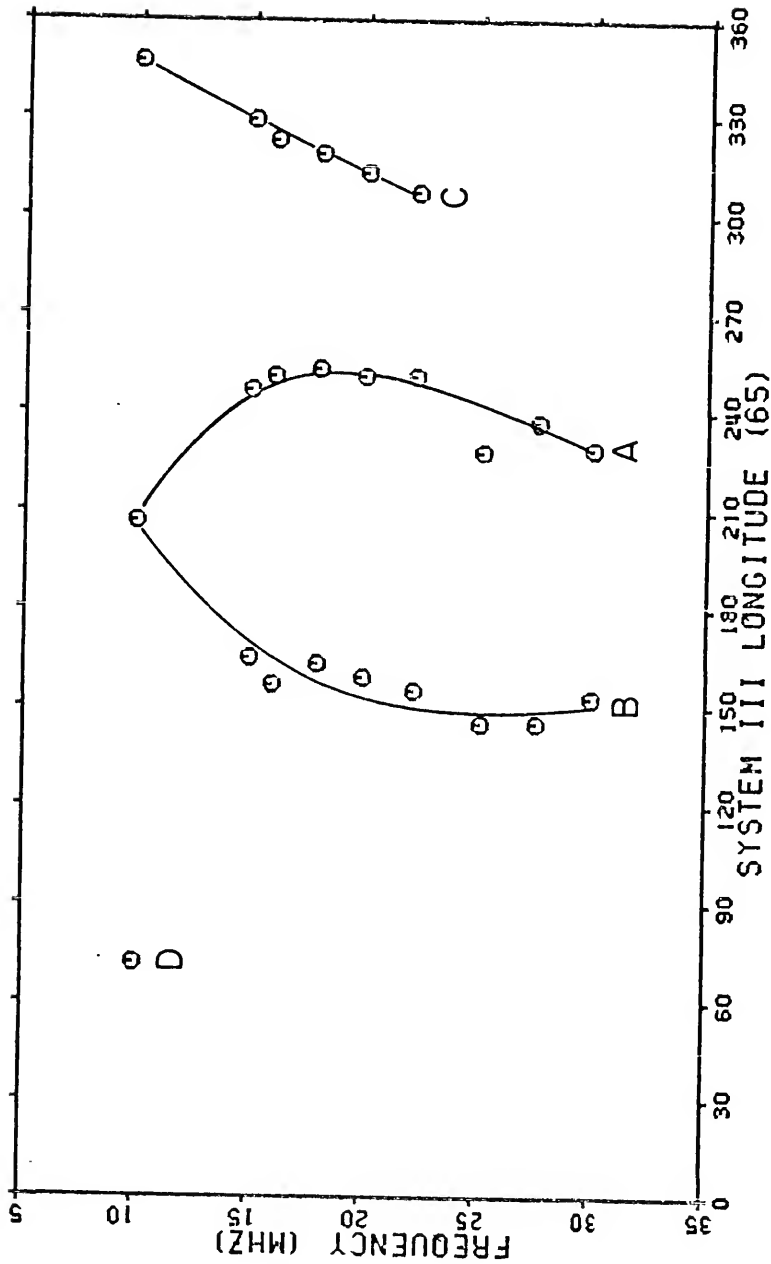


Figure III-2. System III longitude (65) locations of the source probability peaks for selected frequencies. The peaks can be seen in Figure III-1. The 5.6-MHz peaks were excluded on the basis of insufficient data.

### 3.2.2 Phase of Io

Bigg (1964) proved the control of Io on certain aspects of Jupiter's emissions by plotting occurrence probability histograms for the phase of Io. This revealed the now-famous intensification of occurrence probability at  $90^\circ$  and  $240^\circ$  phase values. Additional two-dimensional maps, like that of Figure I-2, disclosed the responsibility of source B for the  $90^\circ$  peak and the combination of sources A and C in the  $240^\circ$  enhancement.

To study the effects of Io on an individual source, one must isolate the storm events or parts thereof occurring in the longitude range defined for that source. The longitudinal limits for the sources have been defined as follows: source B,  $65^\circ$ - $200^\circ$ ; source A,  $201^\circ$ - $290^\circ$ ; and source C, the remainder. The storms associated with each source can then be analyzed in histograms of occurrence probability vs. Io phase. Figures III-3, III-4, and III-5 add information on the variation of Io's influence with frequency. Like Figure III-1, Figures III-3, III-4, and III-5 are pseudo-three-dimensional, smoothed plots derived from histogram data.

Figure III-3 emphasizes the strength of the Io control of source B. The maximum occurrence probability, as seen on the scale to the right, is 0.43 which more than doubles the maximum of Figure III-1. The  $90^\circ$  peaks predominate through all frequencies except 5 MHz, which has no activity in the  $90^\circ$  region. Again, the lack of data (52 per cent standard deviation of the listening times per zone) and limited number of years of observation at this frequency lessens the significance of this finding. The peaks remain very stable in position through all of the frequencies at a value usually quoted as  $90^\circ$ , although the average peak

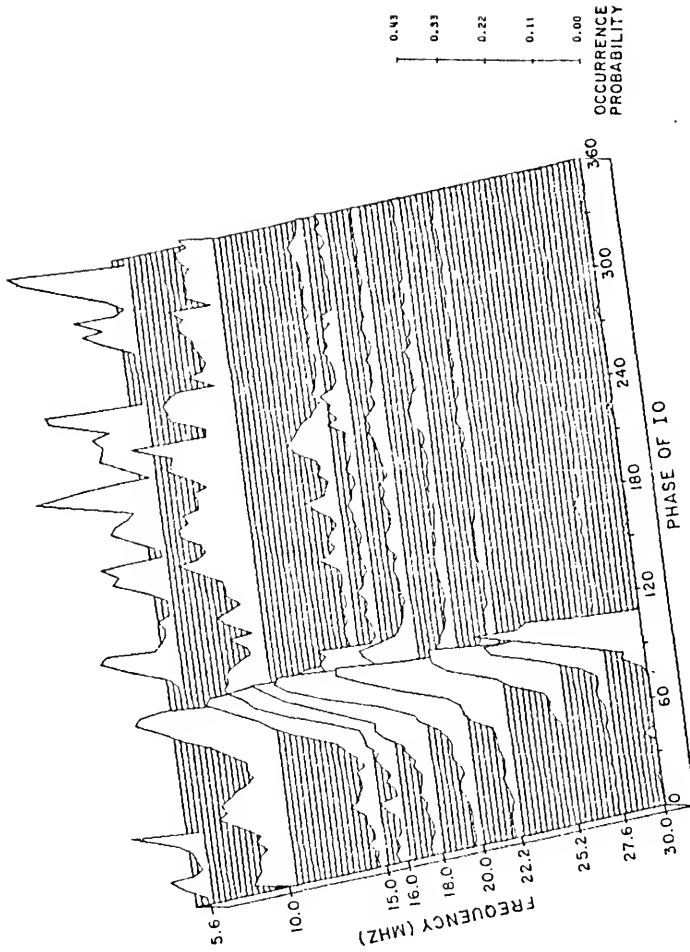


Figure III-3. Perspective view of occurrence probability of source-B storms vs. phase of Io for selected frequencies.

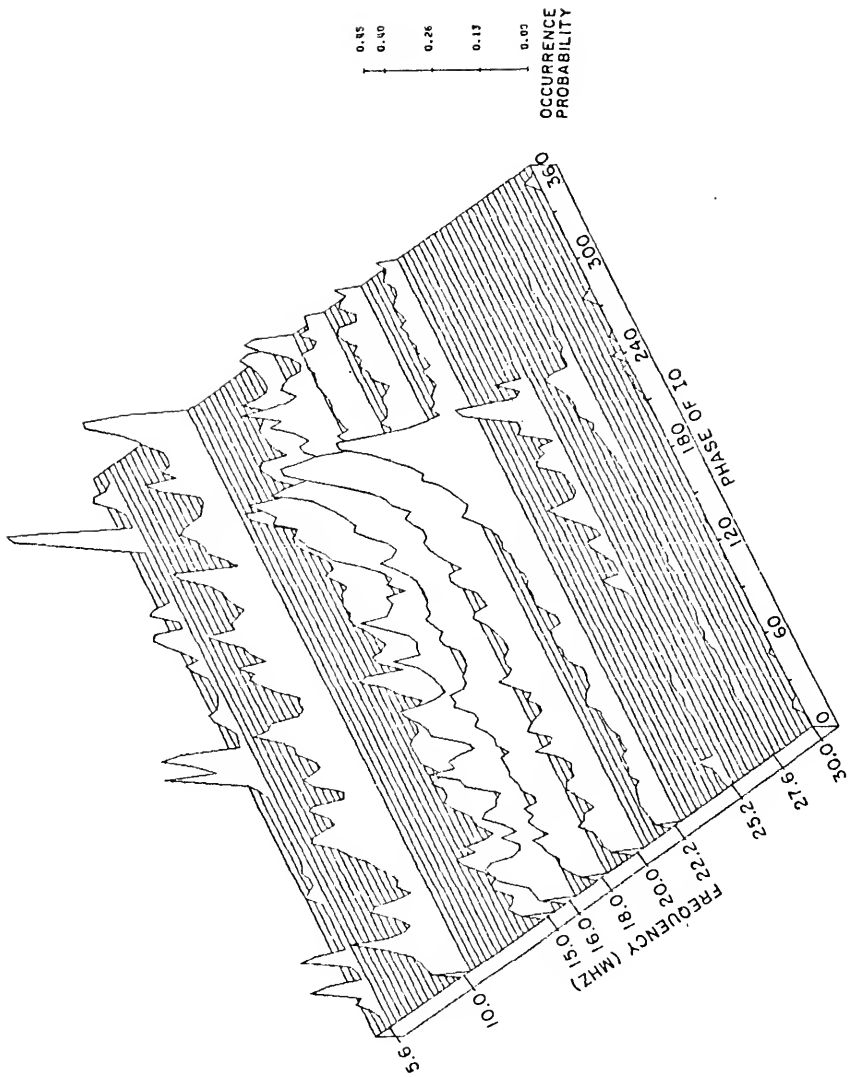


Figure III-4. Perspective view of occurrence probability of source-A storms vs. phase of Io for selected frequencies.

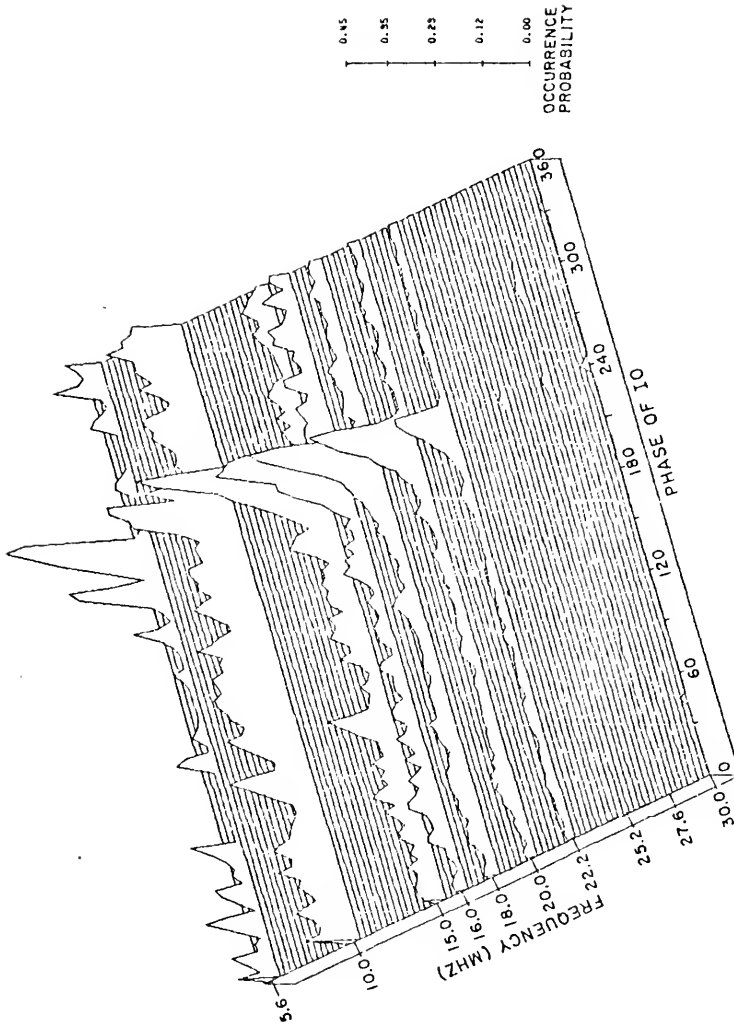


Figure III-5. Perspective view of occurrence probability of source-C storms vs. phase of Io for selected frequencies.



position for the nine frequencies was  $93^\circ$  with a standard deviation of  $2^\circ$ . Notice also the increased non-Io-related radiation as the frequency decreases.

Figure III-4, a diagram of the isolated A region, displays much more prominent non-Io-related radiation, but the Io-related peaks are still obvious. Io-A is more frequency dependent than B. The maximum Io-related probability occurs around 20 MHz, and seems to taper off in both frequency directions until it is no longer evident at 10 and 30 MHz. Between these limits, the peaks have an average position of  $247^\circ$  with a standard deviation of  $6^\circ$ . Presumably, the large mixture of non-Io-related radiation, especially at lower frequencies where the peak position variation is greater, accounts for the increase in standard deviation over source B.

The quick disappearance of the Io influence on source C above 22 MHz is displayed in Figure III-5. Unlike sources A and B, however, Io control still seems to dominate down to 5 MHz and perhaps even lower, although the lack of data at 5 MHz makes that peak suspicious. The average Io phase for these maxima is the same as that of source A,  $247^\circ$ . The smaller standard deviation of  $3^\circ$  follows from the lower "noise" level of events unrelated to Io.

The frequency dependence of the maximum occurrence probabilities in Figure III-1 and Figures III-3 to III-5 may be more precisely examined in Figure III-6. The error in the ordinate values is difficult to determine, since data obtained by equipment with different sensitivities have often been merged. Except for the 30-MHz data, the Florida observations outweigh those from Texas and the sensitivities seem to agree well enough for general statements based on maximum probability tendencies to be made.

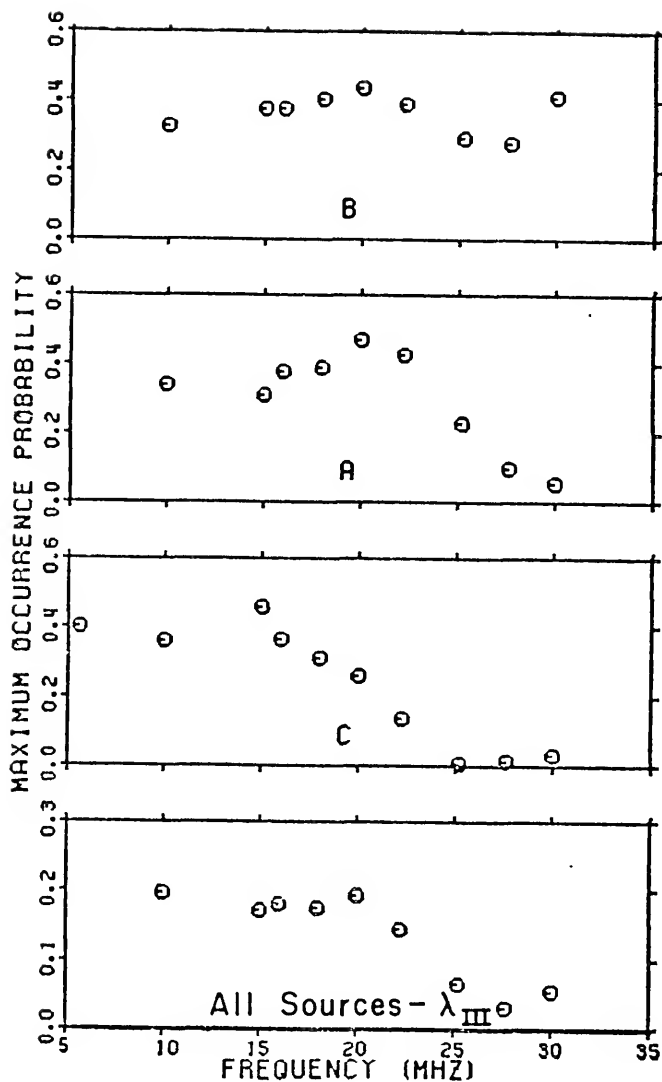


Figure III-6. Spectral distribution of the maximum occurrence probabilities in the Io-phase histograms for isolated source-B, A, and C regions and in the  $\lambda_{III}$  histograms for all sources. (See Figures III-1 and III-3 to III-5.)

As expected, the maximum occurrence probabilities in Figures III-1 and III-4 change in a similar manner with a change in frequency since the major contribution to the peaks in each case comes mainly from the same source-A Io-related radiation. From 10 to 20 MHz both sets of maxima retain nearly constant or slowly increasing levels. Beyond 20 MHz the probabilities decrease at an almost steady rate except for the 30-MHz values which are artificially high. Io-dependent source-B maxima follow the same pattern except for the slower rate of decline at higher frequencies. The isolated source-C region exhibits interesting differences. Its decline begins around 15 MHz, and the source is just barely noticeable above 22 MHz. The labeling of the barely-perceptible storms at these higher frequencies as Io-related is questionable. Note that the 5-MHz peak probability has been included for source C since the peak is similar to and agrees well with those at higher frequencies. From the three peaks at 15 MHz and below the maxima can be construed as approximately constant to, and possibly through, 5 MHz. Dominant Io-related-C radiation at frequencies below 5 MHz would be an interesting discovery. To date no one has published evidence positively linking low-frequency Io-related radiation to a particular source.

### 3.3 Source Chronology

#### 3.3.1 System III Longitude Source Motion

Modification of the sources with frequency has been discussed, but their time evolution must also be considered. The discovery that Jupiter's activity, and especially the source-A characteristics, change over a period of years was made soon after regular Jupiter monitoring began (Gallet, 1961; Douglas and Smith, 1963). The two effects most

quickly recognized were a slow change in the source-A occurrence probability and a gradual translation of its  $\lambda_{III}$  centroid. Gulkis and Carr (1966) first recognized the shifting of the position of source A as a linear drift, resulting from a slight error in the definition of the  $\lambda_{III}$  period, combined with a sinusoidal offset. The pure sinusoidal effect can be observed once the data have been reduced using the corrected period defined by  $\lambda_{III}(65)$  and the centroid of the source is plotted for each apparition.

Calculation of the centroid of a source is very susceptible to error from random statistical fluctuation in the histogram probabilities. For this reason, the results presented in the rest of this chapter will be based upon the largest subset of the data base considered meaningful: the merged observations for 18, 20, and 22 MHz. Even with this pool of more than 90,000 hours of data, the lower-activity years show susceptibility to statistical error. An estimation of the maximum error in the computed centroid value will be made by the following method. Once the centroid has been computed from a particular range of histogram occurrence probabilities, the probabilities to the left of the centroid zone will be decreased by an amount determined by Equation III-7. The probabilities to the right of the centroid are increased in the same manner and a new centroid is computed. The new value is used as an upper error limit for the original centroid. The reverse process yields a lower limit.

With this method an updated study has been made of the source-A sinusoidal motion. The gradual change in the source is apparent from Figure III-7, which compares the  $\lambda_{III}$  histograms from each of the

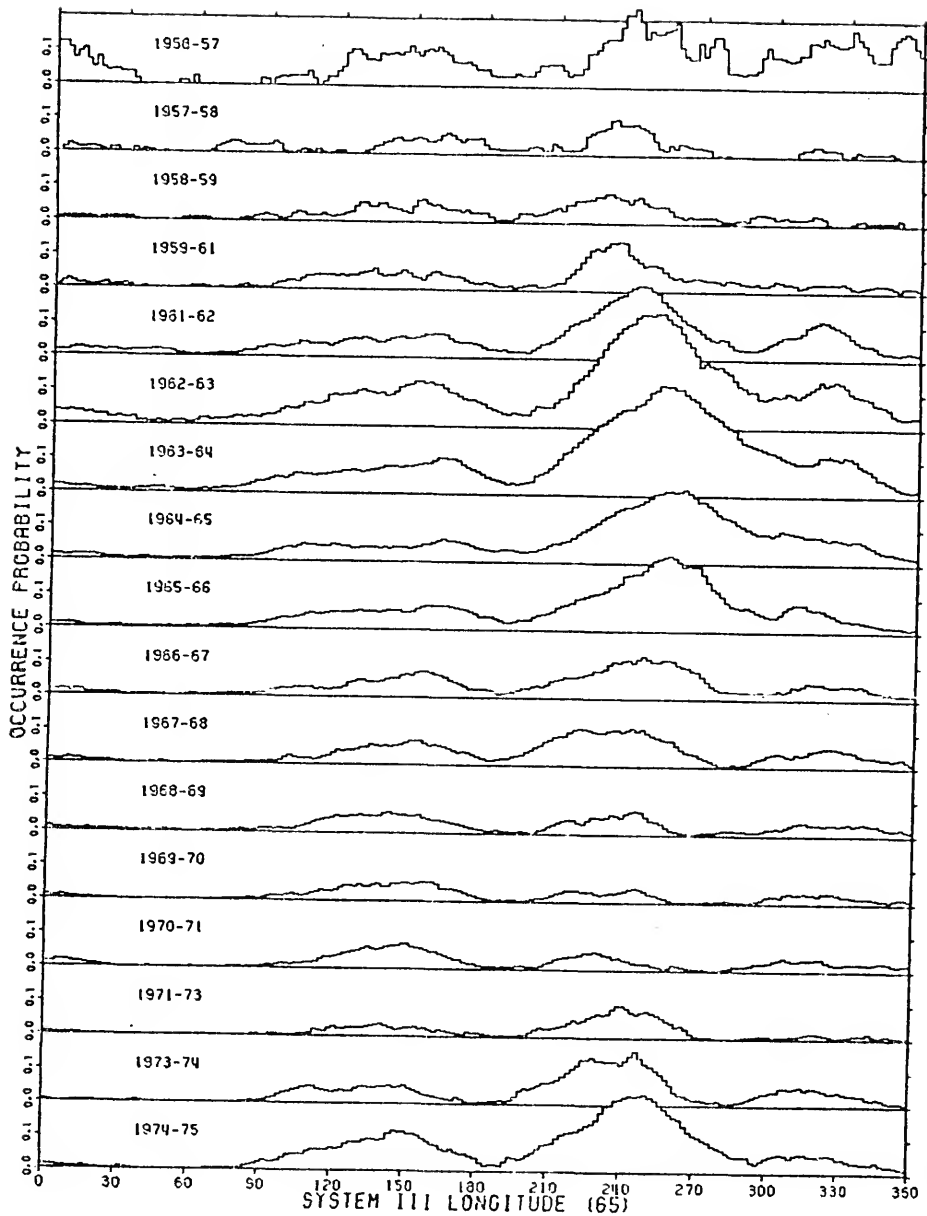


Figure III-7. Individual-aparition occurrence probability histograms for 2° increments in System III longitude (65) based on merged 18, 20, and 22-MHz data.

apparitions. Register and Smith (1969) and Goertz (1971) found that the variation was more prominent in the Io-dependent part of the source-A radiation, and Figure III-8 confirms that this continues through the 1974-75 apparition. The source-A centroid positions and accompanying errors have been plotted for each apparition for the Io-dependent radiation region, the non-Io-related region, and the combination of the two. All source-A radiation occurring when the phase of Io was between  $180^\circ$  and  $270^\circ$  was defined to be Io-related. The centroids were computed from data within particular boundaries defined for each of the Io-dependent, Io-independent, and overall regions. The boundaries were determined from histograms for each region combining all apparitions. The minima on each side of the source-A peak were used as the limits, yielding values of  $188^\circ$ - $288^\circ$  for the Io-related region,  $204^\circ$ - $296^\circ$  for the non-Io part, and  $192^\circ$ - $292^\circ$  for the overall mixture. It may seem wiser to define separate limits for each apparition's  $\lambda_{III}$  histogram, since the minima positions vary greatly from year to year. This procedure is difficult, especially in low activity periods, since the exact position of the minimum dividing source A from a neighboring source is often hard to determine. Nevertheless, an attempt was made to carry out this process. The results were not significantly different from those of Figure III-8.

The dominance of the Io-independent radiation in Figure III-8 in the overall source-A motion is obvious. Some periodic displacement appears in the Io-related sector, but it must be remembered that this region still contains some non-Io-related radiation. Note that the inactive years in this segment, years when Io-dependent radiation dominates, have nearly constant centroid positions. Register and Smith

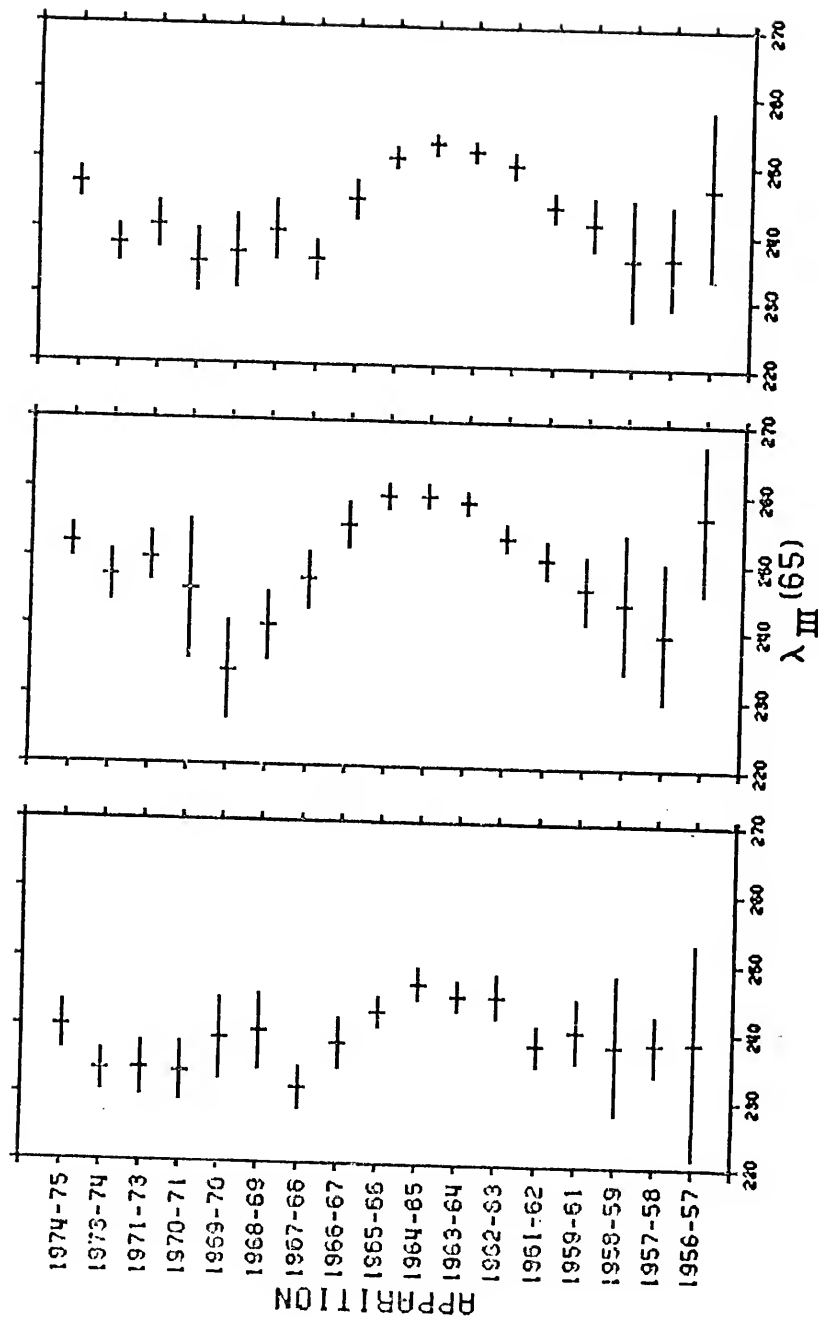


Figure III-8. Comparison of the source-A centroid positions for each apparition for (from left to right) Io-related radiation, Io-independent radiation, and the combination of both, using merged 18, 20, and 22-MHz data.

concluded that the Io-dependent radiation retained a constant rotational period while a variable-amplitude, variable-period, non-Io-related radiation was superimposed on it. Although the rotational period of the Io-independent source A may indeed be variable, the oscillation of the centroid can be explained by causes other than a complete shift of the source in  $\lambda_{III}$  coordinates. This will be discussed again in Chapter V.

As mentioned in Chapter I, Carr explained the sinusoidal source motion as a beaming effect related to the 11.86-year cycle of the declination of the earth ( $D_E$ ) as viewed from Jupiter, resulting mainly from the  $3^\circ$  difference between the Jovian orbital and rotational axes. Donovan and Carr (1969) graphically displayed the correlation of centroid position with  $D_E$  in the manner of Figure III-9. This figure continues the method of Donovan and Carr up to 1975, using the data of Figure III-8. The centroid for each apparition is plotted according to the mean  $D_E$  value obtained by averaging declination values for three months before and after opposition. Weighted, least-squares lines fitted to the data measure the amount of correlation. The equations for the non-Io-A, Io-A, and the overall-A lines, respectively, are as follows:

$$\lambda_{III}(65) = 238.9^\circ \pm .8^\circ + (1.8 \pm .2)\bar{D}_E$$

$$\lambda_{III}(65) = 251.0^\circ \pm .8^\circ + (2.7 \pm .2)\bar{D}_E$$

$$\lambda_{III}(65) = 244.1^\circ \pm .5^\circ + (2.7 \pm .1)\bar{D}_E$$

where the errors are standard deviations. All three lines fit the data quite well, but the larger non-Io-A slope and the matching overall-A slope indicate the dominance of the non-Io radiation in the periodic shift.

Donovan and Carr also looked for a drift in the source-B 18-MHz radiation, finding a possible displacement in the same phase as that of



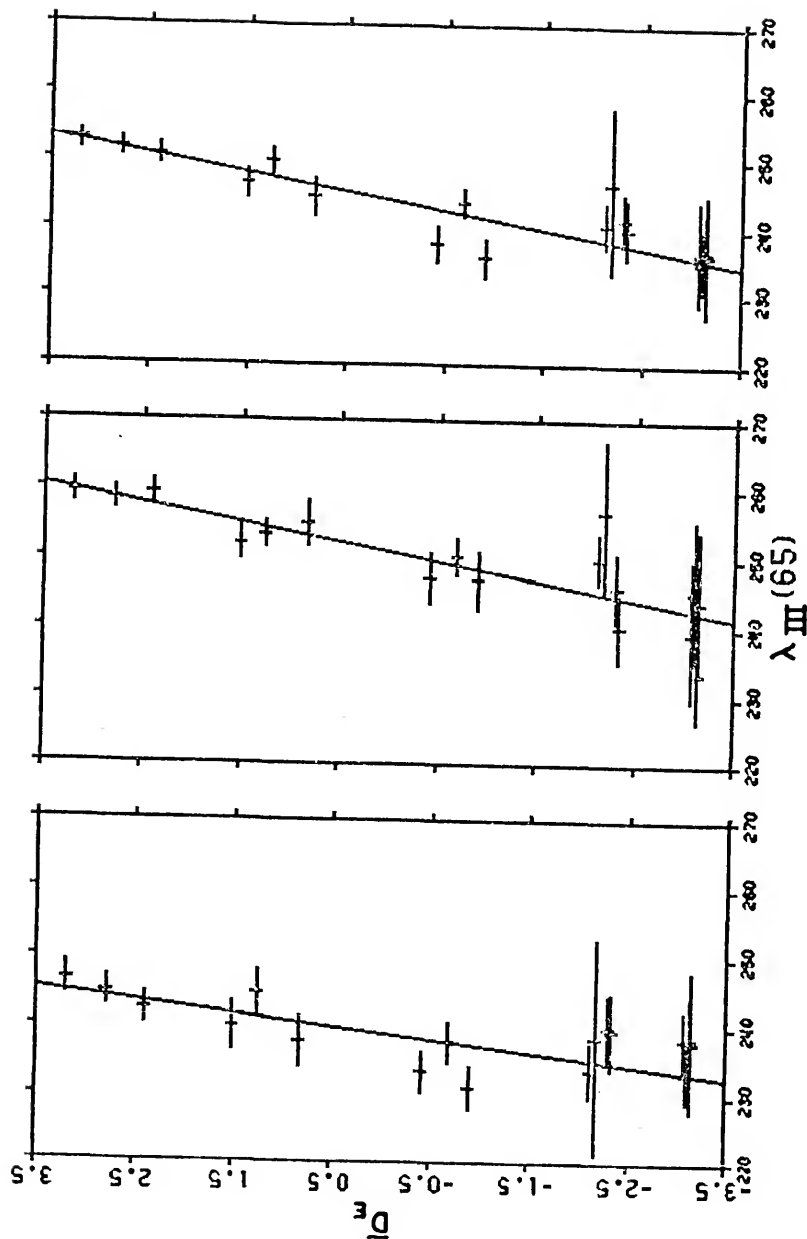


Figure III-9. Correlation of the source-A centroid positions of (from left to right) Io-related radiation, Io-independent radiation, and the combination of both, with the averaged declination of the earth ( $D_E$ ) for each apparition. Weighted least-squares lines have been fitted to the values. The data are taken from Figure III-8.

source A. With the larger data base in the present study no significant motion was found for either source B or source C (see Figure III-10). The boundaries for source B were defined to be  $62^\circ < \lambda_{III} < 188^\circ$ , and  $300^\circ < \lambda_{III} < 30^\circ$  for source C. Perhaps, as in source A, the variation occurs in the non-Io-related segment. Unfortunately, Io-independent-B storms are scarce even in the larger data base. Non-Io-C storms, though more numerous, are difficult to separate from their non-Io-A counterparts, and the position of this boundary is critical in the calculations. The apparition centroids of these regions were computed, however, and some minor trends could be suggested, but overall the results were too erratic and error-prone to be conclusive.

### 3.3.2 Io Phase Drifts

In the process of generating System III longitude histograms for each apparition, Io-phase histograms of the individual source regions were also generated, as shown in Figures III-11, III-12, and III-13. The method of isolating the sources was the same as used in Figures III-3, III-4, and III-5. It should be mentioned that the earliest apparition shows artificially large probabilities and a rugged appearance as a result of insufficient observation time, since, by chance, the small number of observing periods in each zone may each have contributed a storm. Close examination of the figures reveals that the prominent, Io-dependent peaks are unstable in position. This could result from random fluctuations in data acquisition and combination, but a plot of the centroids of these peaks suggest differently. Figure III-14 compares the changing centroid values with the now-familiar  $\lambda_{III}$  shift of source A. The Io-phase motions of sources B and C seem to be correlated with each other and

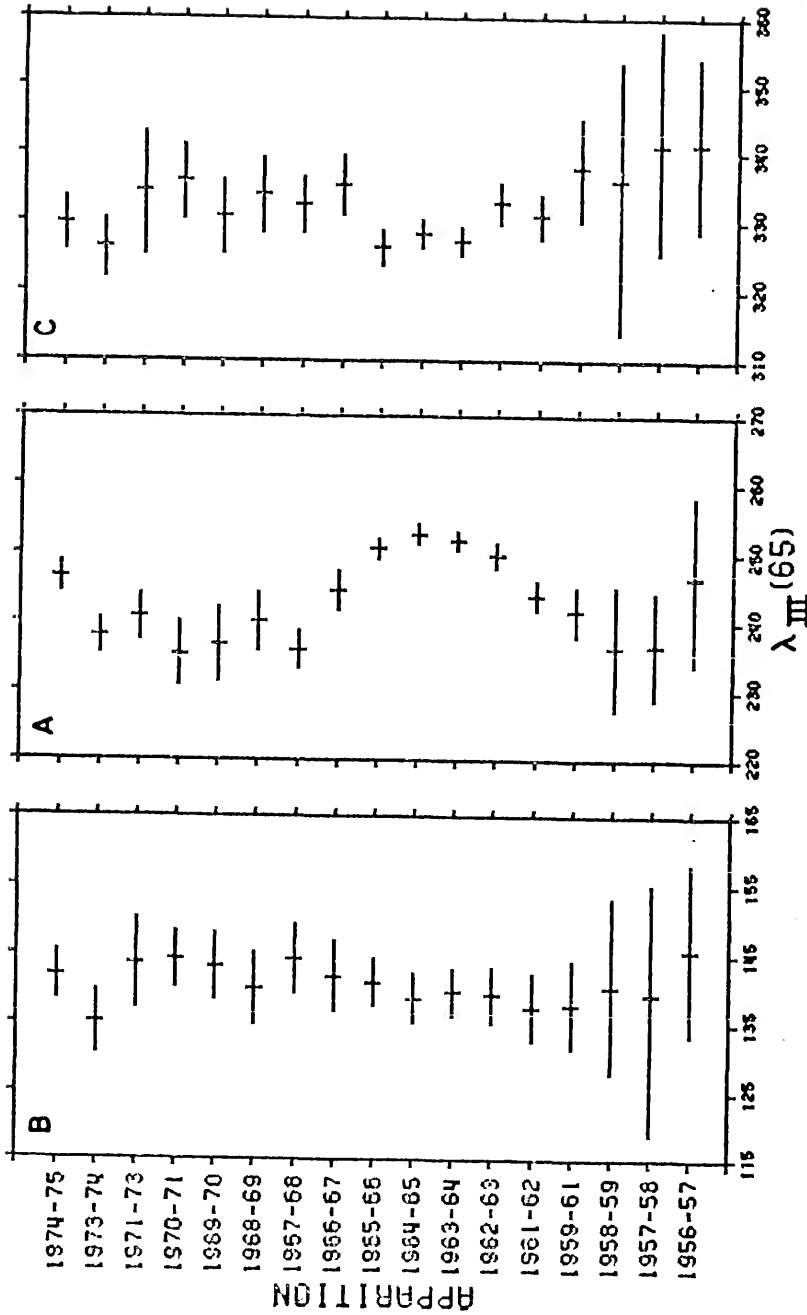


Figure III-10. Apparition-by-apparition comparison of System III longitude (65) centroid positions of sources B, A, and C, for merged 18, 20, and 22-MHz data.

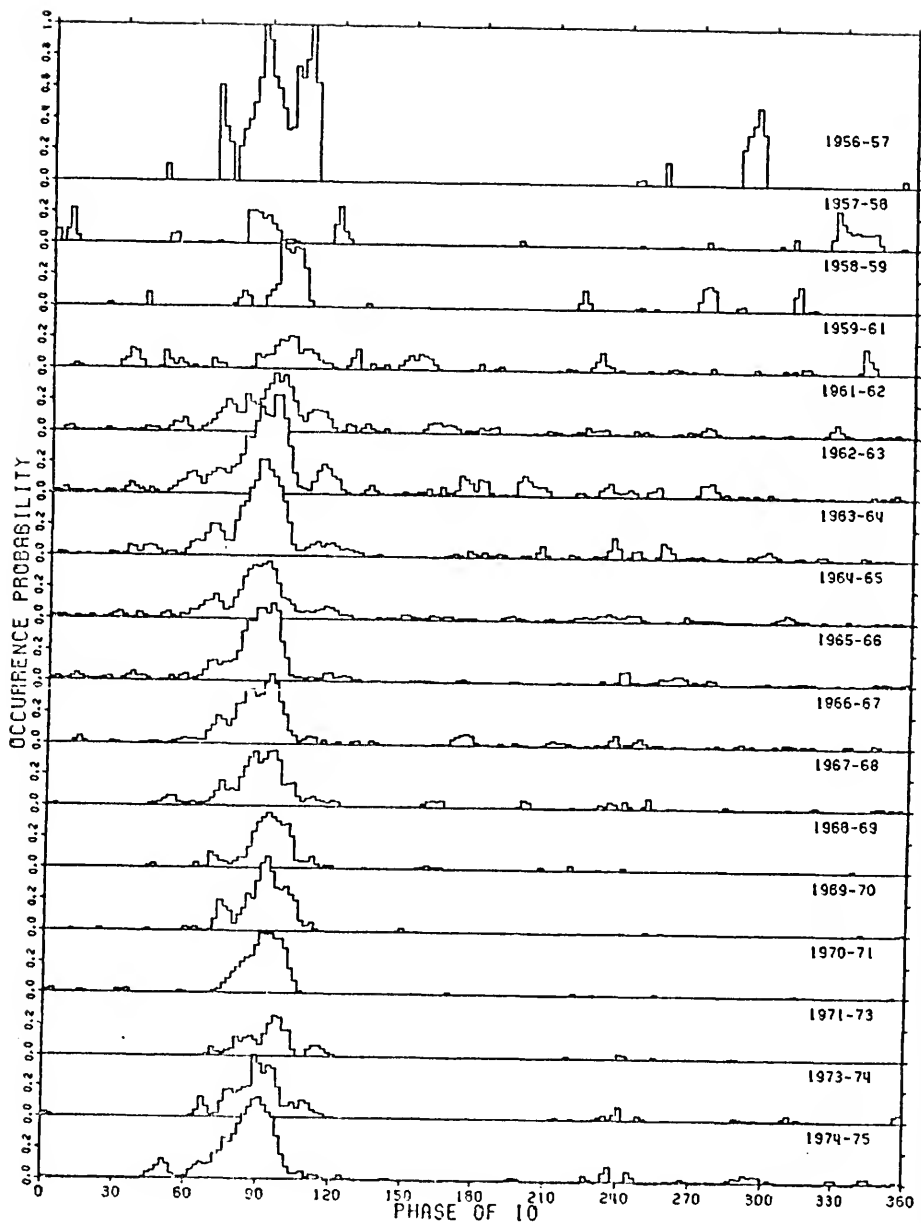


Figure III-11. Individual-aparition histograms of occurrence probability for  $2^\circ$  increments in the phase of Io. All 18, 20, and 22-MHz storms occurring in the source-B System III longitude (65) region are plotted.

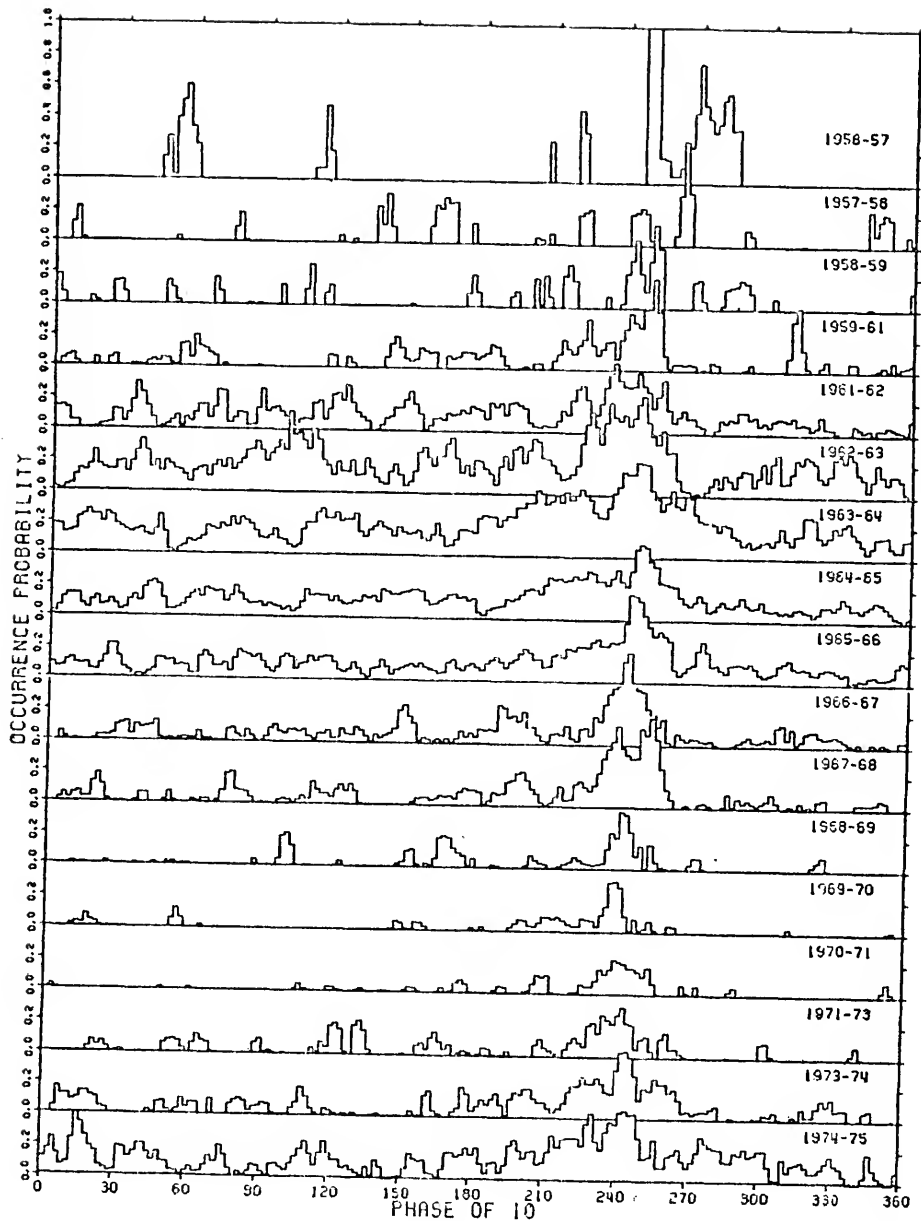


Figure III-12. Individual-aparition histograms of occurrence probability for  $2^\circ$  increments in the phase of  $I_0$ . All 18, 20, and 22-MHz storms occurring in the source-A System III longitude (65) region are plotted.

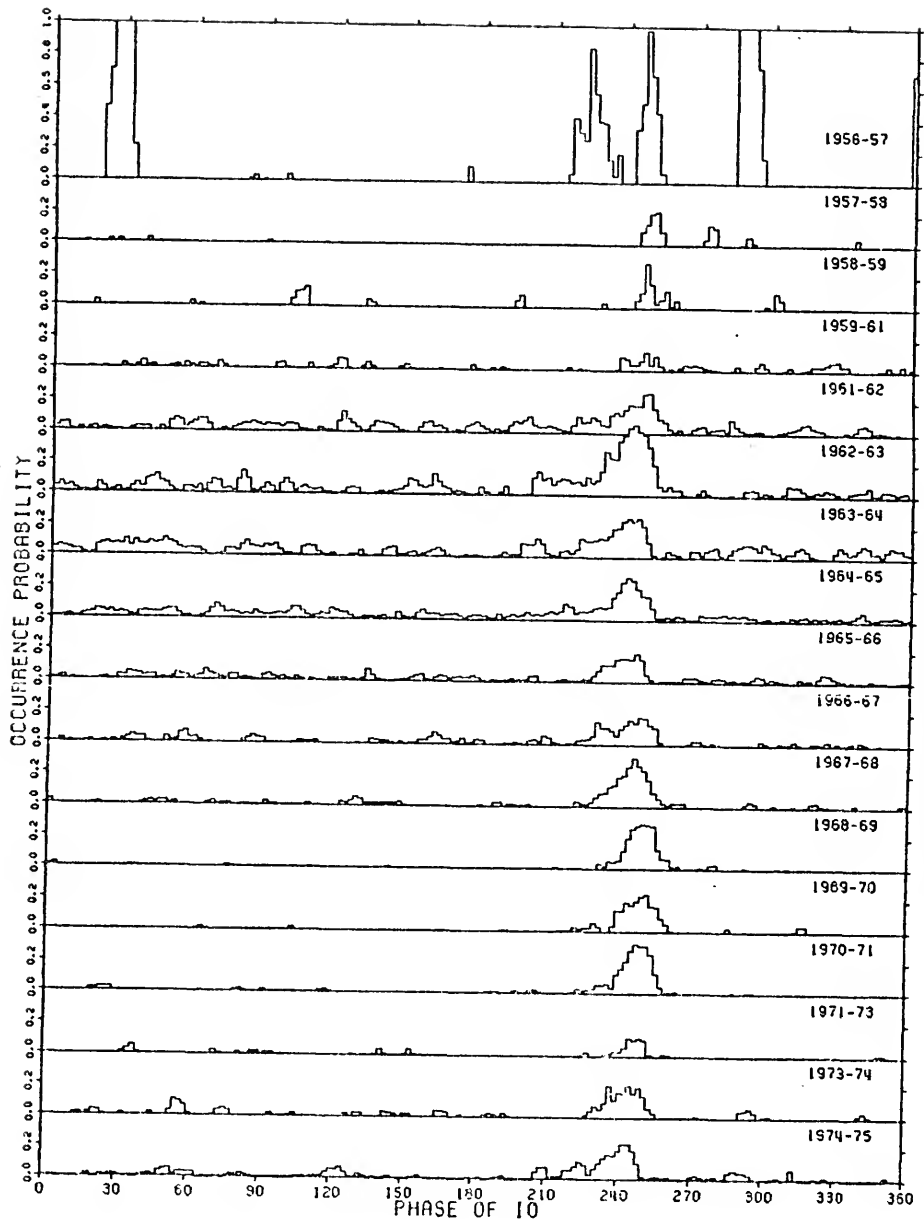


Figure III-13. Individual-aparition histograms of occurrence probability for 2° increments in the phase of Io. All 18, 20, and 22-MHz storms occurring in the source-C System III longitude (65) region are plotted.

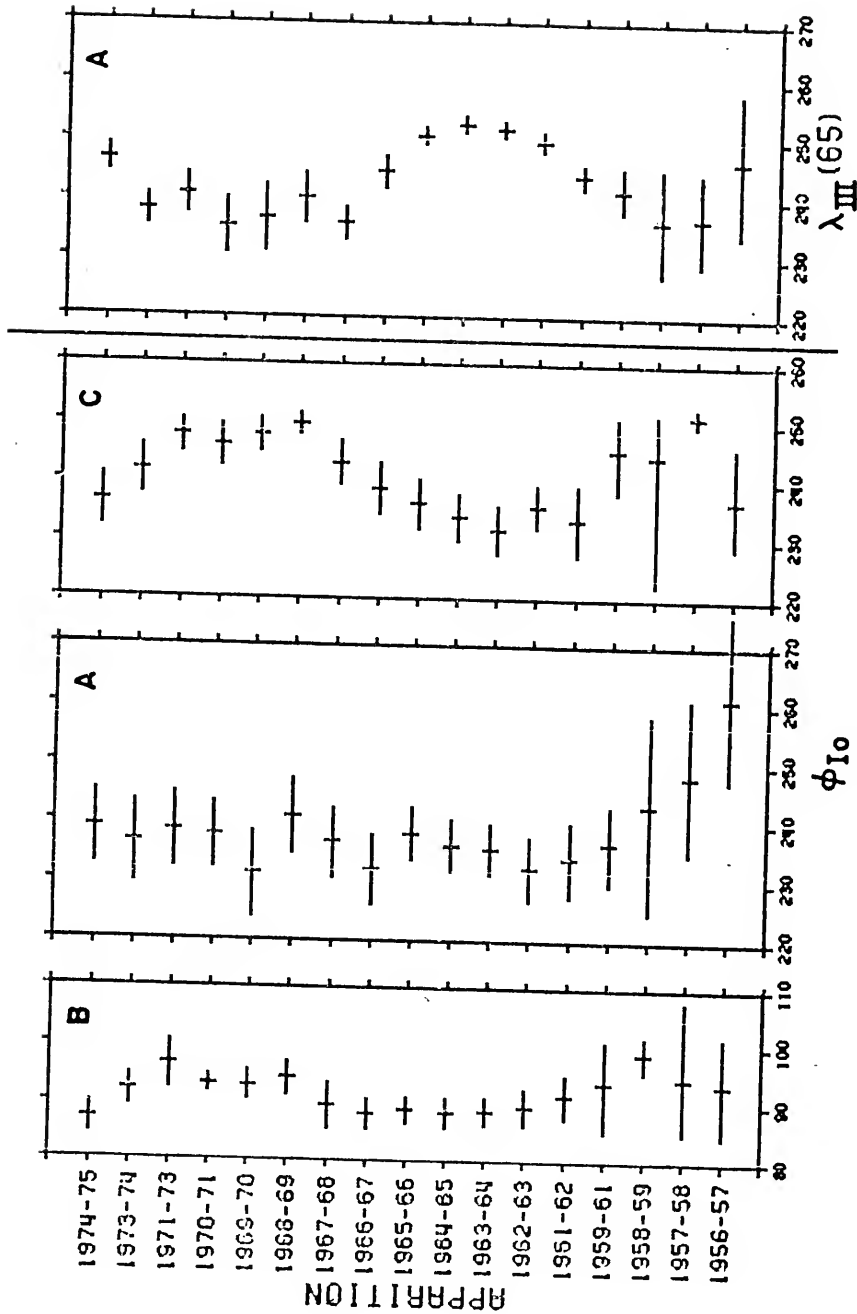


Figure III-14. Apparition-by-apparition comparison of Io-phase centroid positions for sources B, A, and C using merged 18, 20, and 22-MHz data. The System III longitude (65) drift of source A is shown at the right for comparison.

anticorrelated with the  $\lambda_{III}$  shift of source A, that is, an increase in the  $\lambda_{III}$  position of A corresponds with a decrease in the  $I_0$  phase of B and C and vice versa.  $I_0$ -related A exhibits a possible  $I_0$ -phase drift in the early apparitions, where larger errors are apparent, but later years show no significant trends. The strange appearance of the source-C 1957-58 and 1958-59 centroids results from the effects of very small amounts of data on the method of computing errors.

It is interesting that sources B and C appear to oscillate in  $I_0$ -phase coordinates but show no consistent motion in System III longitude, whereas source A behaves in the opposite manner. One obvious difference between sources B and C and source A is the ratio of non- $I_0$ -related to  $I_0$ -related radiation involved in the centroid calculations. Since the data used to compute the  $I_0$ -phase B and C centroids were confined to the regions  $65^\circ < \lambda_{III} < 200^\circ$ ,  $48^\circ < \phi_{I_0} < 126^\circ$  for source B, and  $291^\circ < \lambda_{III} < 64^\circ$ ,  $186^\circ < \phi_{I_0} < 264^\circ$  for source C, the  $I_0$ -related storms should greatly outweigh any satellite-independent radiation. The  $I_0$ -dependent source-A region ( $201^\circ < \lambda_{III} < 290^\circ$ ,  $184^\circ < \phi_{I_0} < 286^\circ$ ), which contains a larger fraction of  $I_0$ -independent storms, has no oscillatory motion, although the larger variability of the activity in this region makes centroid computation difficult. When the  $\lambda_{III}$  centroids were calculated without limits on the phase of  $I_0$ , source A showed the only significant motion and had by far the largest ratio of  $I_0$ -independent to  $I_0$ -dependent radiation. Further discussion of the motions will be delayed until after they have been studied in two dimensions.

The correlation of the  $I_0$ -phase drifts with the averaged declination of the earth is seen in Figure III-15. The weighted, least-squares analysis yielded the following equations for sources B, A, and C



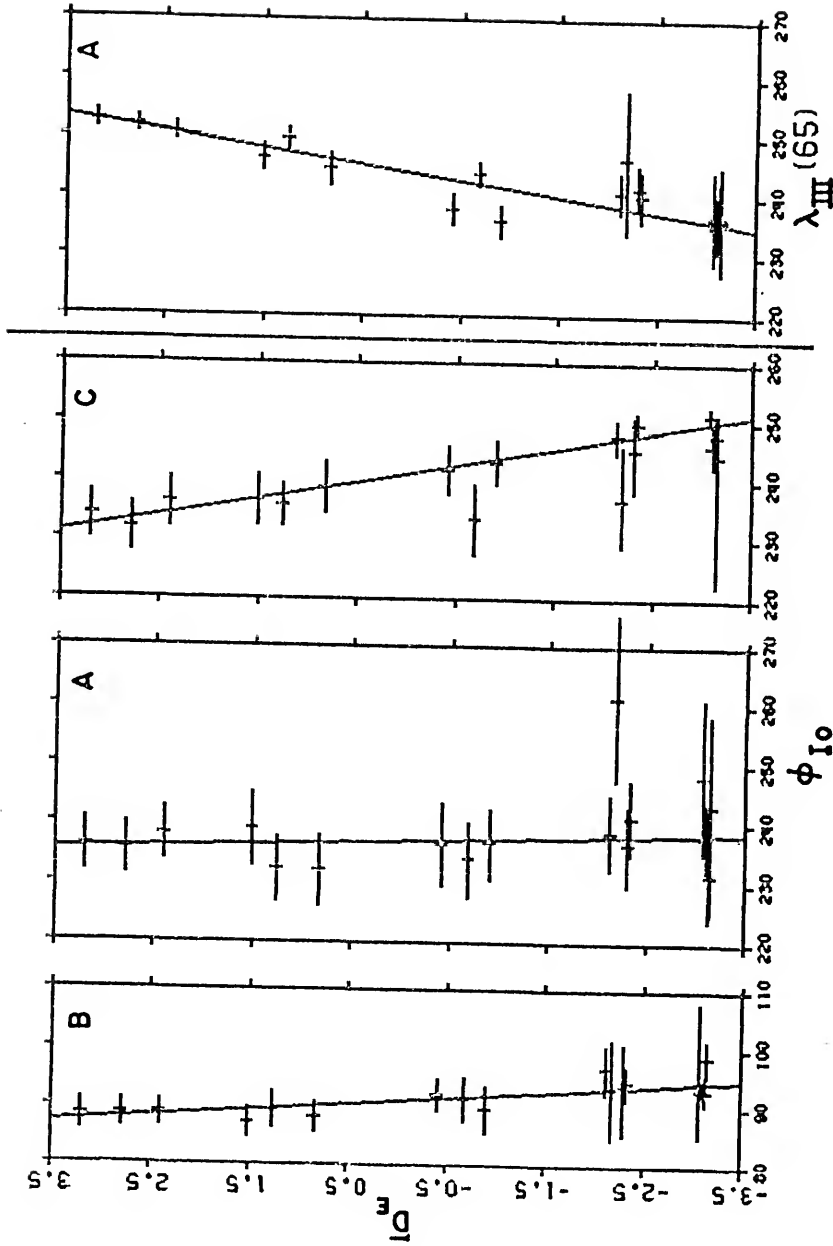


Figure III-15. Correlation of the  $\phi_{10}$  centroid positions of sources B, A, and C and the  $\lambda_{III}$  centroid positions of source A with the averaged declination of the earth ( $D_e$ ) for each apparition. Weighted least-squares lines have been fitted to the values. The data are taken from Figure III-14.

respectively:

$$\phi_{I0} = 91.1^\circ \pm 0.5^\circ + (-1.1 \pm 0.1)\bar{D}_E$$

$$\phi_{I0} = 236.9^\circ \pm 2.4^\circ + (-0.4 \pm 0.5)\bar{D}_E$$

$$\phi_{I0} = 241.1^\circ \pm 1.0^\circ + (-2.9 \pm 0.2)\bar{D}_E$$

The slope of the middle equation, which is within a standard deviation of being zero, corroborates the lack of motion of source A. The other two sources show good correlation with  $\bar{D}_E$ , although the smaller drift in source B results in a slope of less than half the value of that of source C. It is interesting that the fitted values and standard deviations for source C are in the same range as those previously computed for the  $\lambda_{III}$  movement of source A.

### 3.3.3 Asymmetries and Secondary Peaks

The individual-aparition histograms were also useful for a year-by-year study of Leacock's discovery (1971) of a bifurcation of the source-B peak in the Io-phase histograms. It is easier to see these secondary peaks in Figure III-16, which is the smoothed, pseudo-three-dimensional counterpart of Figure III-11. All source-B peaks except those in 1957-58 and 1970-71, which are low-data years, are preceded in Io phase by one or more secondary peaks. Quantitative examination of the minor maxima is difficult because of their low storm levels, but general trends can be distinguished. The second-order peaks seem to be statistically significant since they are often more than  $2\sigma$  above their surrounding minima as measured by Equation III-6. Close inspection reveals that they do not retain a fixed Io-phase position, but move in approximate synchronization with the major peak motion. In the active

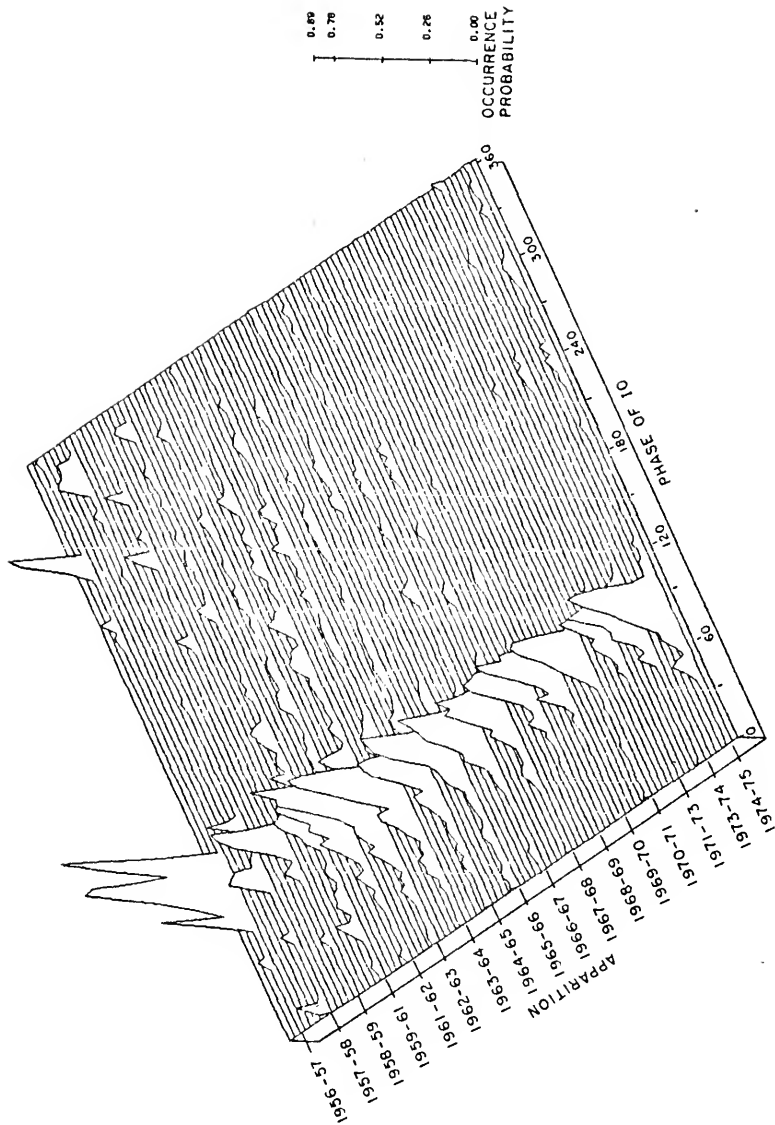


Figure III-16. Perspective view of occurrence probability vs. phase of Io for each apparition of merged 18, 20, and 22-MHz source-B storms. This is based on the data in Figure III-11.

years the separation of the most prominent secondary peak from the main peak remains in the range of  $20^{\circ}$ - $25^{\circ}$ . Secondary peaks following the highest peak can sometimes be seen in Figure III-16 and more readily in Figure III-11, near an  $I_o$  phase of  $115^{\circ}$ . This is a contribution of the 18-MHz data in the mixture, and it is characteristic of the frequencies below 20 MHz, as is shown in Figure III-17, a different view of Figure III-3. The following peak is apparent at 18, 16, and 15 MHz, but it diminishes at 10 MHz. Above 18 MHz, only preceding secondary maxima seem to be permitted. Even where these are missing, a more persistent characteristic is noticeable. The main peak is nearly always skewed toward smaller values of  $I_o$  phase, that is, the occurrence probabilities increase slowly with  $I_o$  phase, reach a maximum and then decrease more rapidly. This is difficult to see in Figure III-17, but Figures III-11 and III-16 provide unobstructed viewing angles.

The slow onset and rapid cutoff of  $I_o$ -related occurrence probability is manifest in more than just the B region. Figures III-18 and III-19 taken from Figures III-12 and III-13, reveal similar asymmetries for the A and C regions. The non- $I_o$ -related radiation makes the source-A picture somewhat confusing, but the asymmetry is still evident. Also reminiscent of source B are the secondary peaks which often occur in the rising incidence of storms preceding the A and C peaks in  $I_o$  phase. Source A may have several of these, while there is normally only a single bifurcation of source C. They have no preferred position, although the enhancement in the C region occurs fairly often in the  $200^{\circ}$ - $210^{\circ}$  range. Secondary peaks and asymmetries can be observed at other frequencies above 10 MHz in the plots of Figures III-4 and III-5.

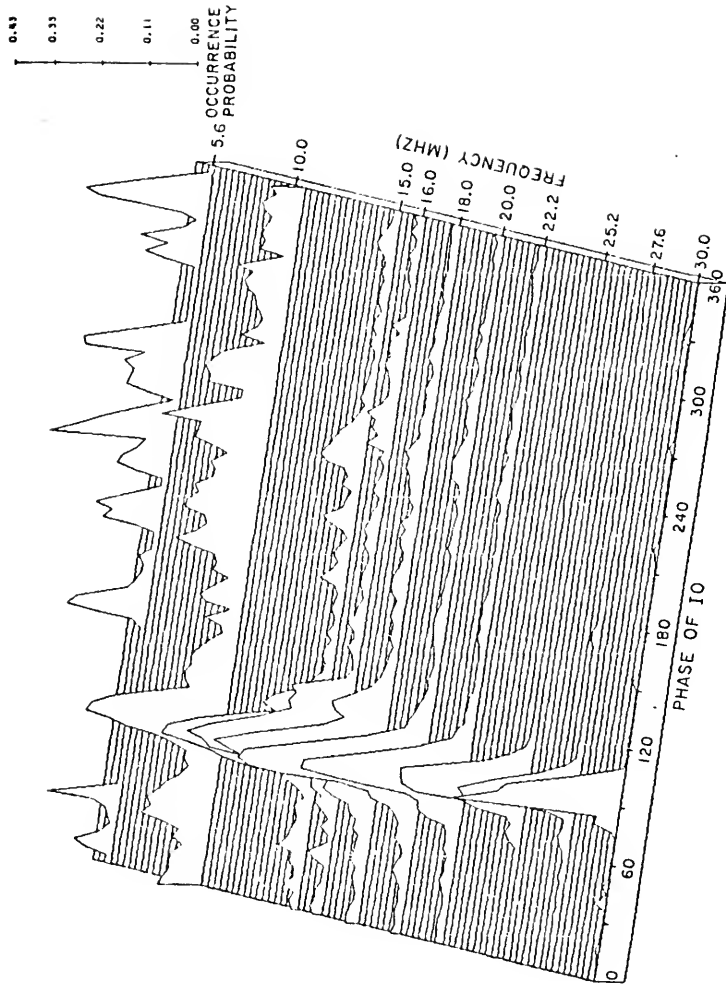


Figure III-17. Perspective view of occurrence probability of source-B storms vs. phase of Io for selected frequencies. This is a different view of Figure III-3.

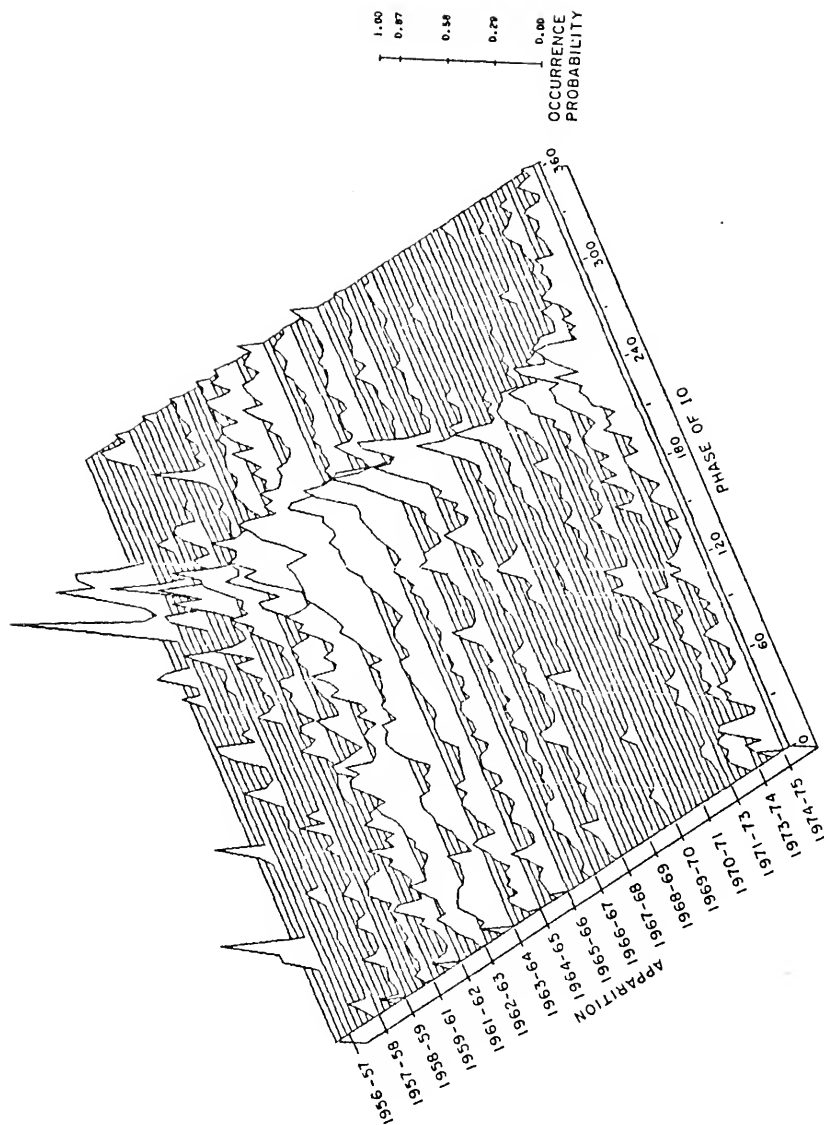


Figure III-18. Perspective view of occurrence probability vs. phase of Io for each apparatus of merged 18, 20, and 22-MHz source-A storms. This is based on the data in Figure III-12.

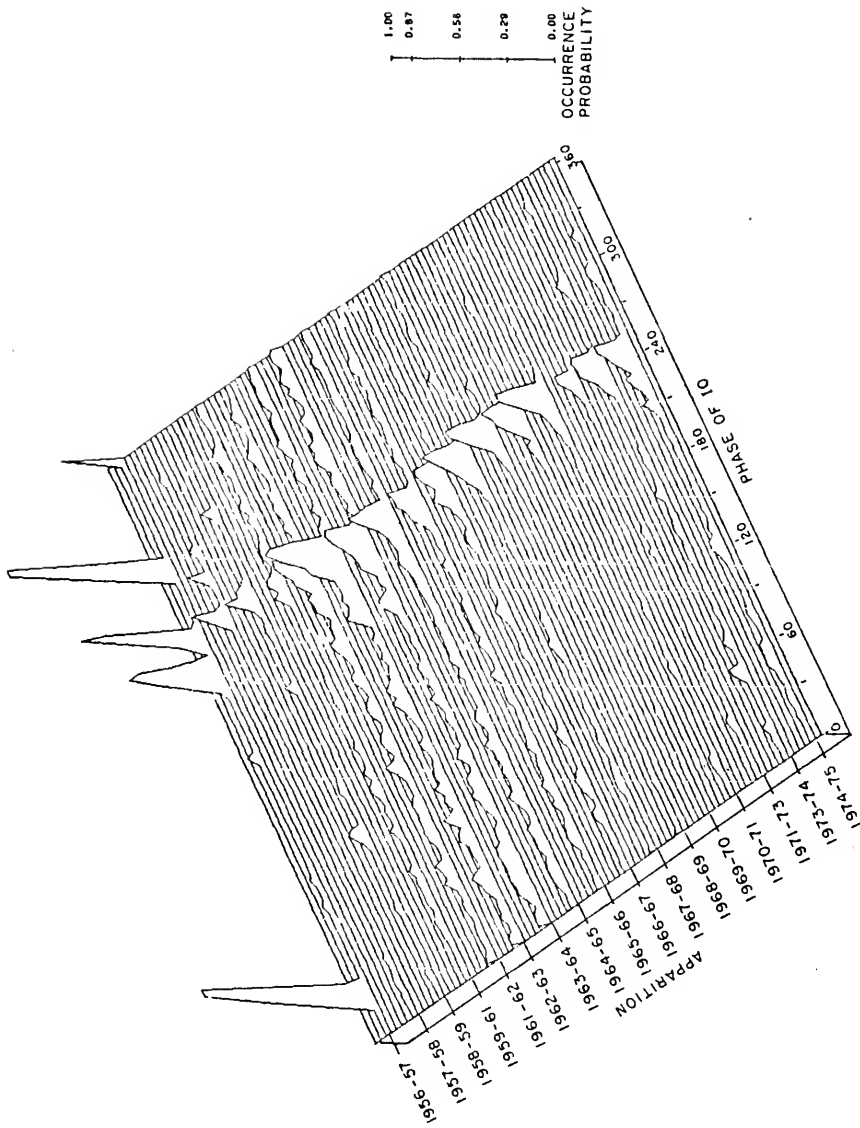


Figure III-19. Perspective view of occurrence probability vs. phase of Io for each apparition of merged 18, 20, and 22-MHz source-C storms. This is based on the data in Figure III-13.

Since all apparitions have been averaged for each of these frequencies, the asymmetries and secondary maxima which are present have some stability through the years.

Skewness is a quality inherent also in the System III longitude picture of the sources. The slow, almost linear increase of source B with increasing  $\lambda_{III}$  coordinates, followed by a more rapid descent, is characteristic above 10 MHz (see Figure III-1). Source C behaves in just the opposite manner, so that sources B and C seem to bracket and build toward source A until an interruption gives them their separate identities. Source A is usually almost symmetrical, with the direction of skew, if any, changing from one apparition to the next according to the rhythm of the centroid motion, as seen in Figure III-7.

Thus far, the source frequency behavior, centroid motions, asymmetries, and bifurcations have been treated only in their relation to System III longitude or the phase of  $I_0$ . Many of these phenomena indicate simultaneous longitude and satellite influence. The next chapter will study the second-order effects in their dependence upon both  $\lambda_{III}$  and  $\phi_{I_0}$ , and reveal other results discovered in the process.



## CHAPTER IV

### TWO-DIMENSIONAL STUDIES

#### 4.1 Projection Methods and Problems

The best means of examining the simultaneous dependence of the decametric radiation on two independent variables is a three-dimensional graph, which is difficult to project onto a two-dimensional page. Historically contour plots, like Figure I-2, have been the choice in the research of many authors (i.e., Alexander et al., 1974; Wilson et al., 1968), including the original work by Bigg (1964). Three difficulties limit the usefulness of these plots: the resolution of the underlying data is hard to ascertain; fine structure is often lost between contour lines unless a confusingly large number of lines is used; and the sense of relief is unsatisfactory for the average observer. Another mode of presentation is the hidden-line, perspective view like Figure III-1. This certainly improves comprehension of relief, but the hidden-line technique can conceal important detail, and deciding exact coordinate locations of a particular feature is troublesome.

A third method has been tried which emphasizes the two-dimensional histogram basis for studying the data. In this process, the two independent variables are divided into intervals, which in turn segments the coordinate plane into rectangular "bins." Since the number of bins increases geometrically when both variables are subdivided, compactness of display of the results in each two-dimensional zone is helpful.

Assignment of a single line-printer character for each bin was the least expensive and most convenient solution. Figure IV-1 demonstrates the technique for an occurrence probability histogram of 18-MHz data from the years 1963-65. In analogy with digital imaging systems each of the characters could be considered as a code for the "brightness" of a picture element or pixel, but the lack of imaging equipment makes it necessary to display only the symbols themselves. The interval sizes used for the System III longitude and the phase of Io axes were  $5^\circ$  each. The print characters are valued according to the order shown at the bottom of the picture. A total of 52 characters are used. A blank means no activity occurred in that bin, and a zero represents the maximum occurrence probability zone. In this case the small amount of data resulted in several zones having the maximum probability of 1.0. The other 50 characters symbolize equally-divided percentiles of the maximum probability, beginning with the "?" representing 0-2 per cent, and ending with the "l" representing 98-99.9 per cent.

This method displays nearly all of the detail attainable from the data, but again there are problems. Comprehension of relief is even more difficult than in the contour plots. Only the contrast between the characters and the blank areas provides any immediate sense of the third dimension. Many times, the data are so diffuse that few blank areas appear. Plots of this nature can be improved by eliminating the less-important lower levels of probability by covering them with low-lying "clouds." This has been done in Figure IV-2, in which all characters below the 10 per cent level have been replaced with blanks. The observer still has trouble distinguishing the shape of the peaks penetrating this cloud layer. Apparently no single plotting method is free of

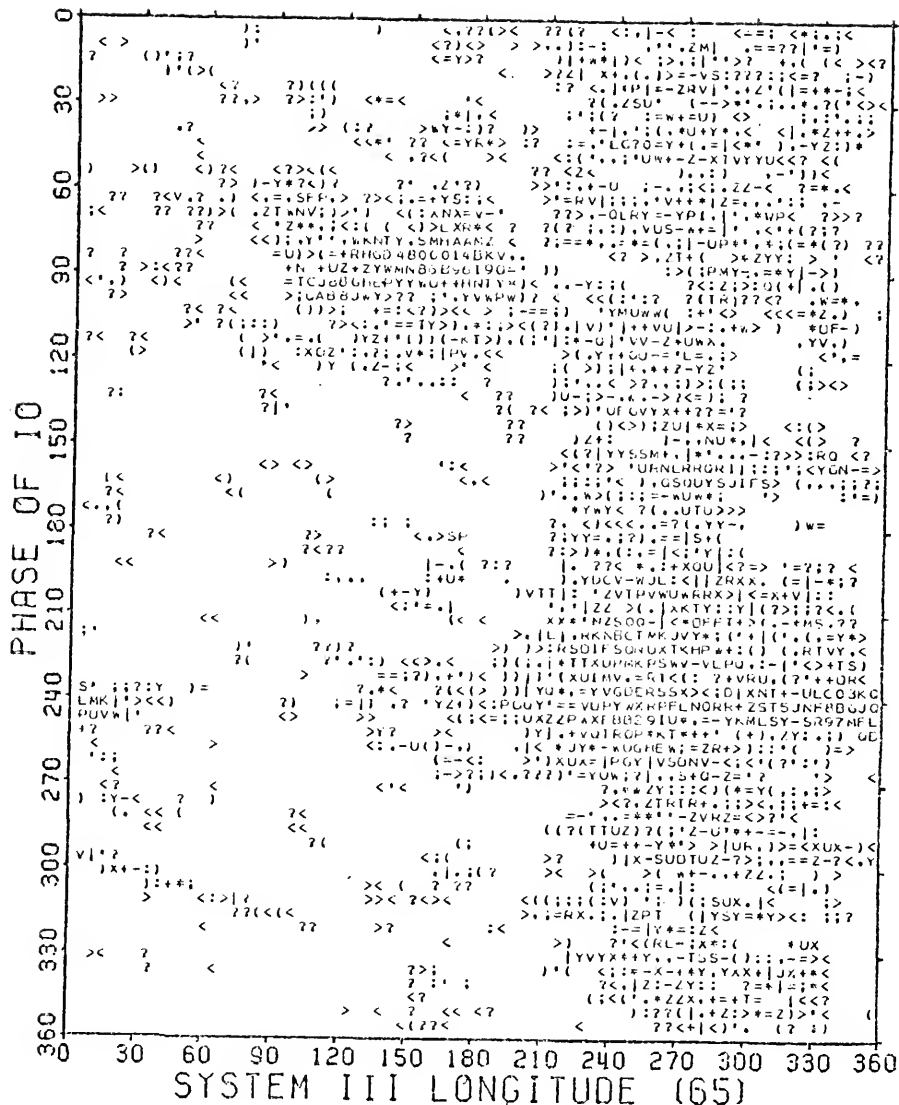


Figure IV-1. Histogram of relative occurrence probability for 5° intervals in System III Longitude (65) and the phase of Io, based on 18-MHz data from the apparitions of 1963-65. The characters represent percentiles of the maximum occurrence probability. Their number and rank from lowest to highest are listed at the bottom.

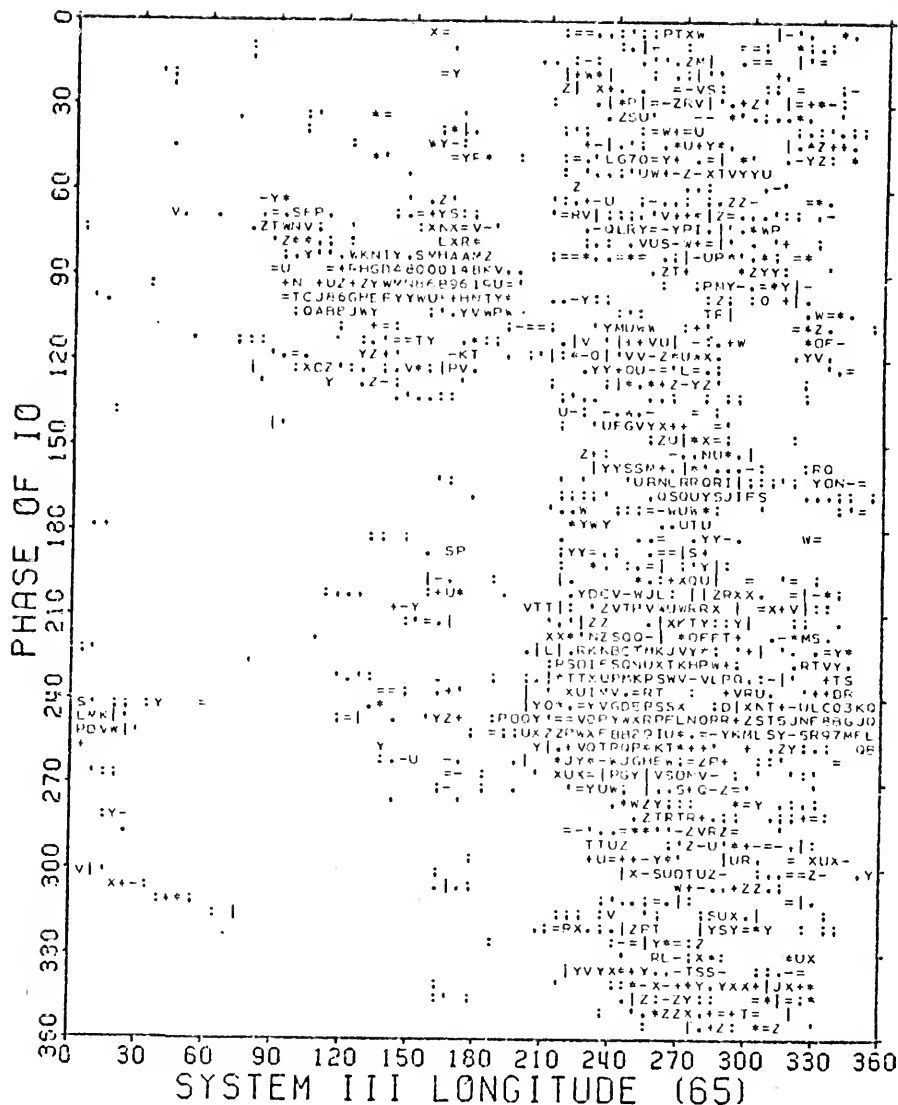


Figure IV-2. Histogram of relative occurrence probability for 5° intervals in System III longitude (65) and the phase of Io, based on 18-MHz data from the apparitions of 1963-65. The characters represent percentiles of the maximum occurrence probability. Their number and rank from lowest to highest are listed at the bottom. All probabilities below 0.100 have been replaced by blanks.

defects. Consequently, a combination of two techniques will generally be used to illustrate the results in the next section. The line-printer-character display provides the resolution needed for observation of second-order effects, and a perspective plot of the same data should provide a perception of the third dimension.

Figures IV-1 and IV-2 also illustrate a problem inherent in the data which all methods of displaying two-dimensional histograms inherit. In low-storm-level regions of the plot linear, downward-sloping structure often stands out. For illustration, see the arrangement of characters in Figure IV-1 beginning at an Io phase around  $300^\circ$  and extending from  $0^\circ$ - $100^\circ$  in System III longitude. This type of feature represents the contribution of a single lengthy radio storm or the superposition of several storms. The slope is characteristic of the family of lines which are described by the elimination of the time parameter from the parametric equations of the time evolution of  $\lambda_{III}$  and  $\phi_{Io}$ . The magnitude of the slope is .234, the ratio of the rotational period of Jupiter to the orbital period of Io. Thus, any two storms having nearly equal  $(\lambda_{III}, \phi_{Io})$  coordinates at some point in their duration will lie along the same lines or bands and will be collectively summed where their tracks in the histogram overlap. The downward-sloping streaks can occur in low-probability areas of even the largest accumulations of data. This is due to a selection effect caused when most of the storms in these regions take place during the active years. Only one complete period of active years has been observed, and the incomplete coverage of the  $\lambda_{III}$ - $\phi_{Io}$  plane prejudices the data. It is expected that inclusion of other active periods will gradually smooth out the ridges and obviate this effect. The high-probability, Io-related source regions will also have some bias

toward more active years, but in their case the inactive years contribute a larger number of storms and, therefore, the coverage is more continuous. Care must be taken to recognize the bias toward inclined structure so that it is not mistaken for phenomena independent of a low probability level.

#### 4.2 Spectral Analysis

Chapter III began the study of source metamorphosis through the frequencies by simultaneous display of the one-dimensional histograms for heavily-observed wavelengths. Since simultaneous comparison of two-dimensional histograms for all frequencies is not possible without a fourth dimension, each frequency will be treated in turn starting at the high end and working down.

Distribution of the data into two-dimensional zones stretches even the largest accumulation of data to the breaking point. Consequently, the frequencies of 5.6 and 25.2 MHz have been dropped from consideration in the present chapter for insufficient data. All of the other frequencies have over 200,000 minutes of observing time. Even at these levels the histograms for the lesser-observed frequencies cannot be meaningfully subdivided beyond 5° intervals for the two independent variables. For accuracy of occurrence probabilities, the calculations have been based on listening and activity times, although the number of events in the zones is still monitored. The uniformity of the data can still be measured from the average and standard deviation of the collection of the listening times in the zones.

Three figures, IV-3 to IV-5, display the 30-MHz results. This end of the decametric spectrum has been chosen as a starting point since future diagrams will become more complicated as frequency decreases.

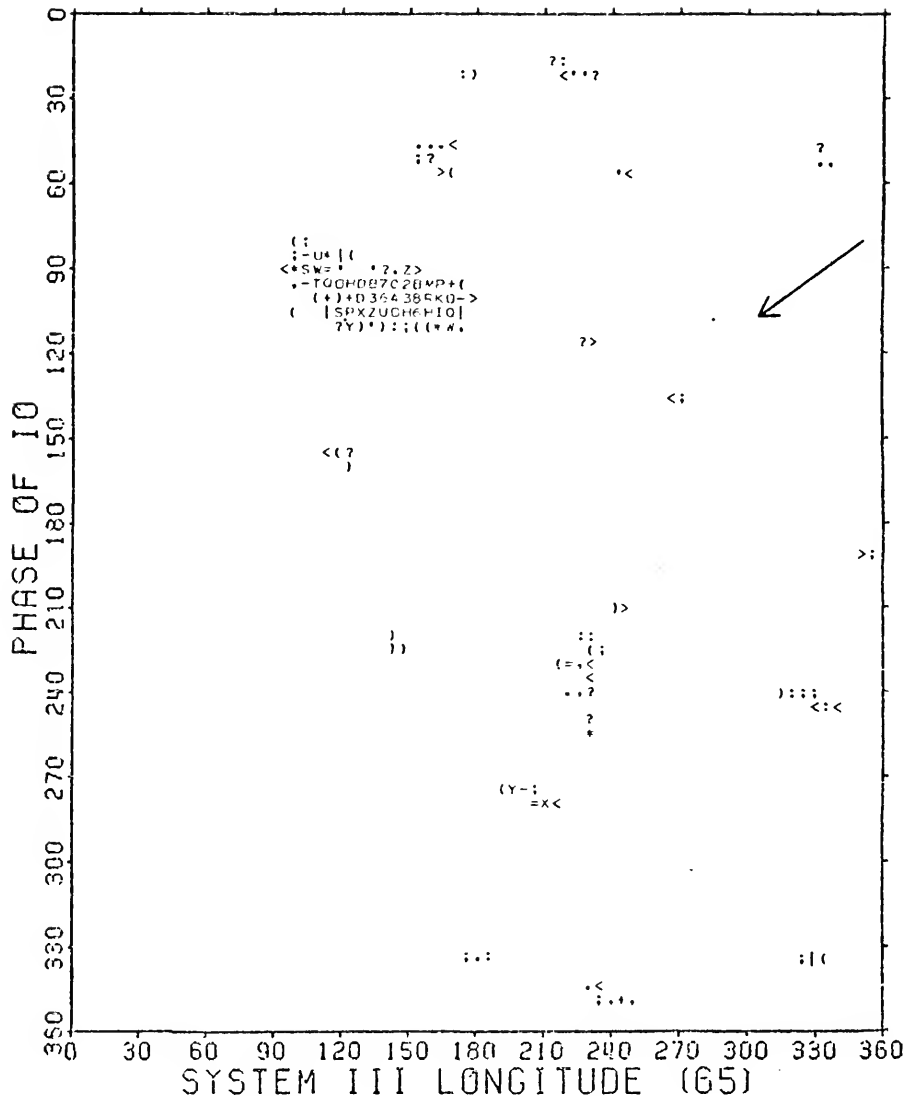


Figure IV-3. Histogram of relative occurrence probability for 5° intervals in System III longitude (65) and the phase of Io, based on all 30-MHz data. The characters represent percentiles of the maximum occurrence probability. Their number and rank from lowest to highest are listed at the bottom. The arrow indicates the direction of view for Figure IV-4.

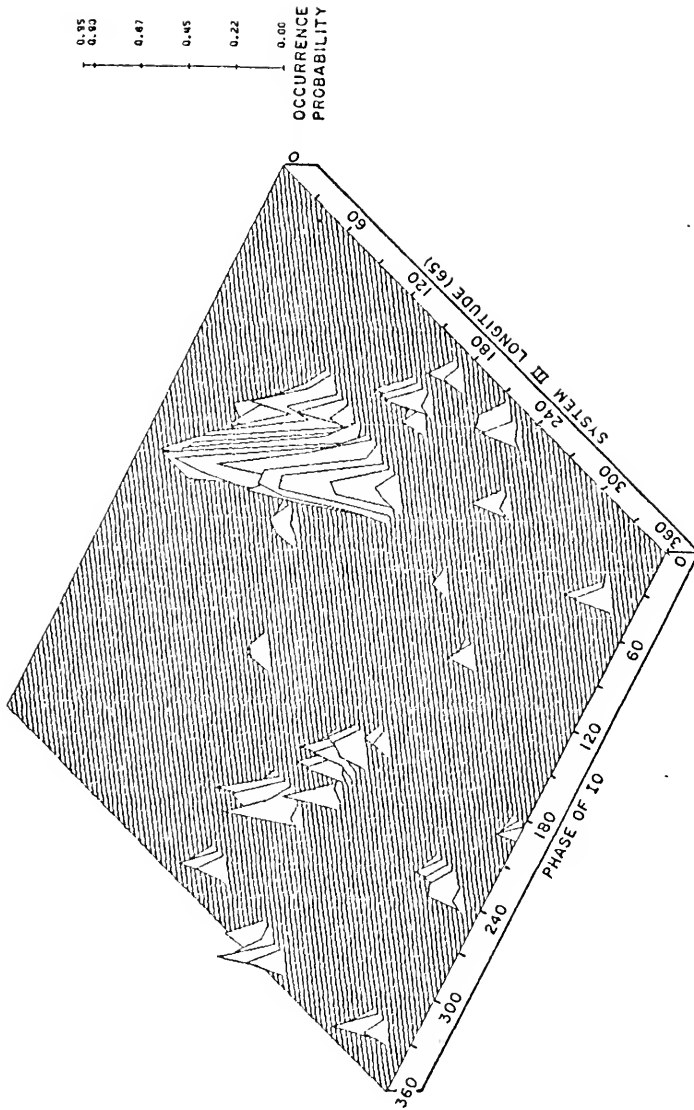


Figure IV-4. Perspective view of 30-MHz occurrence probability for System III longitude vs. the phase of Io. Comparison of distance above the base with the scale at right yields the probability.



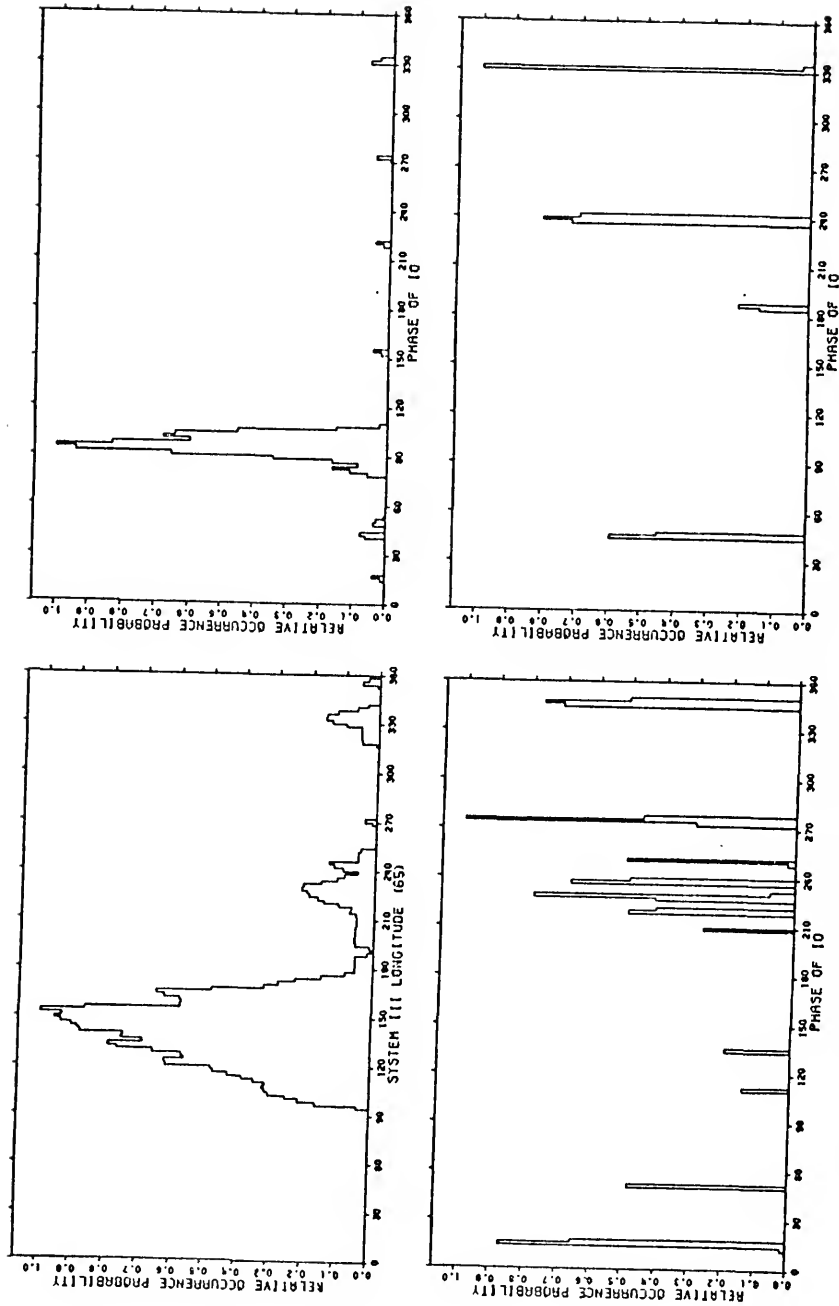


Figure IV-5. Histograms of 30-MHz relative occurrence probability for  $2^\circ$  intervals in, clockwise from upper left, System III longitude (65) and I<sub>0</sub> phase in the isolated source B, C, and A regions.

Figures IV-3 and IV-4 are the detailed presentation and perspective view of the  $\lambda_{III} - \phi_{IO}$  histogram. Zones of  $5^\circ$  by  $5^\circ$  were chosen since division of the 210,000 minutes of observing time into 5184 parts gives an average of 40 minutes and 6 observations per zone, numbers considered too small for further subdivision. Percentiles of relative occurrence probability are represented by the same character sequence as in Figures IV-1 and IV-2. The sequence will remain the same in all of the similar plots in this chapter. The arrow in Figure IV-3 indicates the direction of observation used in Figure IV-4. This angle was chosen as a standard for all of the perspective plots, since it is the most beneficial for revealing details to be discussed later.

The outstanding and almost the only feature in either figure is the  $IO$ -related, source-B radiation. Though surrounded by emptiness, the source-B island still exhibits a high degree of probability, since the maximum occurrence probability is 0.95. Its shape in the  $\lambda_{III} - \phi_{IO}$  plane of Figure IV-3 is typical. There is an elongated smear of data from  $75^\circ$  to  $180^\circ$  in  $\lambda_{III}$  and from  $85^\circ$  to  $110^\circ$  in  $\phi_{IO}$ . This is augmented by a projection extending to the upper left. While the upper edge is irregular in shape, the lower edge cuts off sharply at  $\phi_{IO}$  of  $110^\circ$ , which explains the slow rise and sharp cutoff of source B in the one-dimensional histogram.

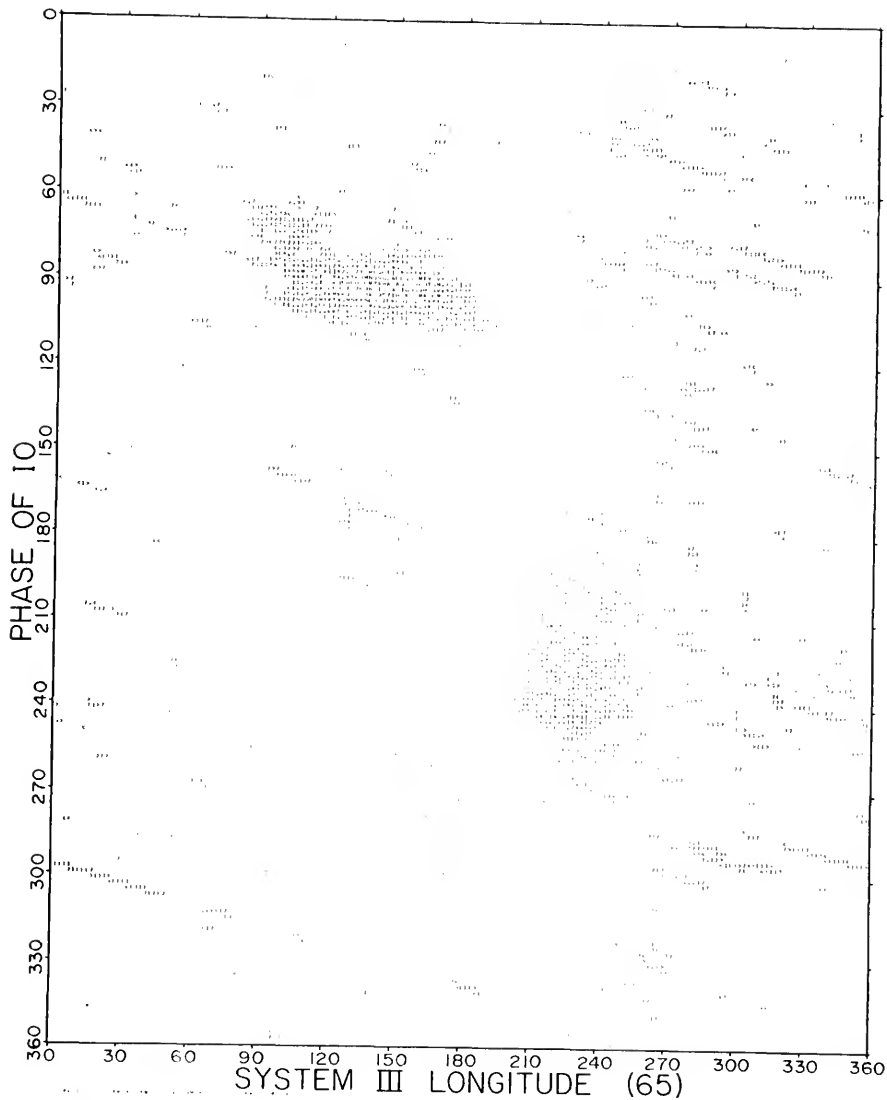
In the traditional locations for sources A and C ( $\phi_{IO} = 240^\circ$  and  $\lambda_{III} = 240^\circ$  and  $330^\circ$ , respectively) there are slight indications of storm activity. These are not significantly different from other storms scattered elsewhere. The dispersion at first appears random, but no storms occur in what is called the "null zone" to the left side of source B in Figure IV-3. In this  $\lambda_{III}$  range, no  $IO$ -related source appears

until source D emerges around 16 MHz. Since the other Io-related sources persist to much higher frequencies, this suggests that the scattered radiation may be harbingers of these sources, while storms preceding source D's appearance will not appear until lower frequencies are encountered. The small number of outlying storms makes this statement rather speculative.

The graphs in Figure IV-5 are 2°-interval histograms for System III longitude and for the phase of Io in isolated source B, A, and C regions. Although these plots did not specifically appear in the previous chapter, they served as the basis for the 30-MHz parts of Figures III-1 and III-3 to III-5. Figure IV-5 and similar figures in this chapter will serve to facilitate comparison of features between the one- and two-dimensional histograms. In the 30-MHz case the source-B peaks are obvious in the upper two histograms and the lack of concentrated storms in the isolated A and C areas makes the lower histograms seem erratic. The System III longitude histogram reinforces the identification of the scattered radiation as precursors of sources A and C, since secondary peaks appear at the appropriate longitudes.

Between 30 and 27 MHz Io-related source A appears, as is shown in Figures IV-6 and IV-7. Figure IV-6 has more detail than its 30-MHz counterpart since the larger amount of observing and activity time at 27 MHz permits division of the data into 2° by 2° zones. Even with the smaller intervals, there is still an average of 49 minutes of observation and 18 separate listening periods for each zone. The individual characters are difficult to see, but for cursory analysis the more important feature is the relationship between the blank and lettered areas.

Figure IV-6. Histogram of relative occurrence probability for  $2^\circ$  intervals in System III longitude (65) and the phase of  $I_0$ , based on all 27-MHz data. The characters represent percentiles of the maximum occurrence probability. Their number and rank from lowest to highest are listed at the bottom.



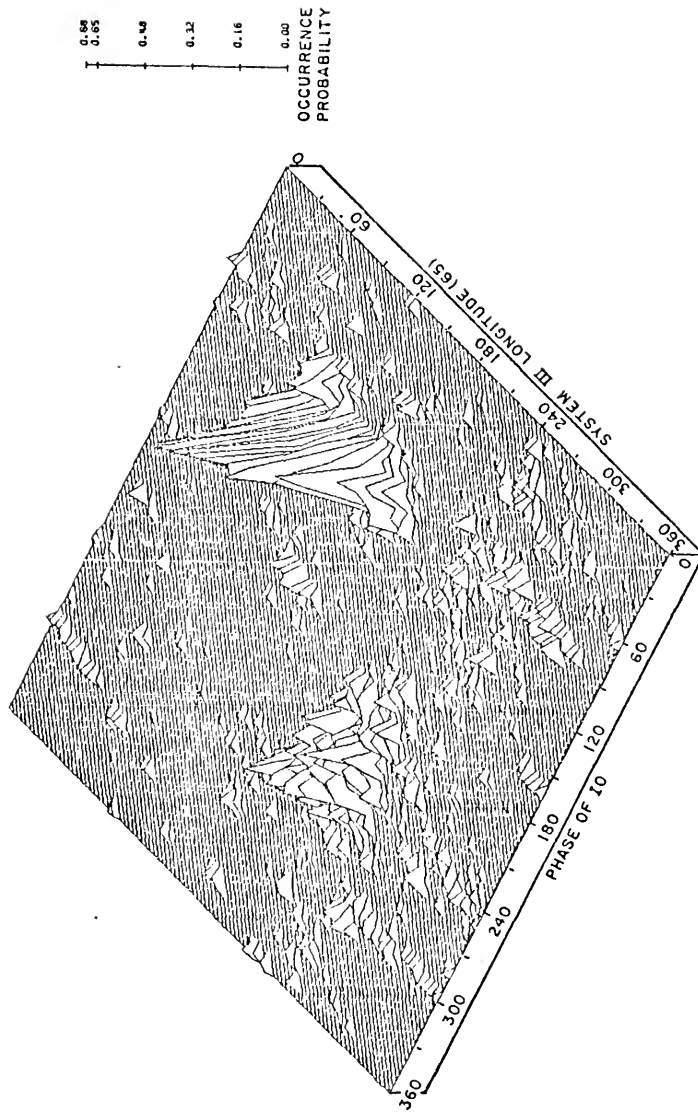


Figure IV-7. Perspective view of 27-MHz occurrence probability for System III longitude vs. the phase of Io. Comparison of distance above the base with the scale at right yields the probability.

Source B has changed slightly from its 30-MHz appearance. Not only is there a projection to the upper left, but a low-probability area has appeared at the upper right. The combination of these two regions explains the bifurcated peak at  $70^\circ$  in the Io-phase histogram of source B in Figure IV-8. Although source A has just appeared and is fairly weak, the corresponding Io-phase histogram already exhibits the secondary peaks and asymmetry discussed in the previous chapter. The slow rise of source A with increasing Io phase corresponds to the slope leading up to the peak in Figure IV-7, and it extends over the entire  $30^\circ$  longitudinal width of the source. The maximum probability is not centered in this range, but occurs at a slightly lower longitude. It is difficult to say whether the secondary peaks come from bumps in the slope or ridges extending across the width. Assuming that the cause for the secondary peaks is the same at lower frequencies, their origins will be easier to determine in the next set of figures.

The most-observed frequency is 22 MHz, with an average of 80 minutes and 30 observations per  $2^\circ$  by  $2^\circ$  zone. This seems poetically just, since the original discovery of Jupiter's radio emission was made at this frequency. The increase in monitoring time from 27 to 22 MHz is also justified by the larger amount of activity, displayed in Figures IV-9 and IV-10. To unclutter Figure IV-9 (and other similar figures at lower frequencies) all zones having probabilities less than the average occurrence probability, defined as the total activity time divided by the total listening time, have been blanked out. In this case the cutoff value is 0.041.

Between 27 and 22 MHz, Io-related source C has emerged as well as profuse Io-independent radiation in the A and C regions. The non-Io-related

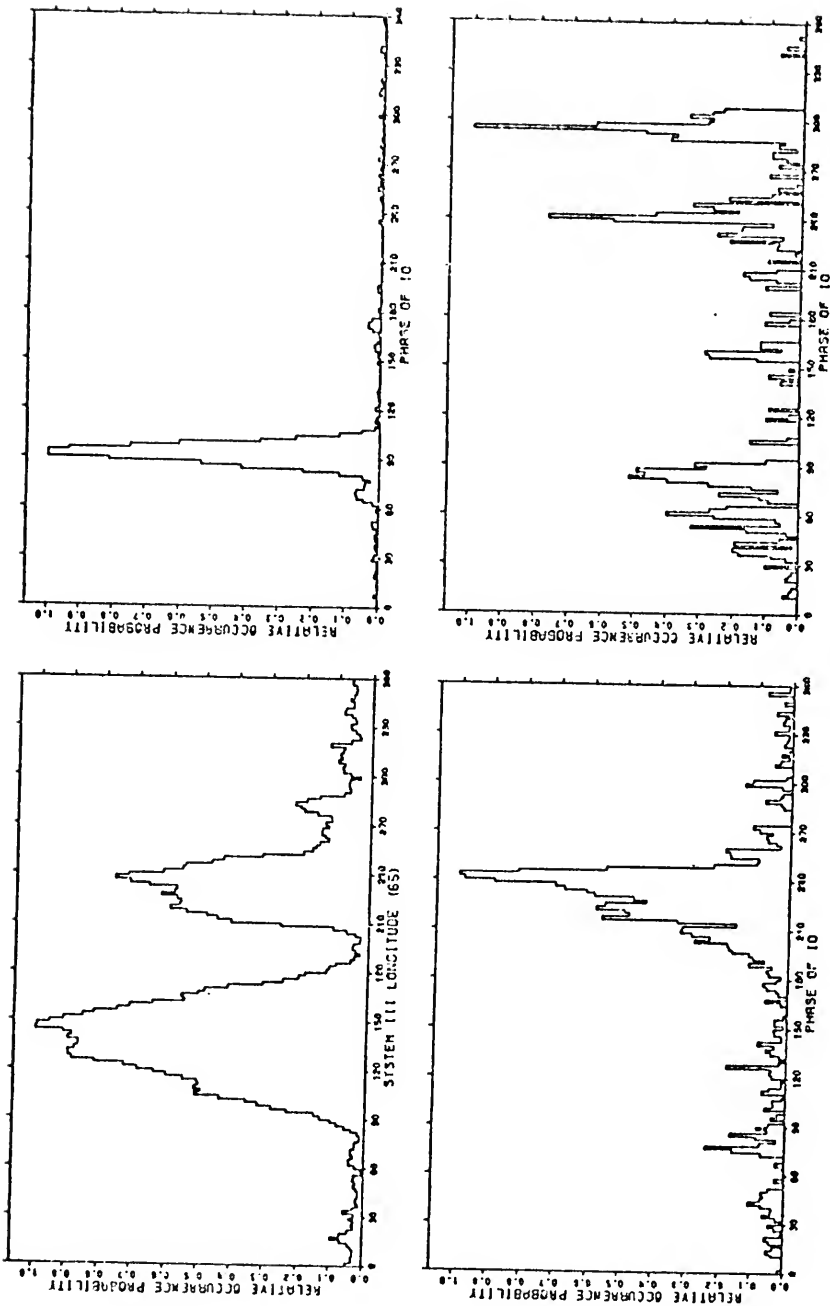
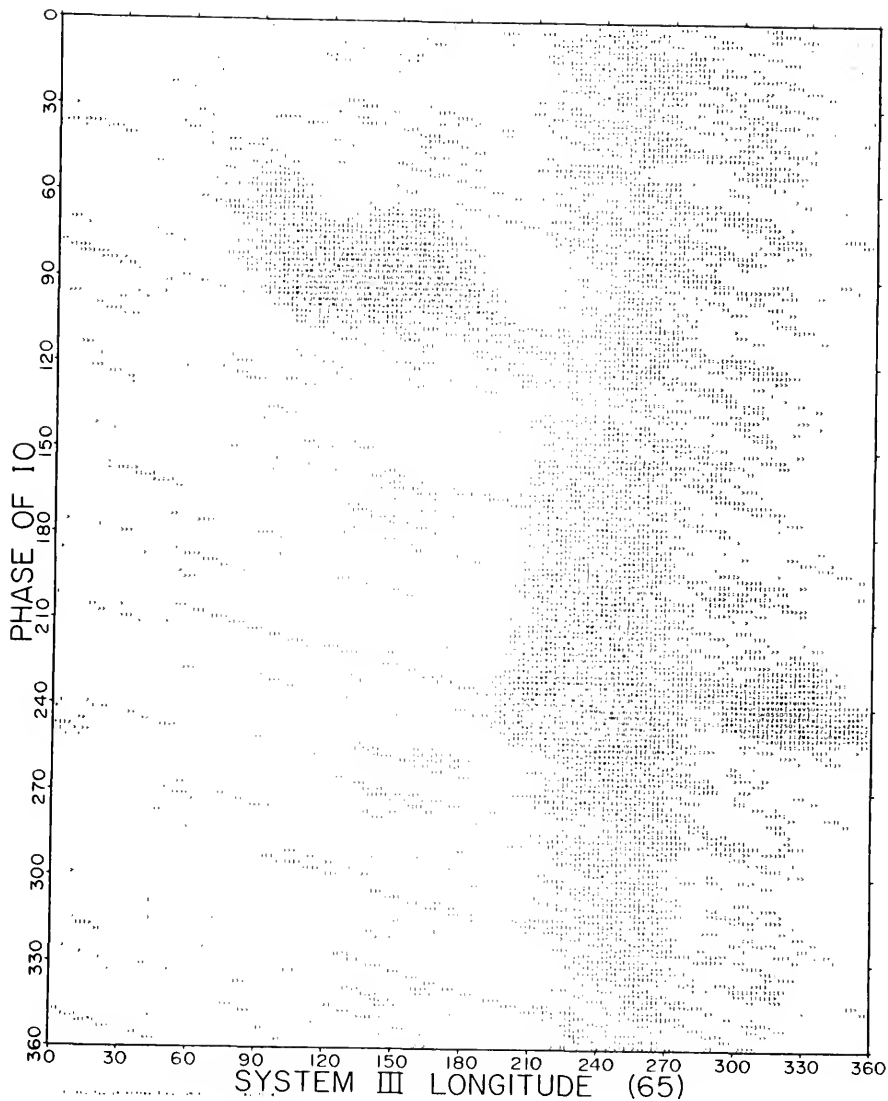


Figure IV-8. Histograms of 27-MHz relative occurrence probability for 2° intervals in, clockwise from upper left, System III longitude (65) and Io phase in the isolated source B, C, and A regions.



Figure IV-9. Histogram of relative occurrence probability for  $2^\circ$  intervals in System III longitude (65) and the phase of  $I_o$ , based on all 22-MHz data. The characters represent percentiles of the maximum occurrence probability. Their number and rank from lowest to highest are listed at the bottom. All probabilities below 0.041 have been replaced by blanks.



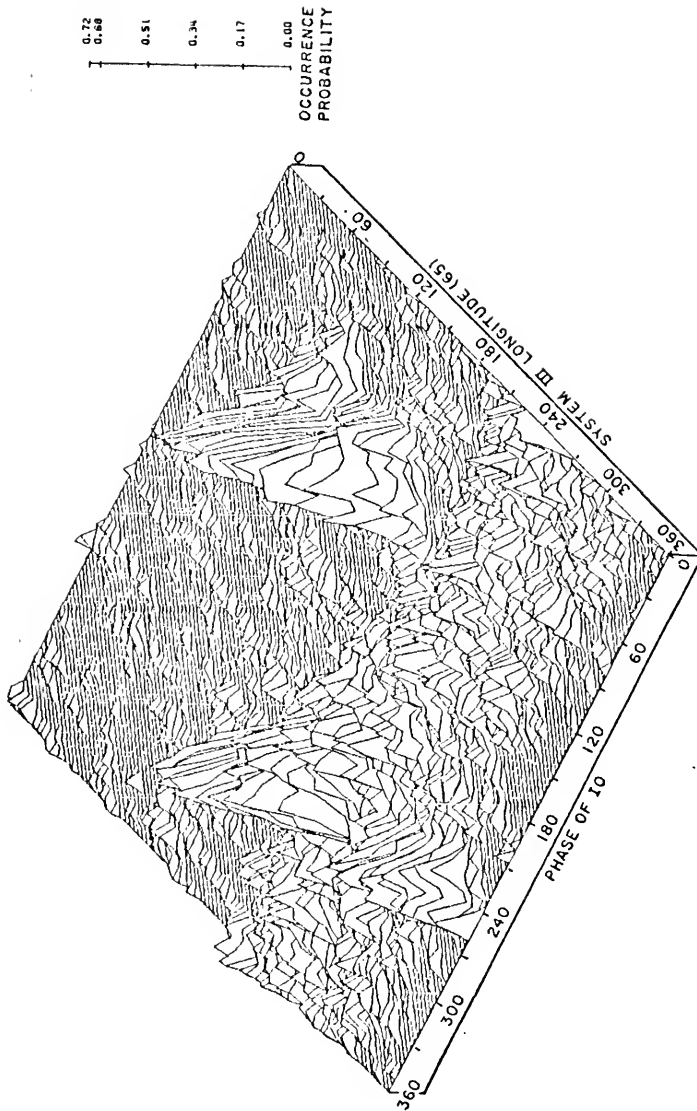


Figure IV-10. Perspective view of 22-MHz occurrence probability for System III longitude vs. the phase of  $I_0$ . Comparison of distance above the base with the scale at right yields the probability.

radiation shows the downward-sloping structure characteristic of low-probability regions. The Io-phase secondary peaks preceding sources A and C in Figure IV-11 coincide with ridges usually extending across the entire longitudinal width of the source. Whether they are artifacts of the active years or persistent through the other periods will be studied in the chronology section of this chapter.

As is true at 27 MHz, the bifurcation and asymmetry of the Io-phase, source-B peak in Figure IV-11 are products of the projections extending to the upper right and upper left in Figure IV-9. Unlike the situation at the higher frequency, the main body of the source extends to lower values of Io phase, but the sharp cutoff at the higher Io-phase edge remains at the same position. The shape of Io-related source C should also be mentioned. In this case an interesting bulge extends to lower values of Io phase, ending around  $220^\circ$ .

There is not too much change between the 22-MHz picture and the 20-MHz data presented in Figures IV-12 to IV-14. The increased probability of the non-Io-related radiation from sources A and C makes observation of Io-related source C in Figure IV-13 more confusing, but its growth is still evident from the higher probabilities and more prominent extension past  $360^\circ$  and into the low longitudes. The increased activity has also raised the average occurrence probability cutoff to 0.059, but the number of observations and listening time per zone have dropped to 16 and 41 minutes respectively. The projection to the upper left of source B in Figure IV-12 has increased in size, while the indentation between the two bulges has been partially filled with a small number of storms. This helps to explain the lack of bifurcation in Io-phase of source B in Figure IV-14, but conspicuous secondary peaks are absent from the other sources as well,

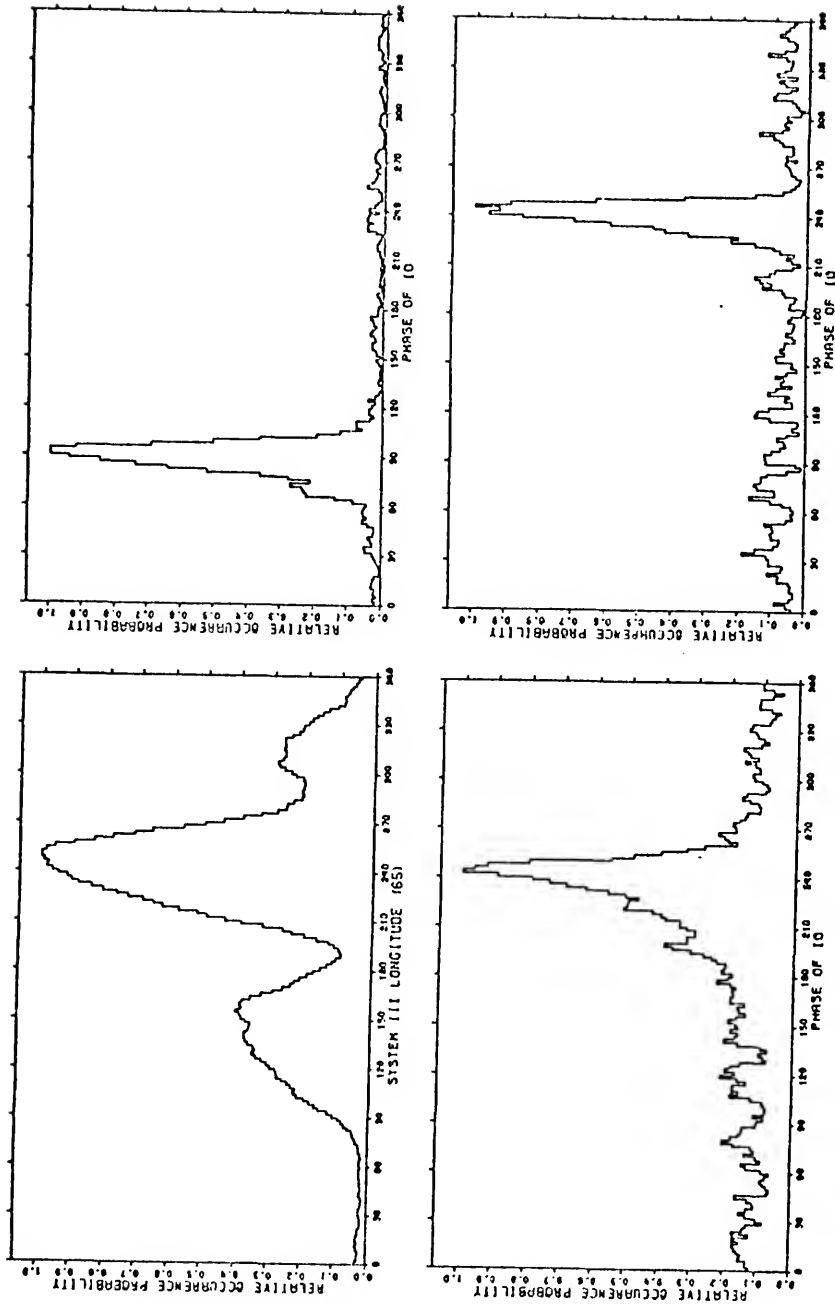
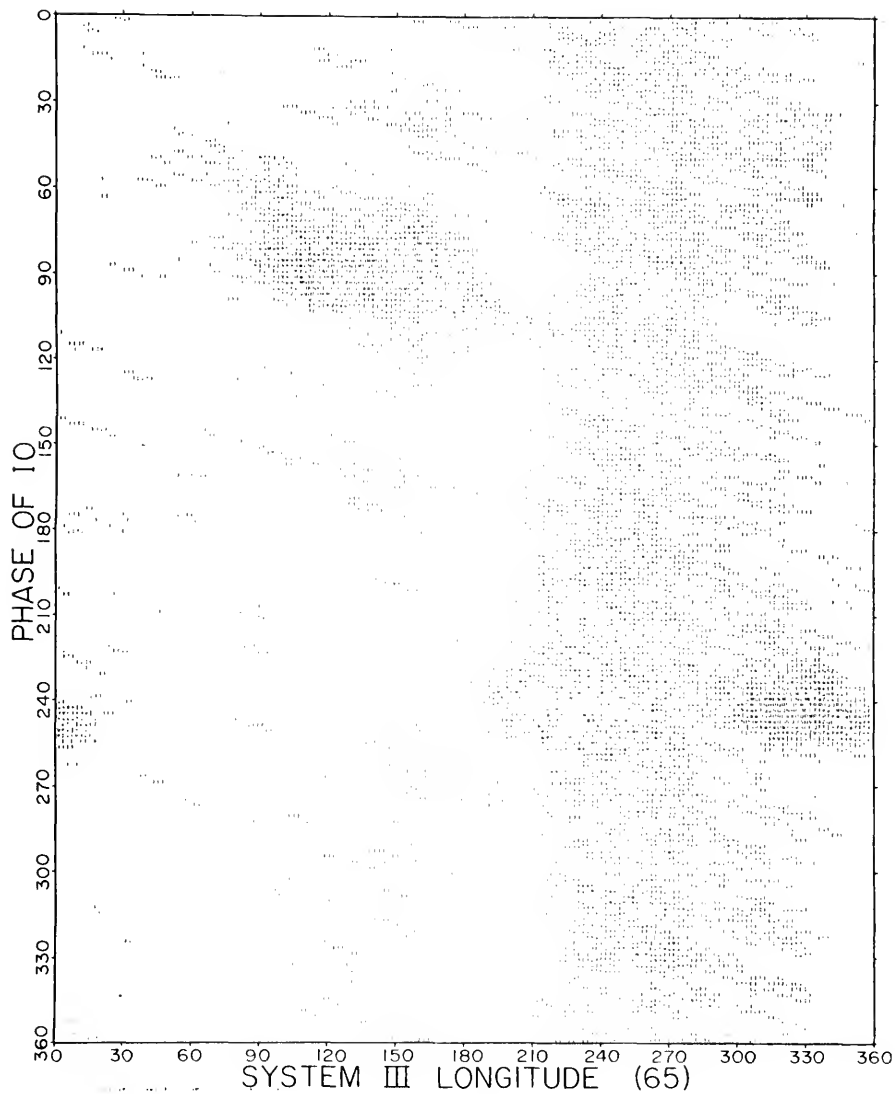


Figure IV-11. Histograms of 22-MHz relative occurrence probability for  $2^\circ$  intervals in, clockwise from upper left, System III longitude (65) and Io phase in the isolated source B, C, and A regions.

Figure IV-12. Histogram of relative occurrence probability for  $2^\circ$  intervals in System III longitude (65) and the phase of  $I_0$ , based on all 20-MHz data. The characters represent percentiles of the maximum occurrence probability. Their number and rank from lowest to highest are listed at the bottom. All probabilities below 0.059 have been replaced by blanks.



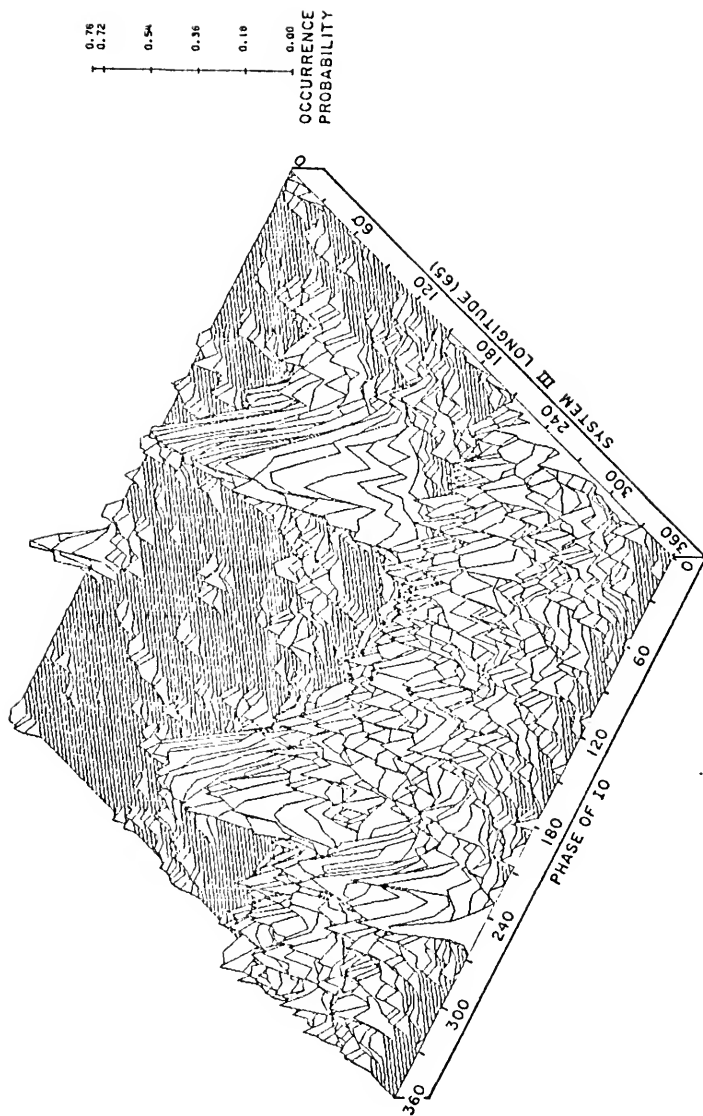


Figure IV-13. Perspective view of 20-MHz occurrence probability for System III longitude vs. the phase of Io. Comparison of distance above the base with the scale at right yields the probability.



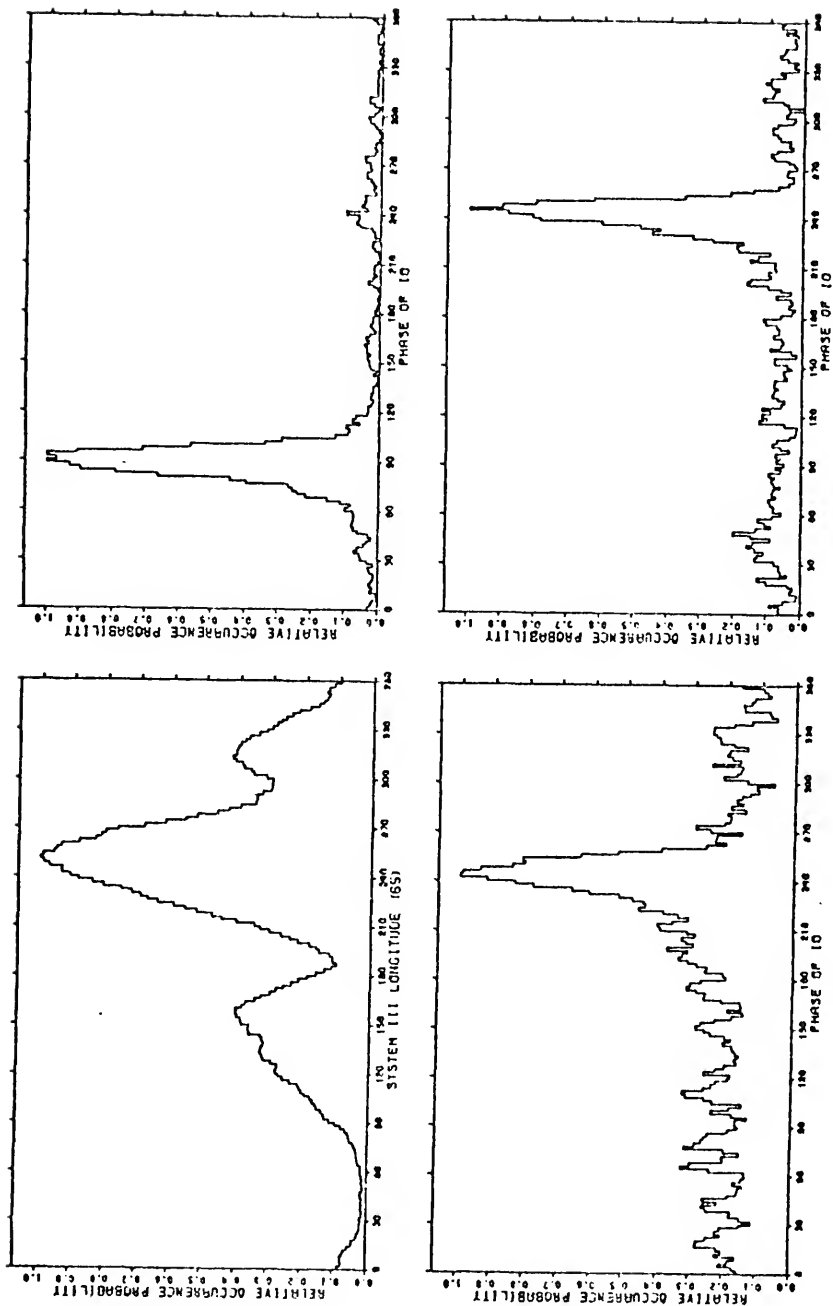


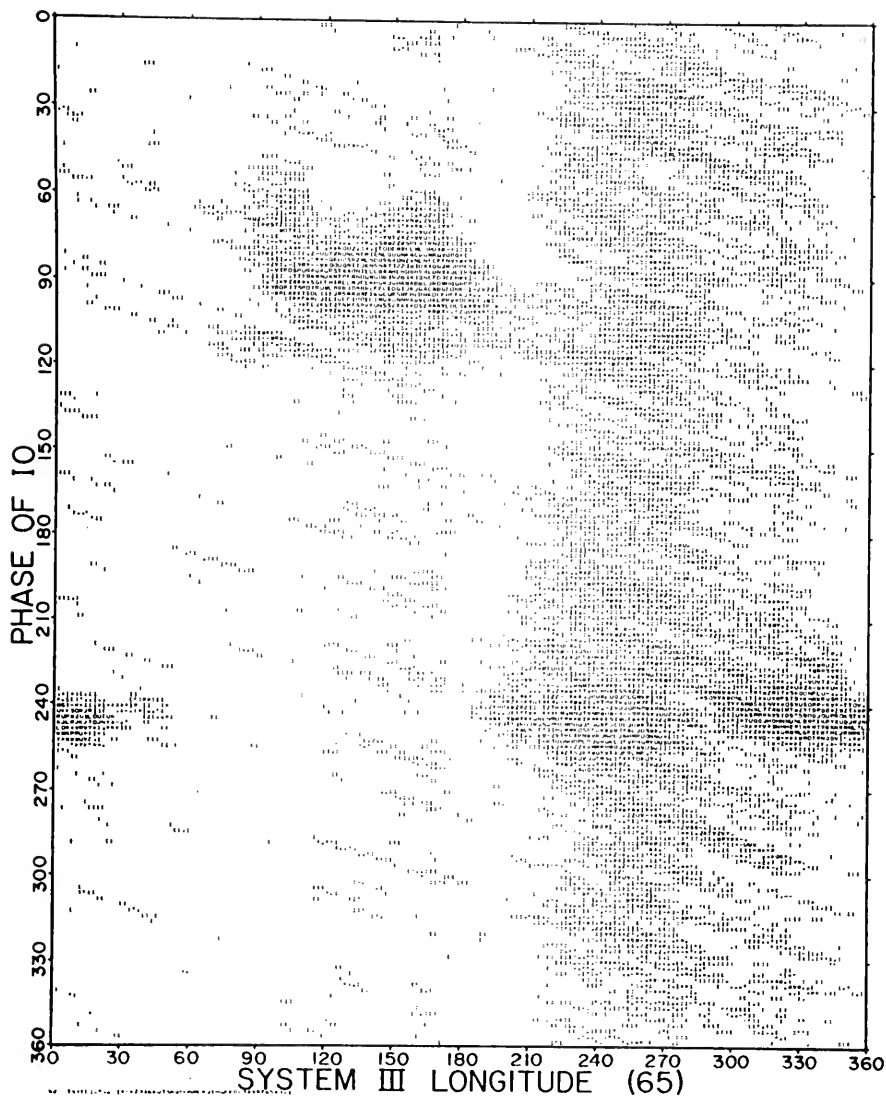
Figure IV-14. Histograms of 20-MHz relative occurrence probability for  $2^\circ$  intervals in, clockwise from upper left, System III longitude (65) and Io phase in the isolated source B, C, and A regions.

although the asymmetry is still unmistakable. This argues for the random superposition origin of the secondary maxima.

The 18-MHz data have a still higher level of activity, elevating the average occurrence probability to 0.065, and it has been monitored slightly more than its 20-MHz predecessor with an average of 20 observations and 53 minutes of listening in each 2°-square zone. Previous figures have shown some signs of non-Io-related radiation in the source-B longitudes, but Figure IV-15 has a consistent low level of radiation scattered in the 120°-180° longitude region. There is a definite lack of Io-independent radiation in the 70°-120° region, even though the Io-related part of source B extends over to the 70° longitude. One major change has taken place between 20 and 18 MHz. The Io-related part of B no longer cuts off sharply at an Io phase of approximately 100° but continues on to 120°. As a result the Io-phase, source-B peak in Figure IV-17 is now more symmetric and trifurcated. The source A and C regions remain virtually the same as before. Source C has increased in probability and extended farther into the low-longitude region. Some secondary peaks have reappeared in Figure IV-17 preceding Io-related source A, but the surrounding fluctuation of Io-independent radiation makes them undistinguished.

The shorter total monitoring time at 16 MHz necessitates returning to 5° by 5° zones for the histograms of Figures IV-18 and IV-19. The time has been divided into an average of 68 minutes per zone contributed by 10 observations. The average occurrence probability cutoff for Figure IV-18 is 0.067. Figures IV-18 to IV-20 do not reveal much change in sources A and C, although the non-Io-A radiation has higher probabilities and a more erratic appearance than at 18 MHz. This can be blamed on the lower data levels. The alteration of source B is more noticeable. The

Figure IV-15. Histogram of relative occurrence probability for  $2^\circ$  intervals in System III longitude (65) and the phase of  $I_0$ , based on all 18-MHz data. The characters represent percentiles of the maximum occurrence probability. Their number and rank from lowest to highest are listed at the bottom. All probabilities below 0.065 have been replaced by blanks.



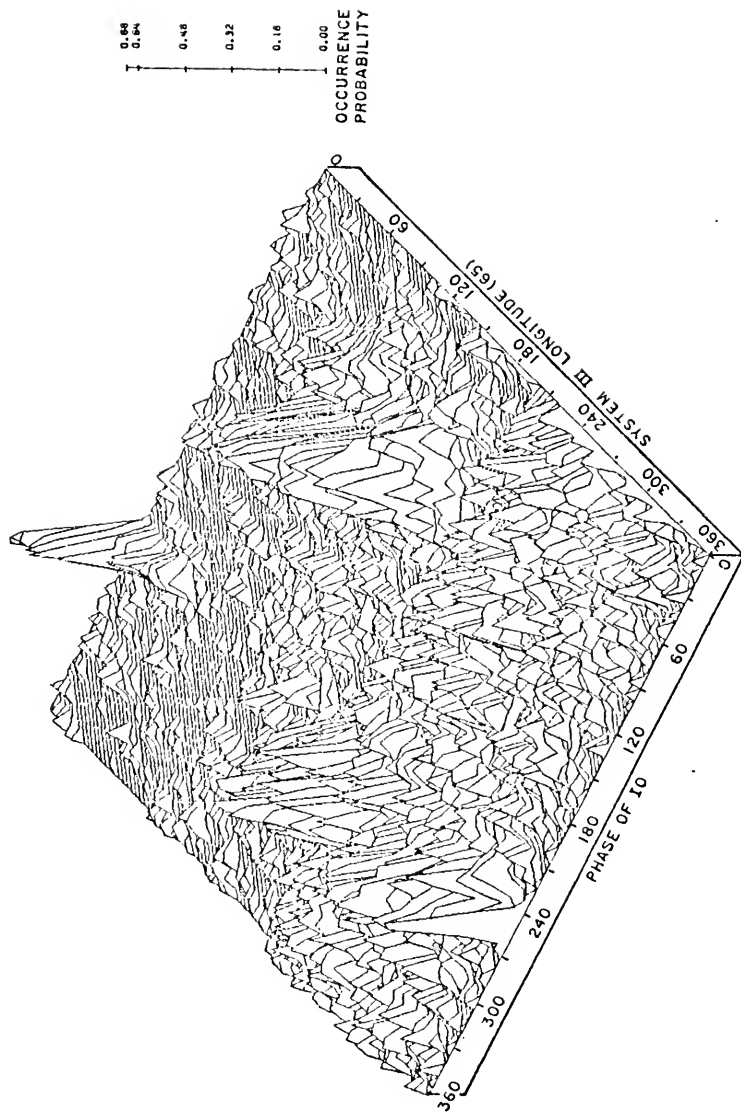


Figure IV-16. Perspective view of 18-MHz occurrence probability for System III longitude vs. the phase of  $I_0$ . Comparison of distance above the base with the scale at right yields the probability.

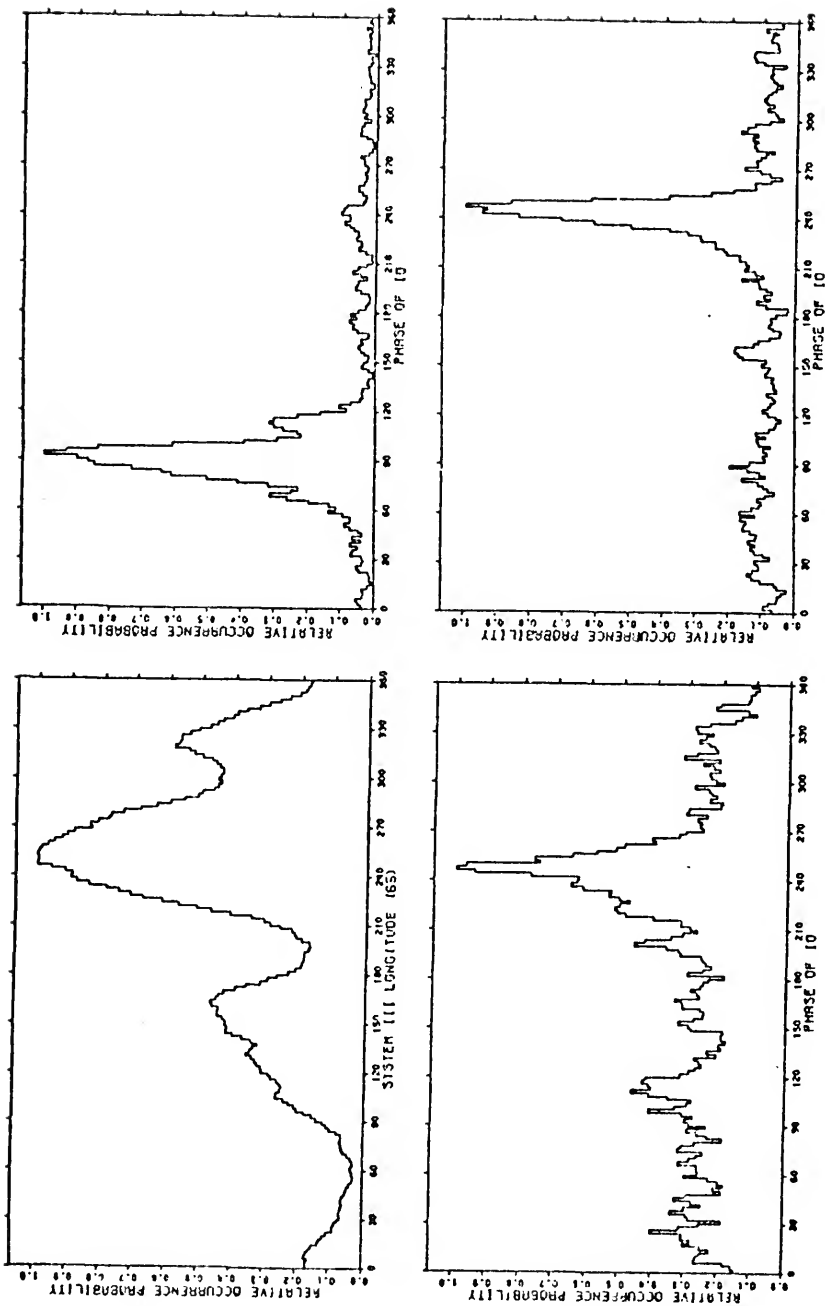
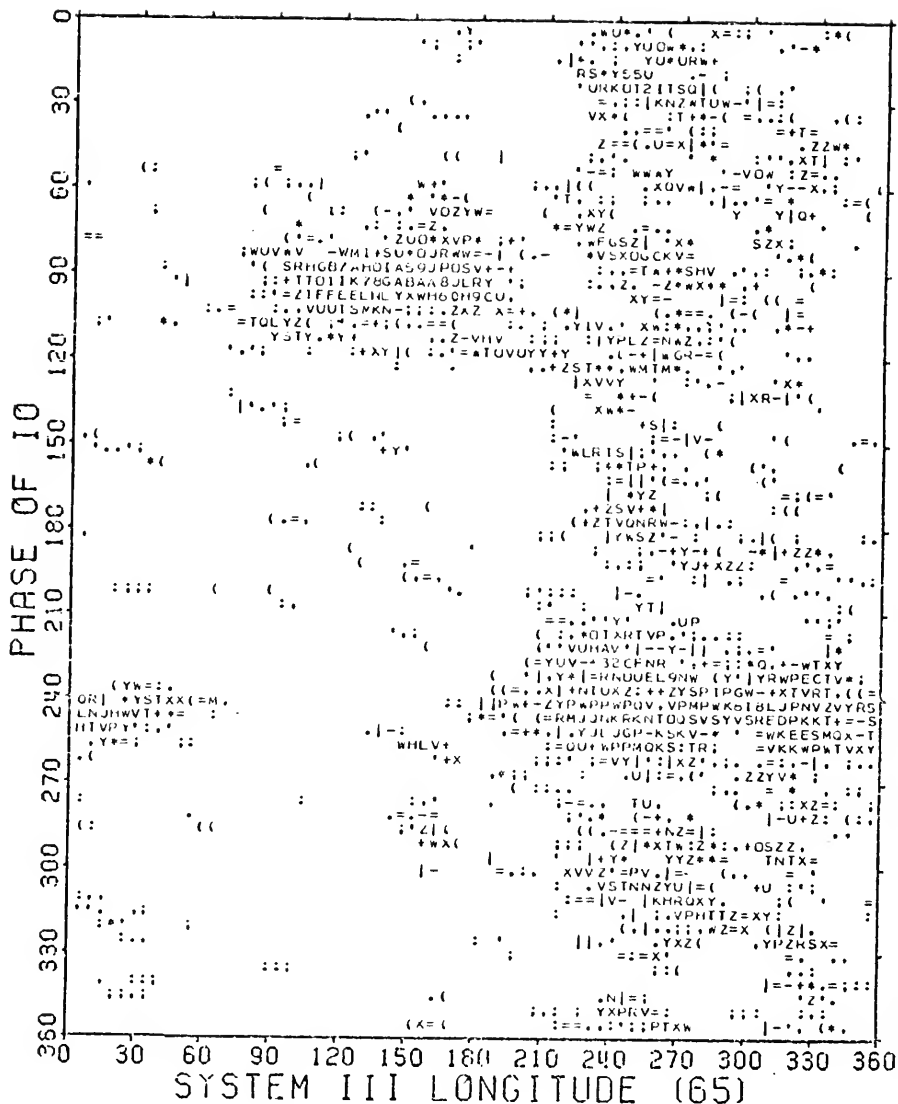


Figure IV-17. Histograms of 18-MHz relative occurrence probability for  $2^\circ$  intervals in, clockwise from upper left, System III longitude (65°) and I<sub>0</sub> phase in the isolated source B, C, and A regions.



52 7(>)(::'..=|\*~+Z YXWVUTSRQPUNMLKJiHGFEUCBA9876543210

Figure IV-18. Histogram of relative occurrence probability for 5° intervals in System III longitude (65) and the phase of Io, based on all 16-MHz data. The characters represent percentiles of the maximum occurrence probability. Their number and rank from lowest to highest are listed at the bottom. All probabilities below 0.067 have been replaced by blanks.

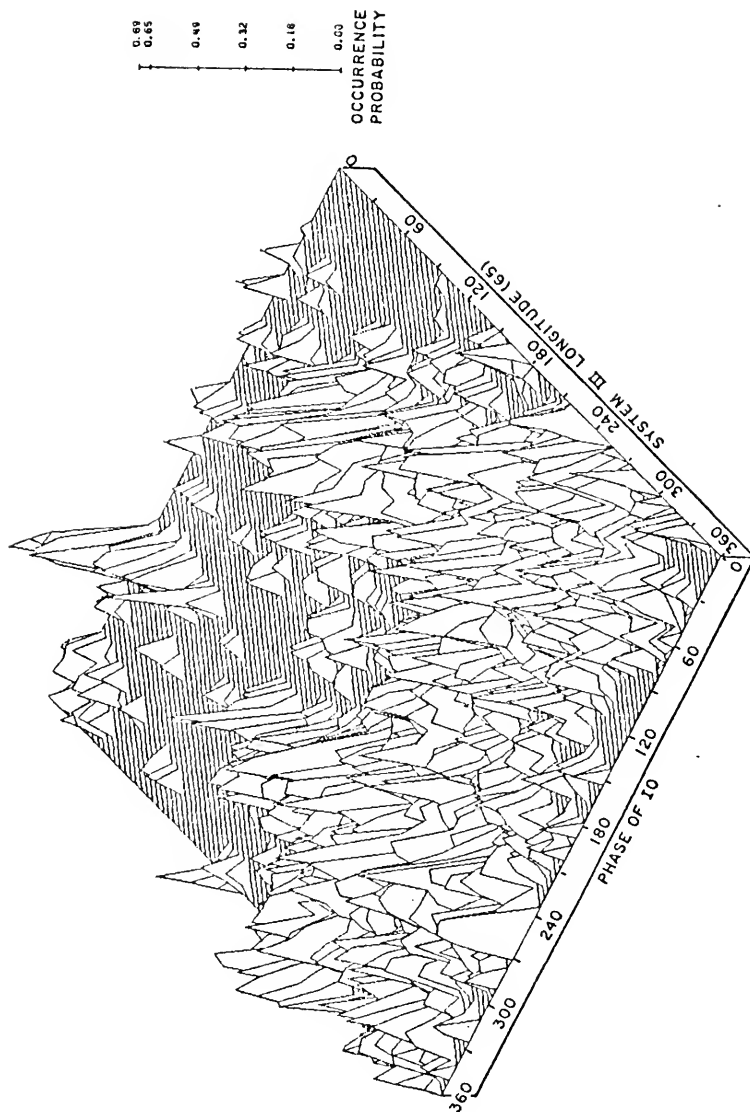


Figure IV-19. Perspective view of 16-MHz occurrence probability for System III longitude vs. the phase of  $I_0$ . Comparison of distance above the base with the scale at right yields the probability.



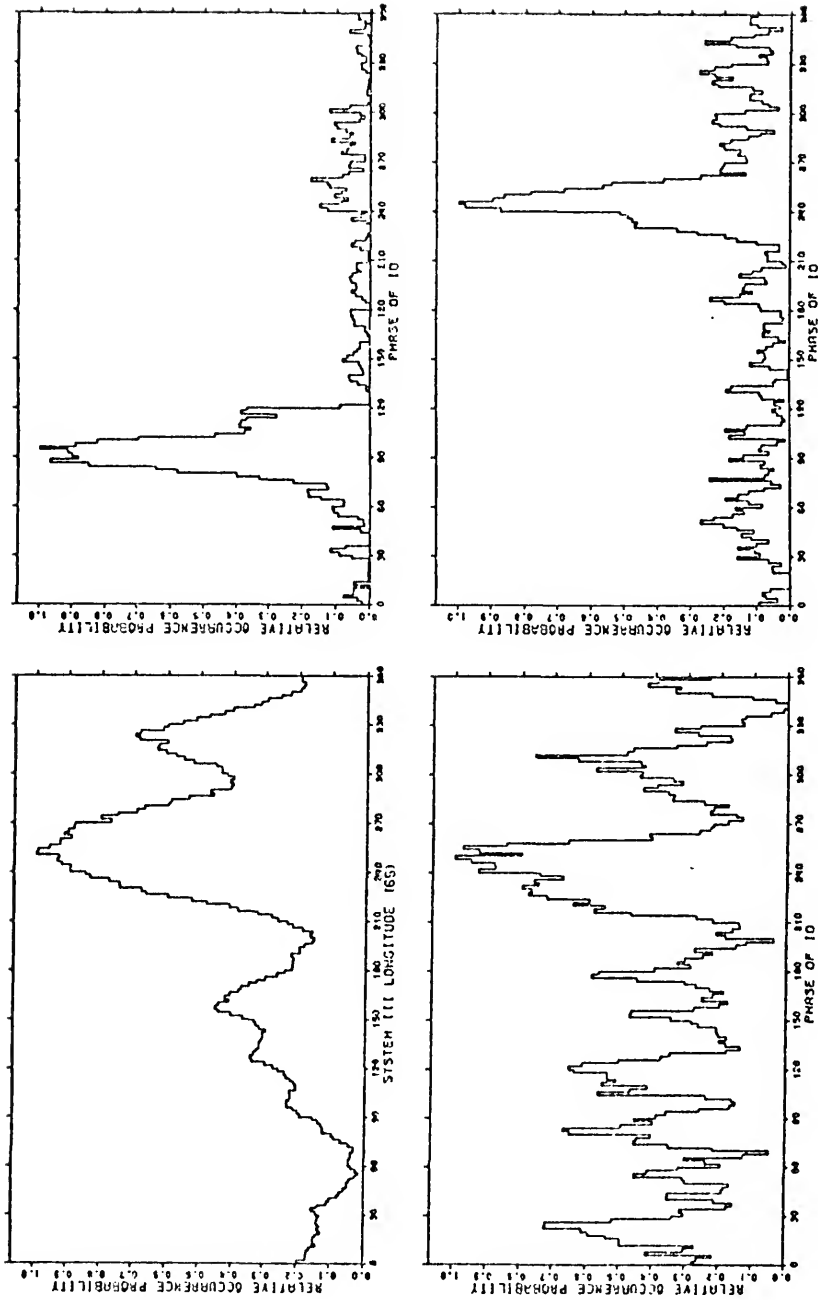
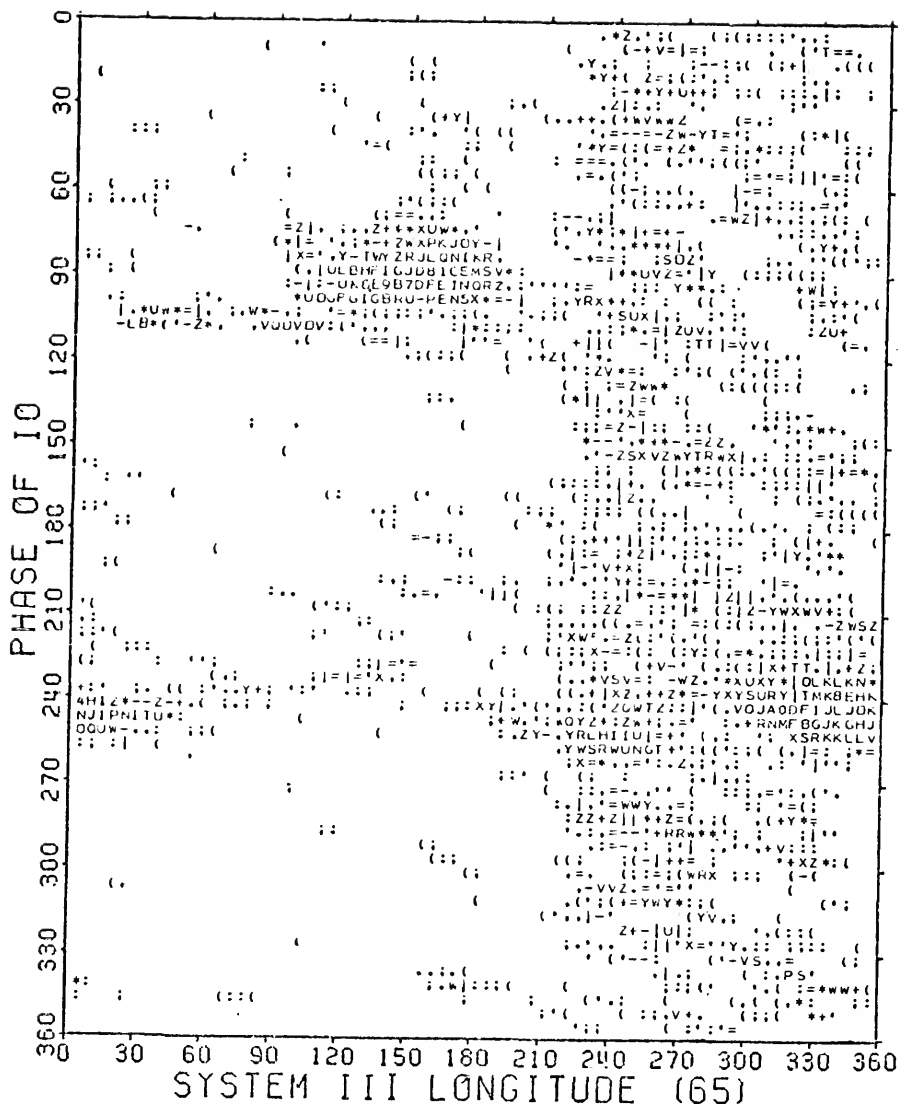


Figure IV-20. Histograms of 16-MHz relative occurrence probability for  $2^\circ$  intervals in, clockwise from upper left, System III longitude (65) and 10 phase in the isolated source B, C, and A regions.

upper left bulge, characteristic of the source at higher frequencies, has all but disappeared in Figure IV-18, and the lower edge of the source extends to an Io phase of  $120^\circ$  as it did at 18 MHz. The Io-related source-B peak in Figure IV-20 is now skewed in the opposite manner from its behavior at frequencies above 18 MHz. Also, the non-Io-related source-B radiation has resumed an intermittent nature similar to that at frequencies above 18 MHz.

The amount of data increases at 15 MHz to an average of 94 minutes and 14 observations per  $5^\circ$  by  $5^\circ$  zone. The average occurrence probability has also risen slightly, to 0.075. Two major differences make Figure IV-21 distinct from Figure IV-18. Between 16 and 15 MHz, source D has become visible between the longitudes of  $15^\circ$  and  $100^\circ$  at an Io phase above  $100^\circ$ . The source has a surprisingly high degree of probability, considering that it was not noticeable at a frequency one MHz higher. There also seems to be an arching bridge of radiation between the edge of source C at  $60^\circ$  longitude and the  $200^\circ$  edge of source A. Figure IV-23 exhibits the same skewing of source B toward higher values of Io phase and the same bifurcation that was present at 16 MHz. Some interesting secondary peaks are present in the non-Io-related part of the Io-phase source-B histogram. The two at  $105^\circ$  and  $240^\circ$  relate to source D and the storms linking sources A and C through the B region. Other secondary peaks in all of the Io-phase histograms may be due to the superposition of storms in the active years, although the peak just preceding source C in Io phase seems to be persistent through many frequencies.

A drastic change occurs between 15 and 10 MHz. Figure IV-24 only vaguely resembles Figure IV-21 because non-Io-related radiation has



52 7<>(((. =|\*+ZYXWVUTSRPONMLKJIHGFDCEBA9876543210

Figure IV-21. Histogram of relative occurrence probability for 5° intervals in System III longitude (65) and the phase of Io, based on all 15-MHz data. The characters represent percentiles of the maximum occurrence probability. Their number and rank from lowest to highest are listed at the bottom. All probabilities below 0.075 have been replaced by blanks.

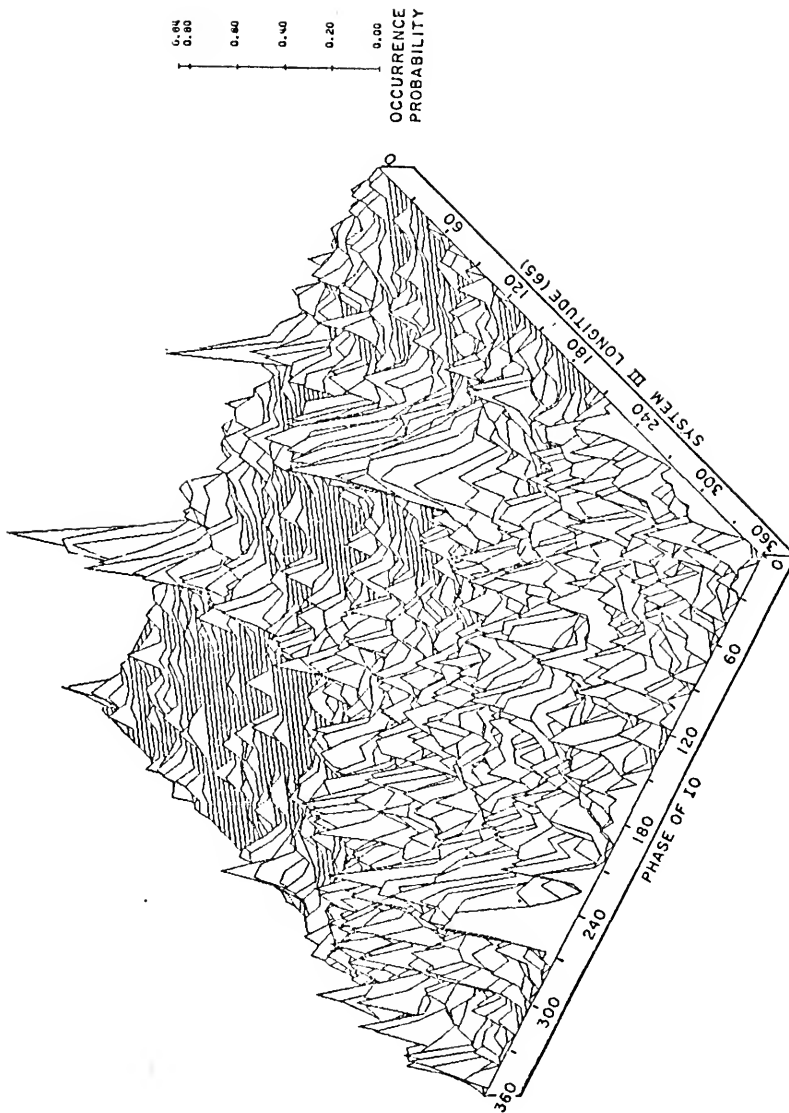


Figure IV-22. Perspective view of 15-MHz occurrence probability for System III longitude vs. the phase of  $I_0$ . Comparison of distance above the base with the scale at right yields the probability.

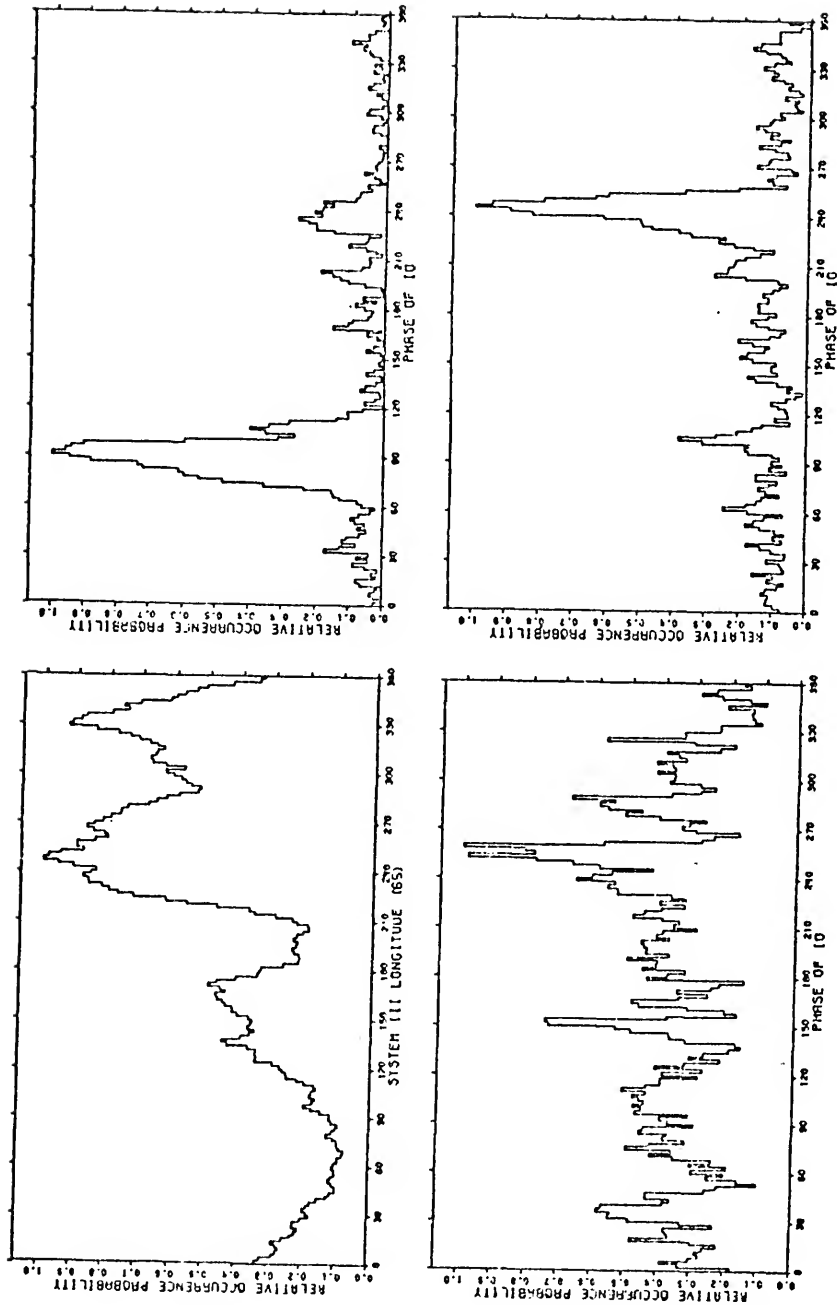


Figure IV-23. Histograms of 15-MHz relative occurrence probability for  $2^\circ$  intervals in, clockwise from upper left, System III longitude (65) and Io phase in the isolated source B, C, and A regions.

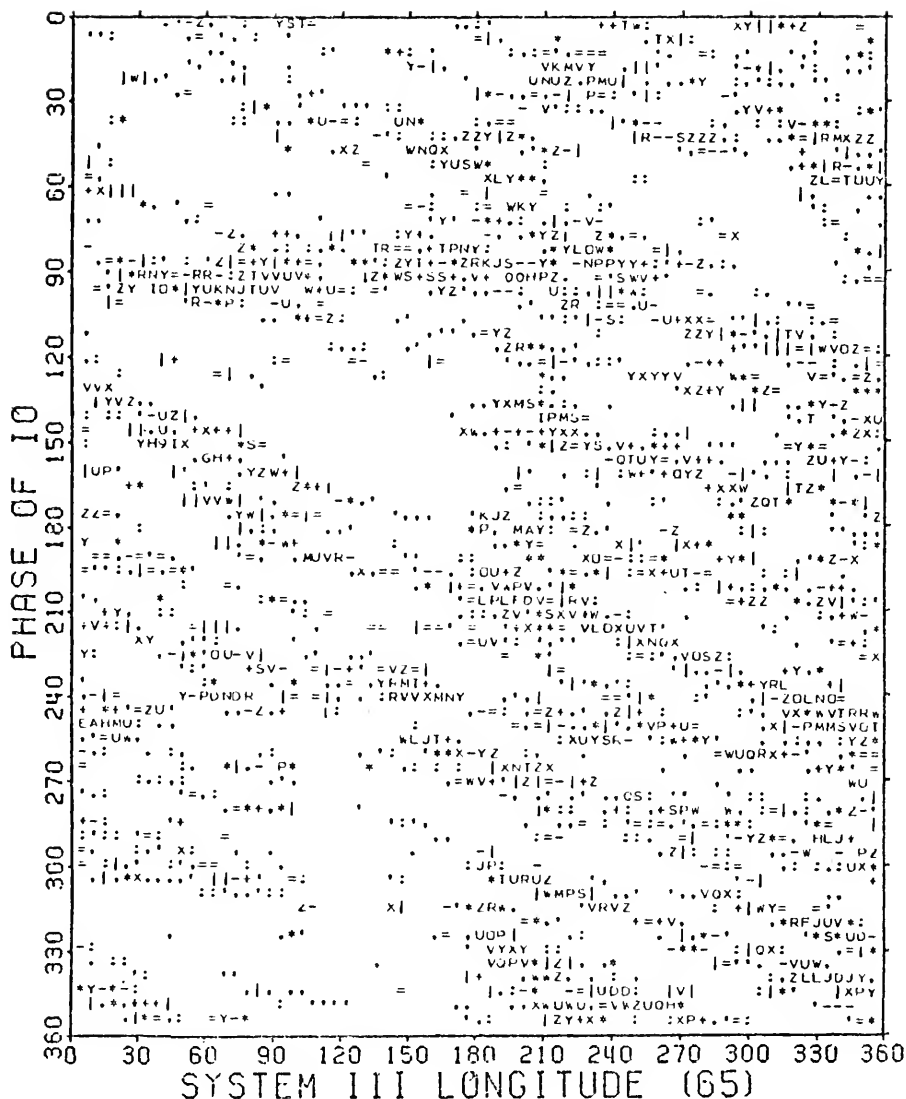


Figure IV-24. Histogram of relative occurrence probability for 5° intervals in System III longitude (65) and the phase of Io, based on all 10-MHz data. The characters represent percentiles of the maximum occurrence probability. Their number and rank from lowest to highest are listed at the bottom. All probabilities below 0.121 have been replaced by blanks.

spread throughout the  $\lambda_{III}-\phi_{Io}$  plane. The  $Io$ -related source regions no longer dominate the picture with higher probabilities, and so it is difficult to pick out any features in Figure IV-25. The most noticeable part of Figure IV-24 is the downward-sloping structure indicative of the fact that this frequency is one of the lesser-observed, with an average of 47 minutes of observation accumulated in 7 sessions for each of the  $5^\circ$  by  $5^\circ$  zones. Even with the elimination of all characters representing values below the average occurrence probability of 0.121, the picture remains cluttered.

The biggest aid in sorting out the features is Figure IV-26. According to the longitude plot in this figure, the probability peaks at  $210^\circ$  and  $350^\circ$ . The radiation near  $210^\circ$  is fairly evenly spread over all values of  $Io$  phase. This is revealed in the one-dimensional, source-A,  $Io$ -phase histogram and in close examination of Figure IV-24. The  $Io$ -related part of source A in Figure IV-24 is no longer detectable above its surroundings.  $Io$ -B is still noticeable, but the dominant part of it occurs at a higher longitude than in the 15-MHz case. Upward projections from the source toward lower  $Io$  phase are no longer distinguishable from the background radiation, if they are even present. It is difficult to separate the  $Io$ -related parts of source B and source D, since B has narrowed in its  $Io$ -phase extent. A gap at approximately  $120^\circ$  longitude seems to separate D from B. If this is true, then source B begins at a higher longitude and has its maximum at higher values than in the upper-frequency diagrams, suggesting that the whole source has moved upward. Also, the null zone of  $Io$ -independent radiation has changed from the  $50^\circ$ - $100^\circ$  longitudes to the  $100^\circ$ - $170^\circ$  band. Further evidence of migration is found in Kennedy's polarization work (1969). The source A

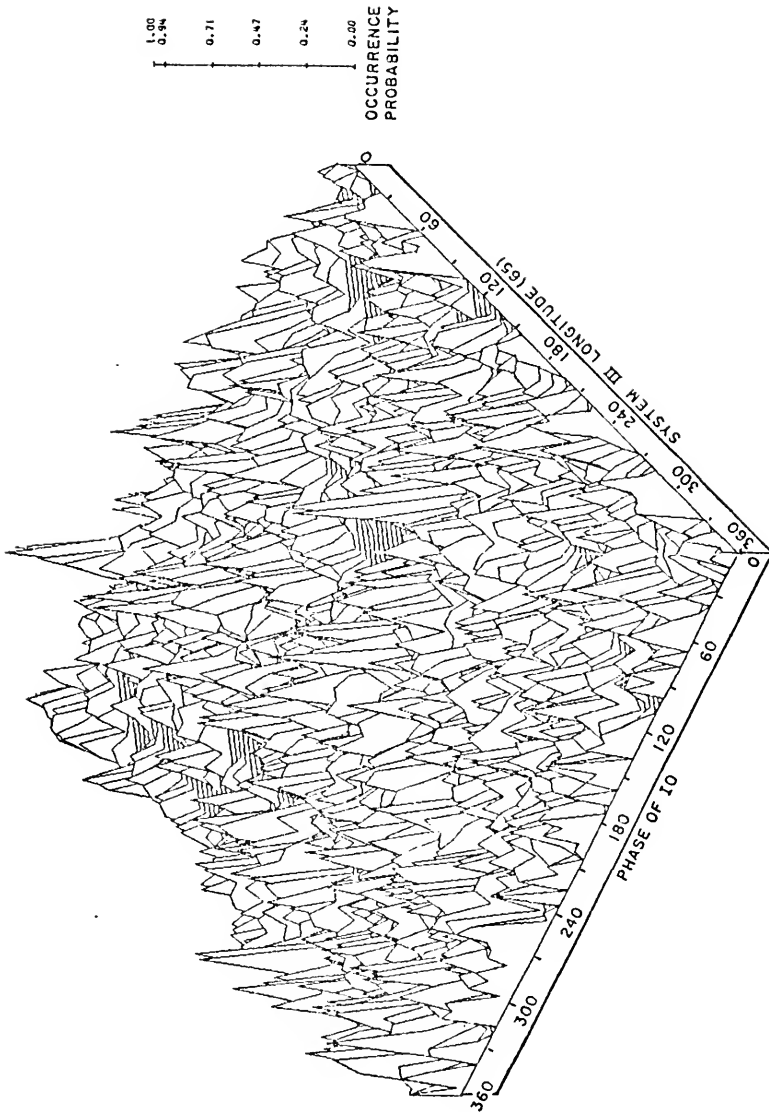


Figure IV-25. Perspective view of 10-MHz occurrence probability for System III longitude vs. the phase of Io. Comparison of distance above the base with the scale at right yields the probability.



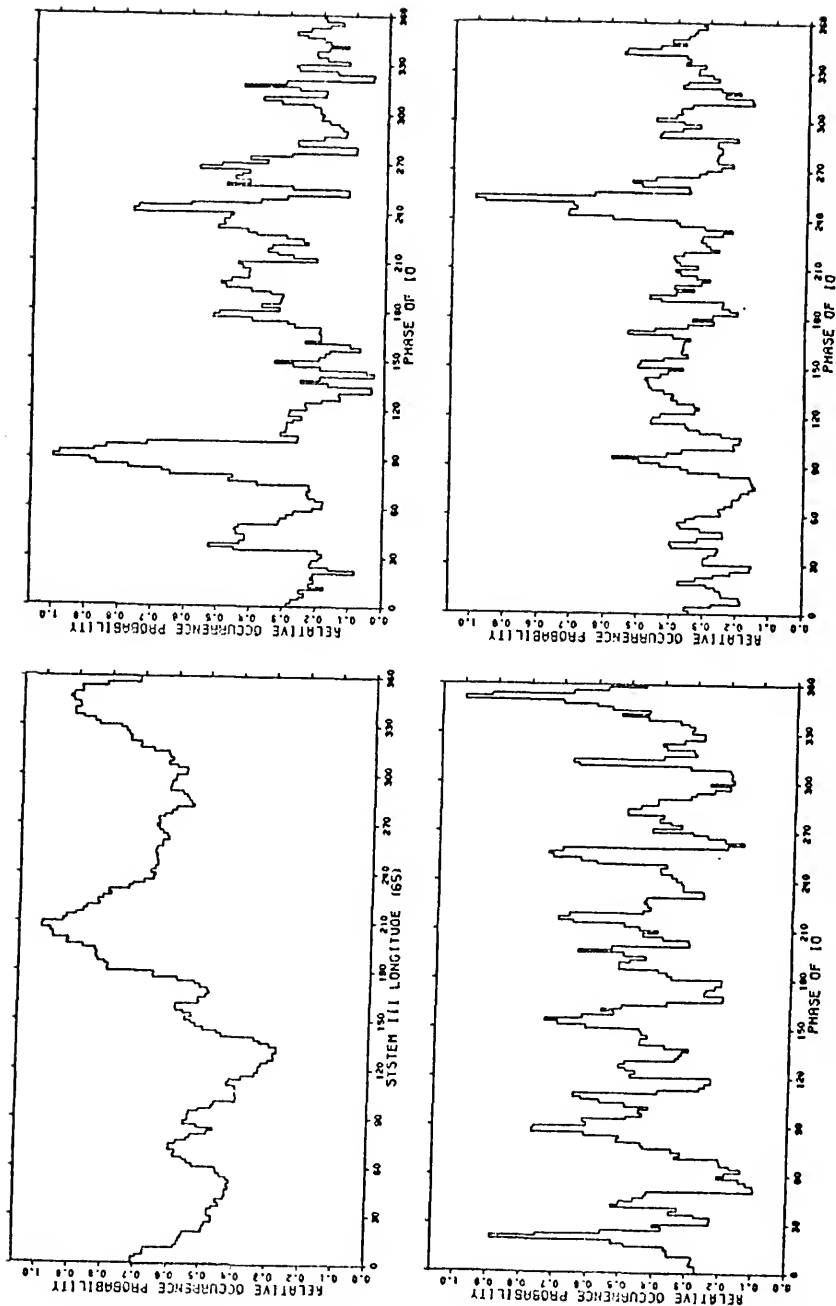


Figure IV-26. Histograms of 10-MHz relative occurrence probability for  $2^\circ$  intervals in, clockwise from upper left, System III longitude (65°) and Io phase in the isolated source B, C, and A regions.

and B regions are known to be polarized in the right-handed sense, whereas sources C and D generally have the opposite sense, though they are more of a mixture. Kennedy finds that the transitions between dominance by one sense to dominance by the other occur at approximately  $100^\circ$  and  $330^\circ$  of longitude in the mid-decametric frequencies. At 10 MHz the upper boundary remains nearly the same, but the lower one has moved to around  $130^\circ$ , indicating a higher-longitude beginning for source B. Careful comparison of Figures IV-24 and IV-21 suggests that between 15 and 10 MHz the non-Io-related source-A storms have split away from their source-C counterparts and moved to lower longitudes. It seems reasonable to say that the longitude probability maxima of sources A and B have moved toward each other and blended together to form the longitude histogram peak at  $210^\circ$  as implied earlier by the lines in Figure III-2.

The longitude peak at  $350^\circ$  in Figure IV-26 is obviously formed from the combination of Io-related and Io-dependent source C. Secondary peaks in the  $60^\circ$ - $100^\circ$  longitude range align with the Io-related source-D radiation located at an Io phase of  $90^\circ$ . Another secondary peak at  $150^\circ$  seems to be caused by the increased number of storms near an Io phase of  $240^\circ$ . These storms are in the same position as the "bridge" at 15 MHz connecting sources C and A. In comparing Figure IV-24 to the 15-MHz equivalent, traces of a bridge can still be seen. Little can be said about the asymmetry of the Io-related sources still present, since the pervasive Io-independent storms obscure the fine details.

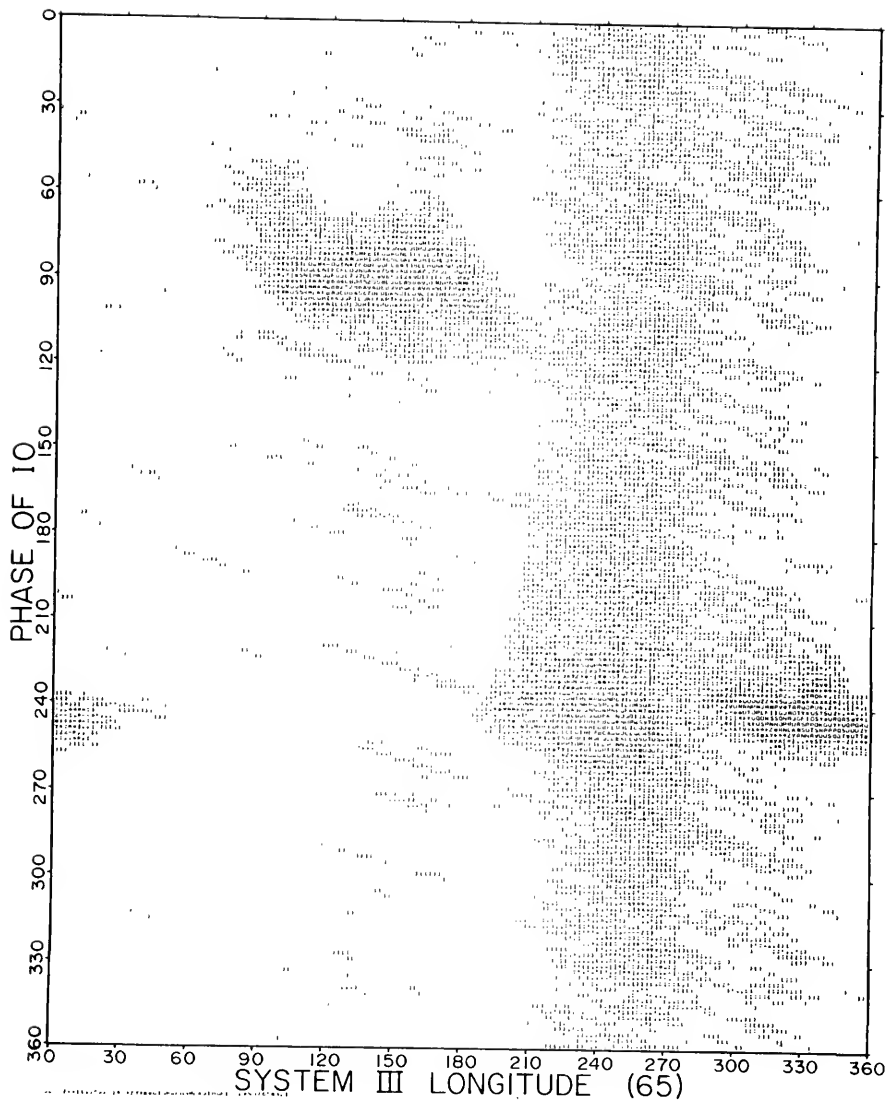
#### 4.3 Io-Related Source Chronology

Subdivision of the two-dimensional histograms into shorter time periods will again require the use of the largest possible set of data. As in the previous chapter, the merged 18, 20, and 22-MHz data will be

used, since they have been extensively observed and their histograms closely resemble each other. Figures IV-27 to IV-29 display the properties of the merged-frequency data for all years. Some individual characteristics of the frequencies are still apparent, such as the radiation on the higher Io-phase side of source B contributed by the 18-MHz data. For Figure IV-27 the  $2^\circ$  by  $2^\circ$  zones now represent an average of 175 minutes of observation and 65 observing periods. All characters symbolizing occurrence probabilities below the average of 0.053 have been replaced by blanks. It will be noticed that the downward-slanting structure indicative of low storm levels is still visible in the low-probability regions. Attempts to separate the data in these areas into different time periods would reduce them to a near-meaningless collection of slanted lines. Effort has been concentrated instead on the high-probability, Io-related parts of the sources. Even for these areas subdivision of the data into single apparitions would display too small a number of storms for the years of low activity. For this reason the apparitions during the times of negative declination of the earth,  $D_E$ , will be grouped together.

The changes in source B through the years can be seen in Figure IV-30. Nearly all of the histograms show some storm-evolution streaks, which are difficult to eliminate completely from short spans of data. The same problem causes artificially high probability concentrations such as the large number of 1's in the 1962-63 diagram. The general structure of the source can still be discerned despite these problems. The process of blanking out all characters below the average occurrence probability for the region has been carried out for each diagram.

Figure IV-27. Histogram of relative occurrence probability for  $2^\circ$  intervals in System III longitude (65) and the phase of  $I_0$ , based on combined 18, 20, and 22-MHz data. The characters represent percentiles of the maximum occurrence probability. Their number and rank from lowest to highest are listed at the bottom. All probabilities below 0.053 have been replaced by blanks.



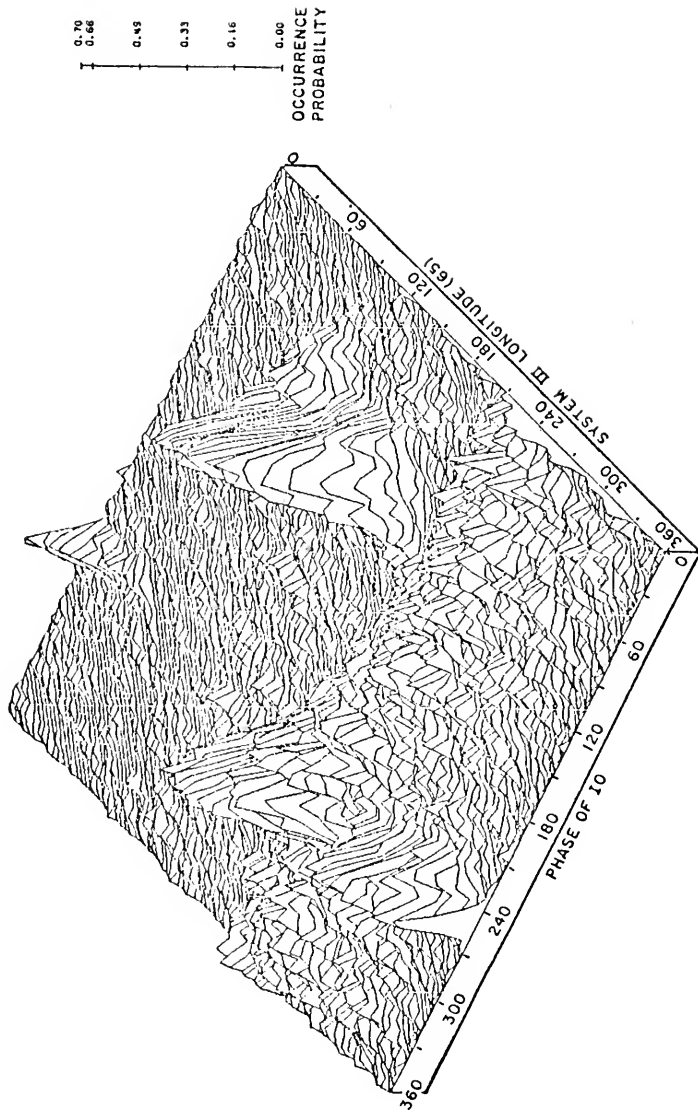


Figure IV-28. Perspective view of combined 18, 20, and 22-MHz occurrence probability for System III longitude vs. the phase of  $I_0$ . Comparison of distance above the base with the scale at right yields the probability.

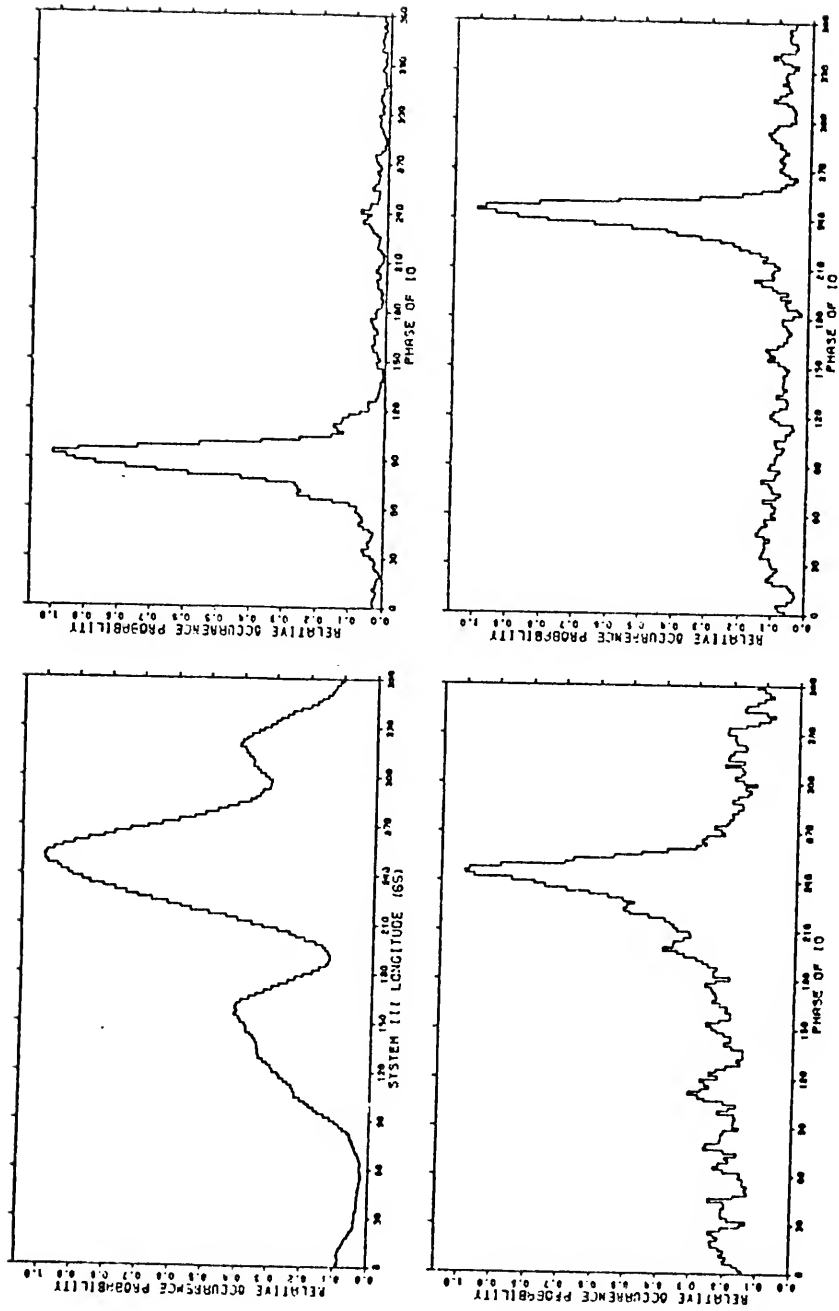
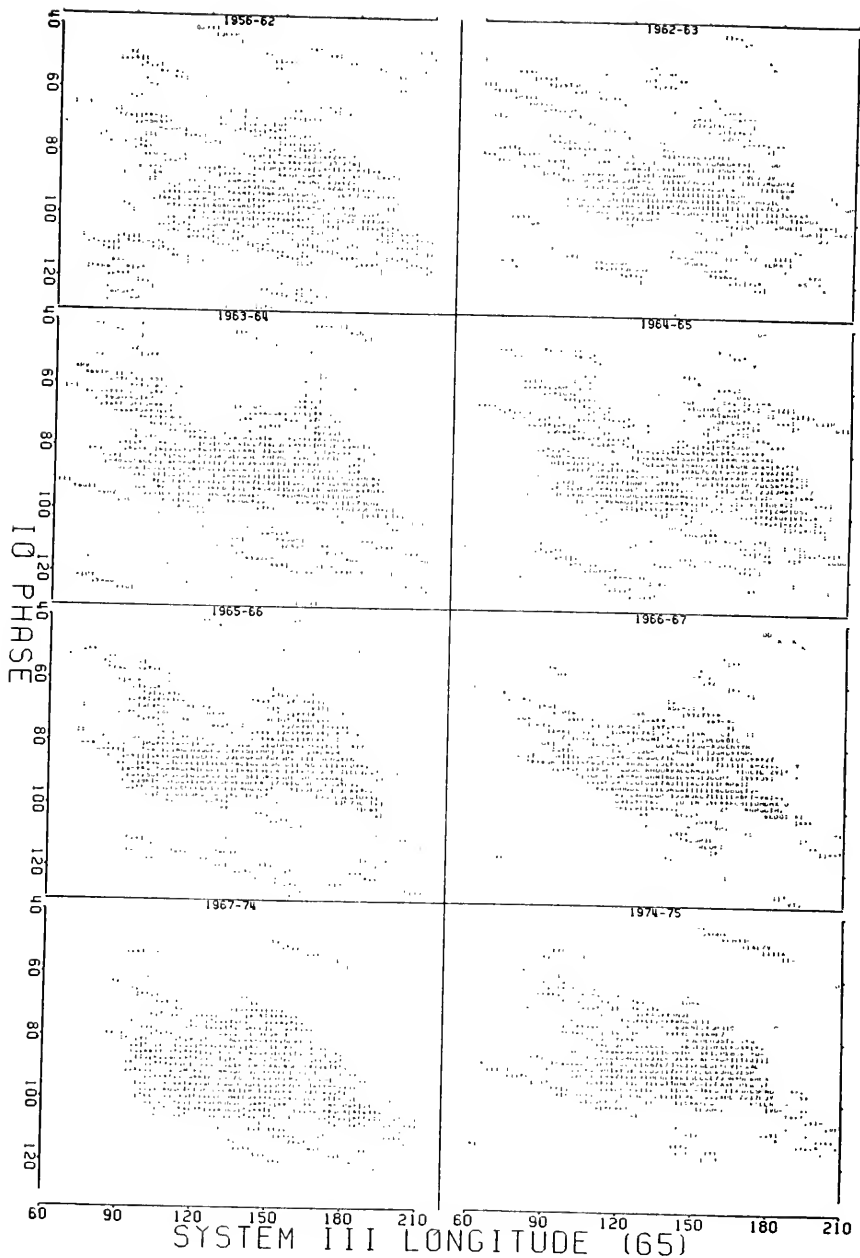


Figure IV-29. Histograms of combined 18, 20, and 22-MHz relative occurrence probability for 2° intervals in, clockwise from upper left, System III longitude (65) and Io phase in the isolated source B, C, and A regions.

Figure IV-30. Comparison of histograms of relative occurrence probability for  $2^\circ$  intervals in System III longitude (65) and the phase of  $I_o$ , centered on the  $I_o$ -related source-B region. Combined 18, 20, and 22-MHz data have been split into individual apparitions for years of positive  $D_E$  and groups of apparitions spanning negative  $D_E$  years. The number and rank of the characters remain the same as in Figure IV-1. All probabilities below the average occurrence probability for each diagram have been replaced by blanks.

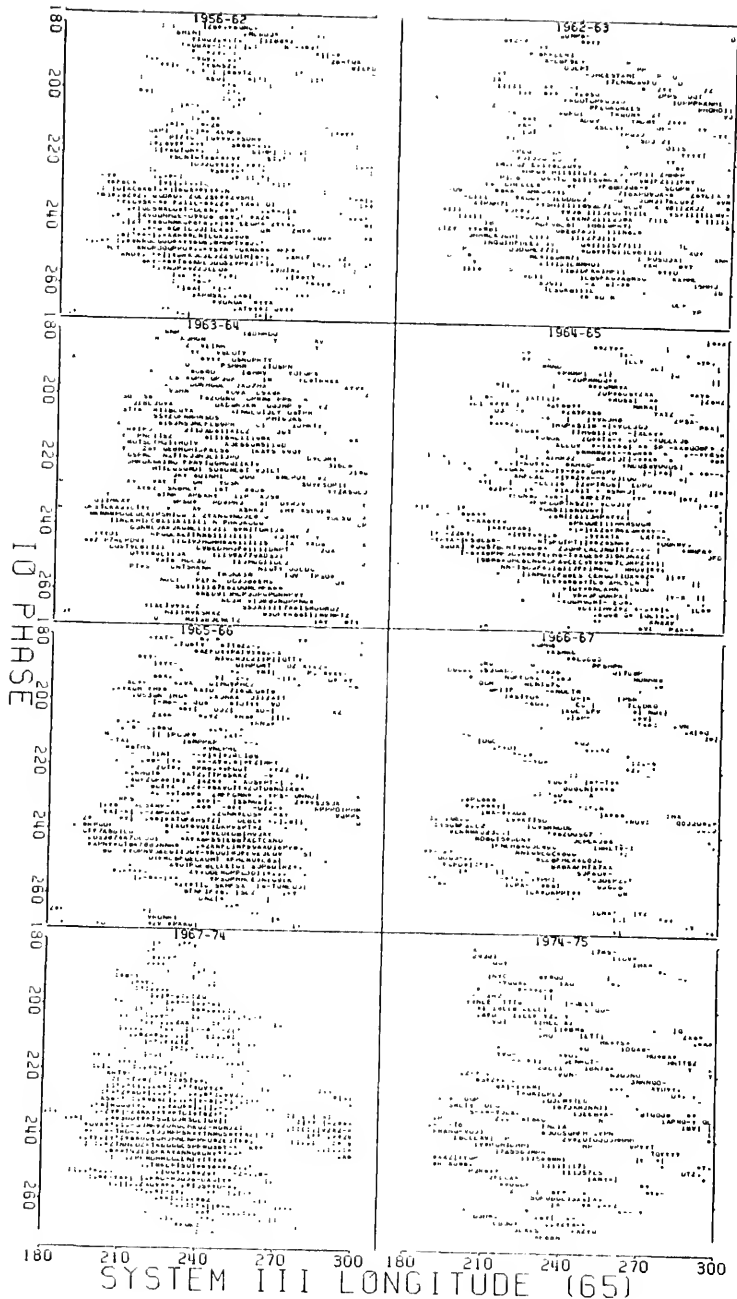




The figure suggests that the motion of source B in Io phase is caused by the entire source shifting its Io phase boundaries with time, rather than having an oscillation of a smaller but heavily-weighted segment within the source. For example, the lower edge (side toward higher Io phase) remains near an Io phase of  $100^\circ$  in the active years, but in the combined negative  $D_E$  years this extends to between  $105^\circ$  and  $110^\circ$ . The more interesting part is the opposite edge. The two upward projections and the intervening blank area vary in appearance over the years. Some of the change can be attributed to the incomplete coverage and low storm levels of this region. Overall examination shows a build-up of the upper structure in the active part of the cycle. At those times the projections extend to around  $55^\circ$  of Io phase on the left and  $60^\circ$ - $65^\circ$  on the right. In the middle, there is generally an indentation to around  $75^\circ$  at a longitude near  $125^\circ$ . The secondary peaks leading the main peak in Io phase, as discussed in the previous chapter, are formed from the combined protuberances, and so they are more probable during the active years. The years of lower probability seem to have a more uniform upper edge with projections absent and the indentation filled. One other characteristic that can be seen in many apparitions may be important. The high-longitude side of the source is usually almost linear in nature, sloping downward at an angle which differs from the slant characteristic of a storm's continuance in time. The implications of all of these phenomena will be discussed further in Chapter V.

The study of source A in Figure IV-31 has a heavily-streaked appearance. Source A is not as probable as source B and it is bracketed by even lower-probability, non-Io-related radiation on the top and bottom. This makes it difficult to acquire enough data in a limited time span to

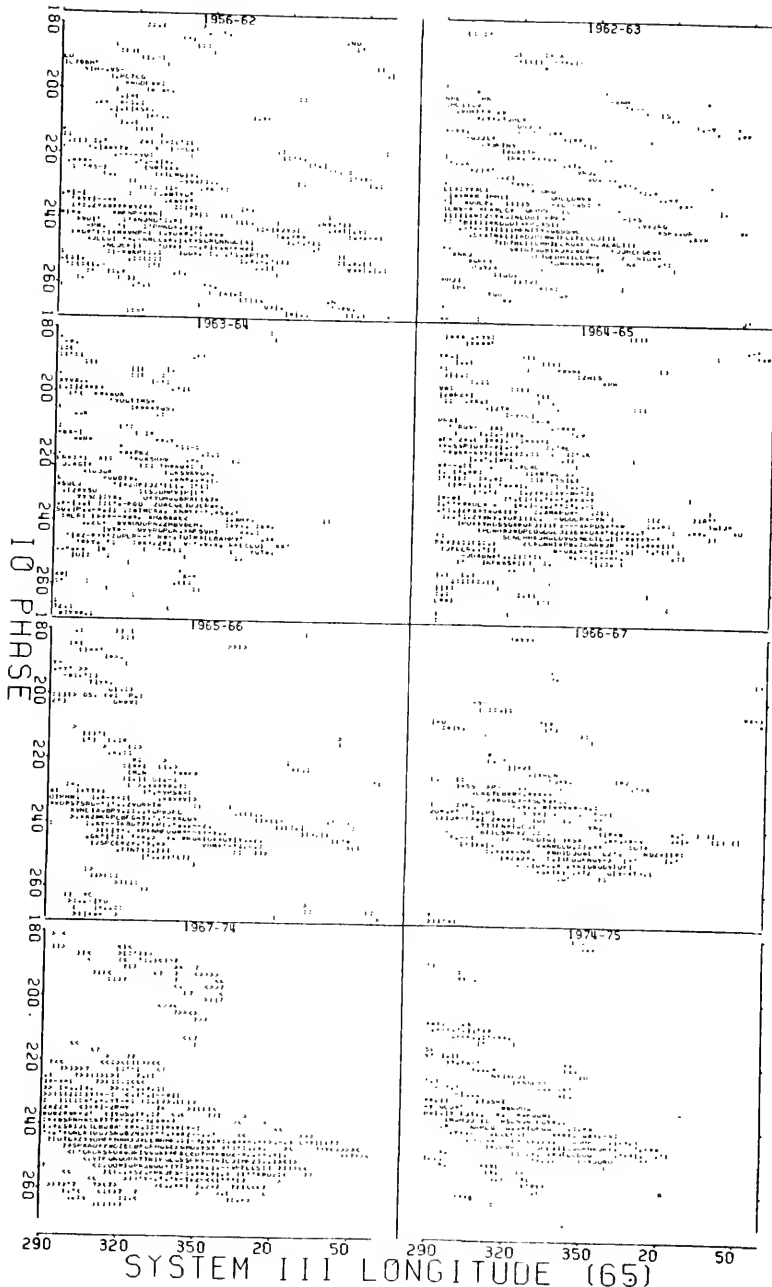
Figure IV-31. Comparison of histograms of relative occurrence probability for  $2^\circ$  intervals in System III longitude (65) and the phase of  $I_o$ , centered on the  $I_o$ -related source-A region. Combined 18, 20, and 22-MHz data have been split into individual apparitions for years of positive  $D_E$  and groups of apparitions spanning negative  $D_E$  years. The number and rank of the characters remain the same as in Figure IV-1. All probabilities below the average occurrence probability for each diagram have been replaced by blanks.



fill in the gaps. The confused scattering of radiation complicates feature recognition. One persistent trait is the rounded bulge extending to the left of the source to a longitude of approximately  $190^\circ$ . This changes slightly in appearance over the years, but not enough to be considered significant. From the diagram it is easy to see that secondary peaks preceding the main peak in the histograms of the previous chapter are caused by the intermittent storm-line ridges. Although the limited time span of a single apparition gives incomplete coverage of the plane and, therefore, a streaked appearance, some of the streaks may be enhanced by passing through a naturally higher-probability area. Thus, the secondary peaks may hint of an underlying feature and be more than just a random superposition. For example, the two histograms combining the negative  $D_E$  years, fairly lengthy time spans, show similar islands of emission preceding the main,  $I_o$ -related part of the source in  $I_o$  phase, although their  $I_o$ -phase boundaries differ. Some other years have storm bands passing through the same area, around  $210^\circ$  of  $I_o$  phase, but 1966-67 is definitely barren at that location. Separation of real from artificial enhancements will require more years of observation and/or additional data from the past filling in the gaps in the times of monitoring.

The lower level of non- $I_o$ -related radiation in the source-C region permits a closer examination of the  $I_o$ -related qualities. First impressions of Figure IV-32 suggest that source C is simply a fairly wide swath of radiation beginning around an  $I_o$  phase of  $240^\circ$  and sloping downward in the normal manner for storm evolution. The end of this swath, however, usually levels out and sometimes bends back upward, as in 1967-74. This often gives the bottom edge a rounded appearance. The overall picture

Figure IV-32. Comparison of histograms of relative occurrence probability for  $2^\circ$  intervals in System III longitude (65) and the phase of  $I_o$ , centered on the  $I_o$ -related source-C region. Combined 18, 20, and 22-MHz data have been split into individual apparitions for years of positive  $D_E$  and groups of apparitions spanning negative  $D_E$  years. The number and rank of the characters remain the same as in Figure IV-1. All probabilities below the average occurrence probability for each diagram have been replaced by blanks.



of source C in Figure IV-27 suggests another feature which can be picked out in careful observation. There is a bulge at the upper edge of the source at a longitude of about  $340^\circ$  and an  $I_o$  phase near  $230^\circ$ . This enhanced area is especially noticeable in the active years from 1963-66. Part of the responsibility for the motion of the source in  $I_o$  phase can be attributed to the appearance of this projection. Also, as in source B, source C's lower edge extends to higher values of  $I_o$  phase in the years of negative  $D_E$ . The secondary peaks in the one-dimensional histograms around  $200^\circ$  to  $210^\circ$  of  $I_o$  phase are seen to be bands of storms differing little from the other non- $I_o$ -related radiation in C's longitude range. Again, whether the secondary peaks suggest significant phenomena or merely result from the limited observational cycle is hard to distinguish.

If the radio emission from Jupiter is dependent upon the variables  $\lambda_{III}$ ,  $\phi_{I_o}$ , and  $D_E$  only, then apparitions which are twelve years apart should appear similar, since they have nearly equal values of  $D_E$ . Sufficient coverage of the  $\lambda_{III}$ - $\phi_{I_o}$  plane during each apparition is assumed. In Figures IV-30 to IV-32 this corresponds to a statement that the top and bottom rows of histograms should match. In each of the pairs some vague resemblances can be picked out and have been mentioned as peculiar to the low-activity years which they represent. Overall they are far from exact copies. The large differences in the amount of data and in the observational technique before and after a 12-year interlude probably explain the modification, but there is still a possibility that another variable may be needed to account for all discrepancies. The active part of the cycle, presently taking place, should make it possible to compare single apparitions having relatively high storm levels in the near future.



Many first- and second-order effects have been revealed in this and the previous chapter, with little supposition regarding their relationship to the decametric emission process. This speculation has been saved until now so that the basic theories and the implications of the effects on these theories might be presented as a unit. The next chapter is dedicated to this task.

## CHAPTER V

### THEORETICAL IMPLICATIONS

#### 5.1 Introduction

The toil of a multitude of observers scanning Jupiter over a score of years can be matched only by the man-hours expended in explanation. A pile of pertinent theoretical publications, excluding superficial opinions proffered in the midst of experimental outcome, is daunting in stature. Comprehensive review of said articles would be unduly long and unnecessary. Fortunately, the field has been blessed by periodic resumes of exceptional value (Warwick, 1964, 1967, 1970; Ellis, 1965; Carr and Gulkis, 1969; Smith, 1976). On page 1147 of the latest of these is a declaration which summarizes the inherent worth of the accumulation of analyses: ". . . we believe that in the paradigmatic nature of science a successful theory will emerge from the gradual modification and consolidation of previous work, rather than from radically new hypotheses." Assuming that a completely independent solution has not occurred and is nor forthcoming, it would seem well to concentrate on comparing results with the newer theories, which have profited from critiques of prior postulates and have been honed by the expanding assemblage of evidence. Indeed, the latest offerings are more given to numerical statements of expectations, permitting direct testing of their validity, especially in light of the post-Pioneer parameter boundaries.

In the course of Smith's review, the theories are divided according to their treatment of the coupling mechanism which must provide a

trigger for Io to stimulate radiation; the instability mechanism and corresponding amplification process required to explain the power for both Io-related and Io-independent radiation; and the subsequent propagation of the radio waves through the Jovian plasmasphere. Emphasis in this dissertation has been on the morphology of the sources, which is most directly affected by the last category, although the previous sections certainly have some influence. Propagation theory is the least discussed aspect of decametric radiation, making direct comparison of prediction with observation applicable to only a few theoretical models. Some of the second-order effects uncovered in the previous chapters relate in an indirect fashion to other theories, and this too will be considered wherever possible. Let us examine the results in the context of several hypotheses.

## 5.2 The Source B Anomaly

Evident throughout Chapter IV is the consistency and longevity of the Io-related source-B shape. Its uniformly high degree of probability and control by Io make it a natural starting point for studying the nature of Io's influence. Figure V-1 summarizes all of the activity in the Io-B region for the frequencies 18, 20, and 22 MHz. In the histogram the zones are  $2^\circ$  by  $2^\circ$ , the character sequence is the same as for similar plots in Chapter IV, and all symbols representing probabilities below 0.114 have been replaced by blanks. In a way, the shape resembles a profile view of a cellophane tape dispenser. The two upper projections responsible for this morphology are the interesting part. The line drawn through the diagram illustrates one of the family of lines of equal slope which trace the change of longitude and Io phase with time. The positioning of

Figure V-1.

Histogram of relative occurrence probability for  $2^\circ$  intervals in System III longitude (65) and the phase of  $I_0$  for all 18, 20, and 22-MHz data in the  $I_0$ -related source-B region. The characters represent percentiles of the maximum occurrence probability. Their number and rank remain the same as in similar diagrams for Chapter IV. Significance of the slanted line, circles, and numbered points is explained in the text. The longitude ranges in which the proposed subdivisions of source B,  $B_1$  and  $B_2$ , dominate are indicated.



this particular line shows that both bulges can be sampled in a single night of monitoring. Examination of the histogram occurrence probabilities along or near this line reveals a probability of 0.13 at point 1 on the line, a zero probability at point 2, and a 0.32 value at the third position. These probabilities seem insignificant when compared with the maxima nearby (see the perspective plots of Chapter IV), but there is still a definite modulation effect. The mechanism producing the anomaly seems to allow storms to occur, then shuts them off completely, to be followed by an even more probable occurrence of storms--all within the space of an hour and a half.

Does the radiation actually follow this scenario, or are pre- and post-null probabilities built up from separate storms on different nights? Even in the merged-frequency data presented in the figure, there are few nights in which the plotted track of the period of monitoring would lie close to the depicted line and span both enhancements during a time of reasonably radio-quiet conditions. In a study of many apparitions of data, 25 nights were found to have storms contributing to zones along or near the line in question. Of these, 7 of the cases exhibited activity both preceding and following the null zone at point 2. Thus, in some instances the radiation does turn on and off, and then on again from the earth's viewpoint. On none of the nights was this behavior observed at more than one frequency. This could reflect the difficulty of receiving the low-probability events, or it could mean they are narrow-band by nature. It would be interesting to examine the traces of these events as recorded by the spectrograph at Boulder, Colorado. Unfortunately, according to the catalog of Warwick *et al.* (1975) only two of the incidents were received in Boulder. Nevertheless, the study of the

Boulder data from all appropriate nights would be beneficial. One other comment, which will be discussed in more detail later, is that all but one of the sets of pre- and post-null storms occurred in the first half of an apparition.

The two bulges of source B are mentioned in the literature indirectly. The upper left protuberance and the radiation in the main part of the source directly below and to the right of it often combine to form a secondary peak at approximately  $125^\circ$  longitude in one-dimensional histograms (cf. Figures III-1 and III-7) or two-dimensional contour plots of source B. This has prompted some researchers (Smith, et al., 1962; Goertz, 1971) to consider the two peaks as separate sources, labeled  $B_1$  and  $B_2$ , which overlap in their longitudinal widths making them appear as one source. The approximate longitudinal range of each source is indicated in Figure V-1. Goertz reverses the order of labeling, but in this work  $B_1$  will refer to the dominant peak in the longitude histograms. Several arguments can be made for and against the division of source B.

Close scrutiny of Figure V-1 reveals two nearly equal maxima which have been circled. The first is symbolized by a "0" at  $127^\circ$  in longitude and  $93^\circ$  in Io phase, and a "1" represents the other at  $151^\circ$  in longitude and  $89^\circ$  in Io phase. The dual maxima were also apparent in some of the contour plots mentioned previously, but the difference in Io phase between the two peaks was not as obvious. In general, the surrounding zones emphasize the change of Io phase resulting in a slight upward slant of the probability contours across the main body of the source. This, in turn, causes a slight indentation along the bottom edge at longitudes near  $B_1$ . If  $B_1$  and  $B_2$  are separate sources they seem to vary slightly

in Io-phase position. It is interesting that  $B_2$ , the secondary peak in the one-dimensional longitude histograms, has an Io-phase position equal to the one-dimensional Io-phase maximum.

Division of source B has also been indicated by the spectral changes in the  $B_1$  and  $B_2$  bulges, if they may be so labeled, brought out in the previous chapter. The  $B_2$  extension is prominent at 30 and 27 MHz,  $B_1$  dominates at 15 and 16 MHz, and both are conspicuous for frequencies in between. On the other hand, the one-dimensional longitude histograms of the entire source remain nearly unchanged by frequency differences.

The previous chapter has also discussed the occurrence of non-Io-B radiation, especially at the lower frequencies, and its usual confinement to longitudes between  $120^\circ$  and  $180^\circ$ . This means the non-Io-related storms are centered on the  $B_1$  longitude range of the source. Few storms are found in, or extend to, the lower  $B_2$  longitudes. One exception to this appears in the work by Desch and Carr (1974) at 26 MHz, in which the non-Io-B band seems to be centered on a lower longitude between the  $B_1$  and  $B_2$  peaks. It is possible that the sensitivity of their antenna array has allowed detection of low-intensity non-Io- $B_2$  radiation. In combination with Io-independent- $B_1$  storms this would explain the decrease in the central longitude.

At this point it will be beneficial to consider the theory of Cavaliere and Speranza (1971), which assumes the existence of non-Io-B radiation. For explanation of Io-related sources the theory espouses a now-common interpretation of the Io influence first proposed by Dulk (1965), in which the Io-related sources originate near the point where the magnetic field lines passing through or near Io intersect the Jovian cloud tops (the "foot" of Io's flux tube), and the radiation is emitted nearly



perpendicular to these lines. The longitude beneath Io at the time of storm onset and the direction to the earth determine which of the sources, if any, are seen. This is shown in Figure V-2, a modification of a diagram in the article by Cavaliere and Speranza. The figure looks down on the north pole of the axis of rotation and Io is placed at two positions of interest. At the foot of the Io flux tube, the curved line connecting Io to Jupiter, the direction of emission of Io-related radiation is represented by arrows nearly orthogonal to the flux lines. If the emissions reach the earth, their identification as a particular Io-related source depends on the position of Io and the longitude facing the earth at the time of storm generation. The two examples of Io position were chosen for their angular distances from the north magnetic pole (NMP), assumed to point toward a longitude of  $200^\circ$  as represented by the dashed line. They yield the Io-related sources indicated at the tips of the arrows at the flux tube feet. Thus, Io-A and Io-B<sub>2</sub> storms may have the same point of origin, but they are distinguished by their direction of propagation. For small changes in the given positions of Io, the identification of the sources will remain the same. Larger changes will bring a cutoff of the source by some type of modulation mechanism.

According to Cavaliere and Speranza, the non-Io sources are turbulent plasma regions beaming radiation radially outward from the planet. The theory's modulation mechanism permits occurrence of Io-related storms only when Io is over a longitude corresponding to the non-Io-A and non-Io-B sources. The non-Io-A and non-Io-B sources surround the magnetic pole as depicted by the shaded regions and labeled arrows in Figure V-2. The Io-related storms are, therefore, stronger emissions generated in the same turbulent plasma regions which produce non-Io radiation. The major

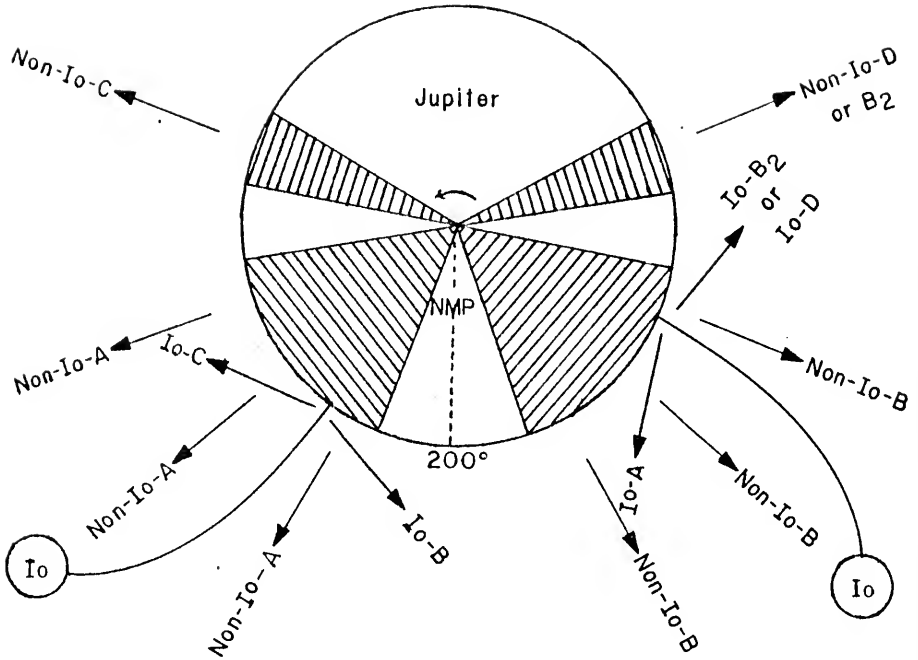
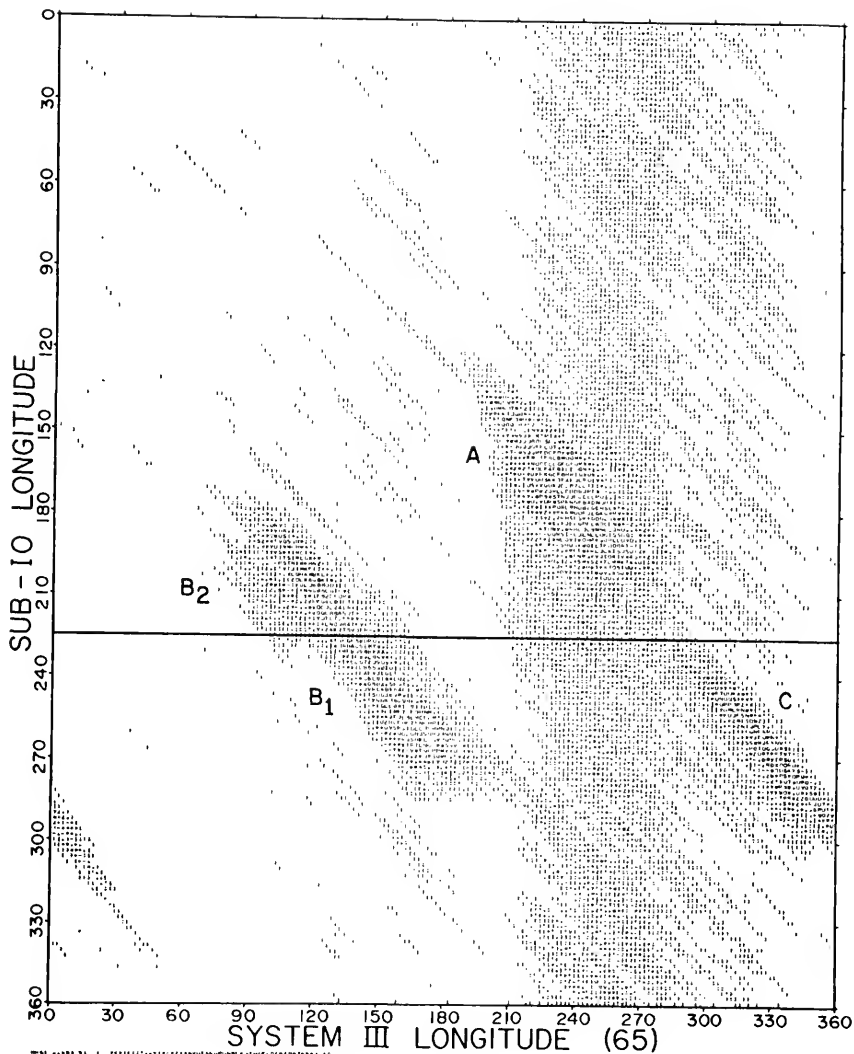


Figure V-2. View of Jupiter from directly over the north pole showing sample beaming directions of the decametric sources according to an extension of the theory of Cavaliere and Speranza (1971). The longitude of the north magnetic pole (NMP) is assumed to be  $\sim 200^\circ$ . The geometry of source emission for the Io-related sources applies to many other theories as well.

drawback to this hypothesis is the failure to account for non-Io-C radiation. Extension of the theory may explain this source and imply existence of non-Io-B<sub>2</sub>. Cavaliere and Speranza state that the Io-dependent A and B sources are positioned symmetrically about the longitude of the north magnetic pole ( $\sim 200^\circ \pm 50^\circ$ ). An extension of the theory to include a separate non-Io-C source at a longitude centered around  $310^\circ$  would suggest by symmetry a counterpart near  $90^\circ$ . This latter source could be interpreted as non-Io-B<sub>2</sub> or perhaps non-Io-D, if they exist. Some evidence for a band of Io-independent storms centered on the  $90^\circ$  longitude can be found in Figure IV-24, the two-dimensional histogram for 10-MHz data. The problem with the extension of the theory is that one would expect Io-related radiation to occur in the non-Io-C and non-Io-B<sub>2</sub> regions. The angular distance of these sources from the north magnetic pole may weaken the plasma turbulence and prevent this emission. In general, the modulation mechanism proposed by Cavaliere and Speranza works well for explanation of approximate source positions, but the added assumptions necessary to explain non-Io-C radiation and the exact source boundaries would stretch its credibility.

In Figure V-2 the perpendicular-beaming model suggests that Io-related sources B<sub>2</sub> and A originate on the opposite side of the north magnetic pole from sources B<sub>1</sub> and C. The reason for this is clearer in the next figure. Figure V-3 replots the 22-MHz data of Figure IV-9 in terms of System III longitude versus the longitude beneath Io at the time of emission. The sources are altered in shape, but still recognizable, and they are more closely grouped. A line drawn along a sub-Io longitude near  $225^\circ$  separates not only sources A and C, but also B<sub>1</sub> and B<sub>2</sub>. For purposes of radiation-beaming symmetry most theories incorporate some mechanism which places the

Figure V-3. Histogram of relative occurrence probability for 2° intervals in System III longitude (65) and the sub-10 System III longitude (65) for all 22-MHz data. The characters represent percentiles of the maximum occurrence probability. Their number and rank are listed at the bottom.



WOL 4482 71 1 PERIODICITY OF POINTS IN THE SYSTEM III LONGITUDE

origin of Io-related storms at a longitude approximately  $15^\circ$  lower than Io's position. This is equivalent to moving the sources upward by  $15^\circ$  in Figure V-3, and it changes the separation line to  $210^\circ$ , a longitude which is close to that of the north magnetic pole.

The symmetry about the dividing line can be taken one step further by a comparison of Figure V-4, an enlarged view of the Io-related source-C region with the  $B_1$  side of source B in Figure V-1. An overlay of the two, with a longitude of  $185^\circ$  and an Io phase of  $90^\circ$  in the source-B picture aligned with  $360^\circ$  and  $240^\circ$ , respectively, in the source-C diagram, reveals many similarities. The  $B_1$  bulge and the protuberance above source C coincide, as does the downward slant of the edges just to the right of the bulges. Ignoring the scattered non-Io-C data, the extent of each source in Io phase is comparable. The sole difference of major import is the "tail" on the right side of C. Source B sometimes has tails extending into the non-Io-A longitudes, but they never have an upward turn like that of source C.

In the comparison of source  $B_1$  with source C, one is reminded of the Io-phase sinusoidal drifts of sources B and C discussed in Chapter III. Source B varies its Io-phase peak in the same direction, but less than half as much as source C. Perhaps this is caused by a large motion of  $B_1$  like that of source C, coupled with a lack of motion of  $B_2$  like that of A. Alignment of the changing source positions by correcting the data for the sinusoidal drifts should reveal such a situation by a concentration of the maximum probability areas at a single point. In accordance with the results presented in Chapter III, all 18, 20, and 22-MHz storms were modified in observed Io-phase by subtracting  $2.9 \times D_E$  degrees.  $D_E$  was determined from the date of the storm, and the factor 2.9 is

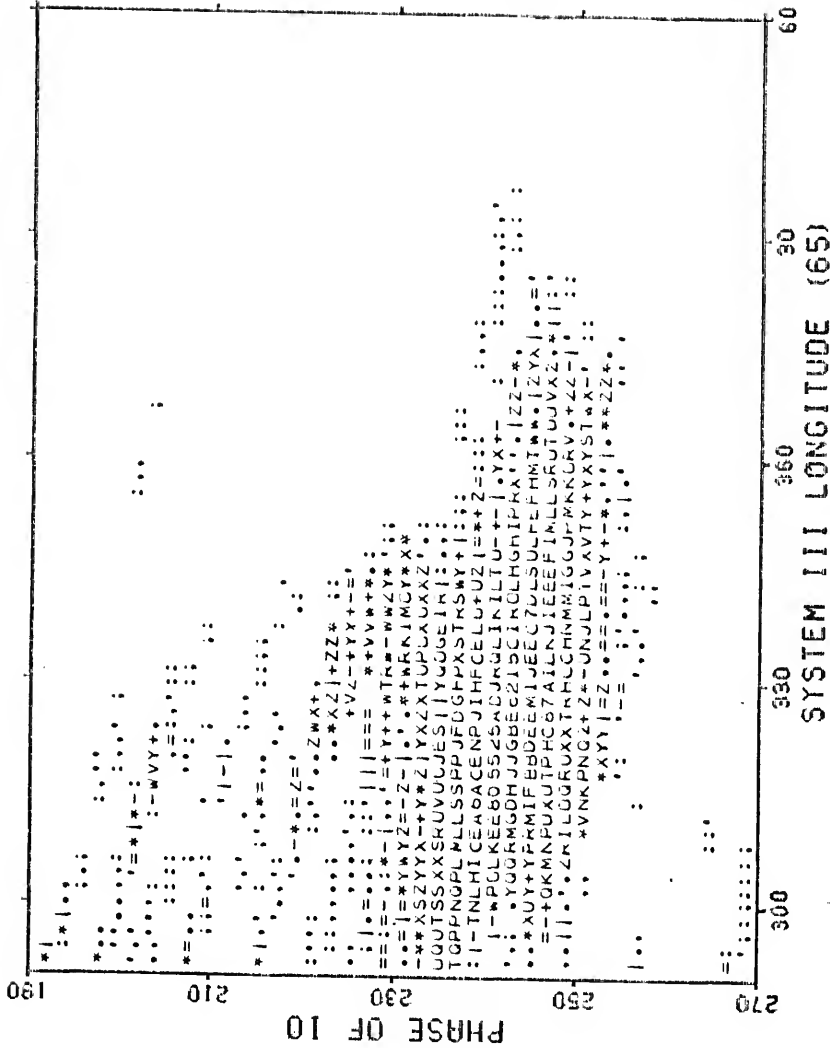


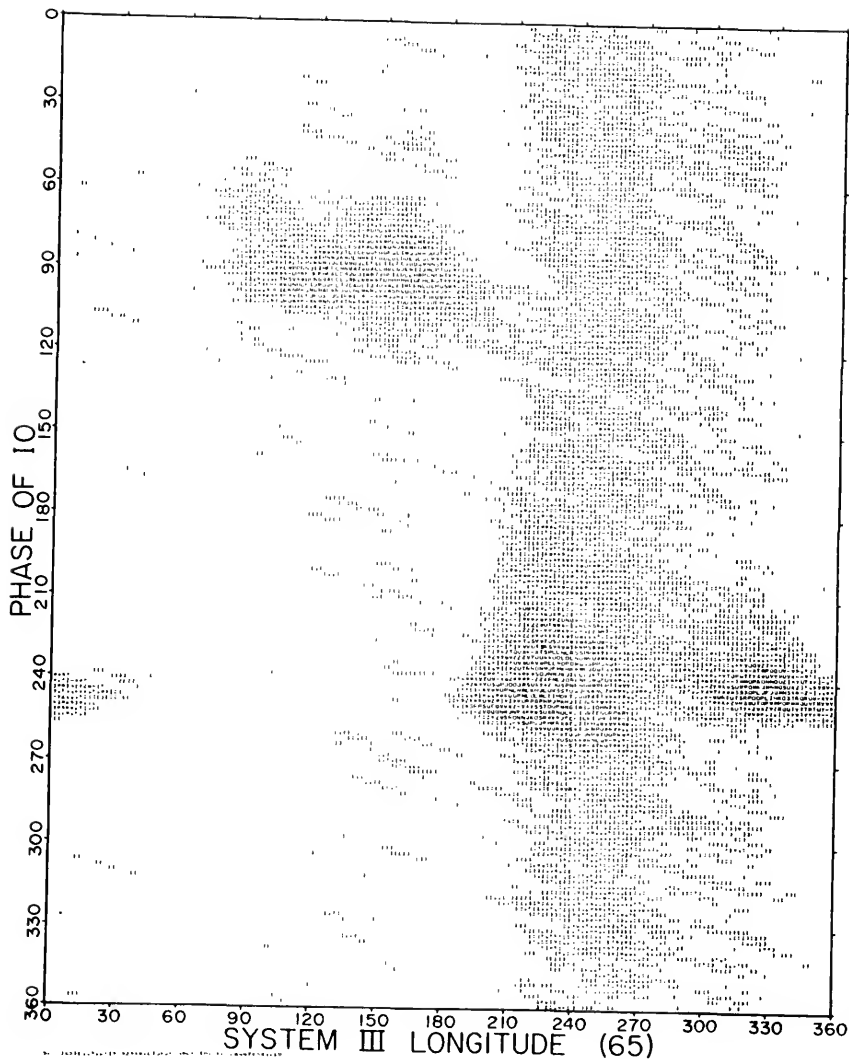
Figure V-4. Histogram of relative occurrence probability for 2° intervals in System III longitude (65) and the phase of Io for all 18, 20, and 22-MHz data in the Io-related source-C region. The characters represent percentiles of the maximum occurrence probability. Their number and rank remain the same as in similar diagrams for Chapter IV.

the proportionality constant determined in Chapter III relating  $D_E$  to Io phase for source C. At the same time, to study the longitudinal motion exhibited by source A, the longitudes of all storms were corrected by  $-2.7 \times D_E$  degrees, a factor ascertained in Chapter III from the non-Io-A drift. The results are shown in Figure V-5 and can be compared with Figure IV-27. Changes between the two figures are nearly insignificant. The non-Io-related radiation seems to be more concentrated within each source's longitude range, implying that each source does have its own Io-independent segment and that all non-Io sources drift in longitude in a similar manner. If the drifts are all similar, they can be explained by a variable period, but this is difficult to reconcile with  $D_E$  dependence. Explanation in terms of beaming geometry seems more likely, but similar changes in the geometry for all non-Io sources are hard to justify. Although the Io-related source-C radiation is more concentrated, the  $B_1$  counterpart is not. This suggests source B moves as a unit in its Io-phase drift, whether or not it is composed of separate sources.

One theory proposes the existence of separate  $B_1$  and  $B_2$  sources. Goertz (1973) hypothesized the triggering of Io-dependent storms by magnetohydrodynamic (MHD) waves traveling down magnetic flux lines which have been perturbed by Io's passage. The waves encounter dense plasma in the lower parts of the Jovian ionosphere and stimulate coherent cyclotron radiation. The radiation is beamed nearly perpendicular to the flux tube so that the propagation geometry for Io-related sources is equivalent to the configuration shown in Figure V-2. In this case, the modulation mechanism limiting the extent of the sources involves the amount of amplification of the radiation. The amplification factor first increases and then decreases rapidly as Io moves away from the longitude



Figure V-5. Histogram of relative occurrence probability for  $2^\circ$  intervals in System III longitude (65) and Io phase for all 18, 20, and 22-MHz data. The storms have been corrected for longitudinal and Io-phase drifts according to the method described in the text. The characters represent percentiles of the maximum occurrence probability. Their number and rank are listed at the bottom.



of the north magnetic pole, since plasma characteristics change with angular distance from the pole. The radiation is lessened when  $I_0$  is over the pole because amplification depends inversely upon the area of spread of the MHD wave and this is greatest at the pole. The result of these conditions is a maximum of amplification on each side of the pole, and the  $I_0$ -related sources are again beamed as in Figure V-2. The theory may also explain the longitudinal merging of sources A and B at 10 MHz observed in earlier chapters, since this radiation should be emitted farther from the planet where amplification may be limited to points closer to the pole. Goertz predicts source positions in a contour plot of reception probability for  $\lambda_{III}$  versus  $\phi_{I_0}$ . Peaks of probability occur near the normal positions for sources A, C,  $B_1$  and  $B_2$  and Goertz labels them as such.

The same pair of amplification maxima produce sources  $B_1$  and  $B_2$  when the phase of  $I_0$  is  $90^\circ$ , and sources A and C for a  $240^\circ$   $I_0$  phase, and yet sources A and C have greater separation in longitude than  $B_1$  and  $B_2$ . The theory accounts for this by stating that sources A and C are produced when  $I_0$  is on the hotter, afternoon side of Jupiter. Heating of the ionosphere makes it thicker, and this in turn causes the amplification factor to peak farther from the pole. A simple test can be used to study this hypothesis.

Assume that the separation of the amplification maxima increases linearly as the Jovian day proceeds. The approximate angular distance in longitude between sources A and C has been measured from the different apparitions of the 18, 20, and 22-MHz data, and it averages around  $70^\circ$ . Measurement of the average  $B_1$ - $B_2$  separation is more difficult, but it is roughly  $30^\circ$ . This means there is a  $40^\circ$  increase in separation over the

150° change in Io's position from the dawn side to near dusk. Although Io-related sources A and C are received on earth when Io is near 240° from superior geocentric conjunction, Io's position from superior heliocentric conjunction at those times changes with the sun-Jupiter-earth angle. Let the change in this angle from one point on the earth's orbit to another be represented by the angle  $\beta$ . For example, the maximum change occurs between the two points of quadrature on the earth's orbit, giving a 23° value of  $\beta$ , as illustrated by Figure V-6.

If the earth's orbit is divided into the first and second halves of a Jovian apparition, then the average change in the sun-Jupiter-earth angle between the positions of earth during the first half and the locations in the second half is 15°. This means that for a given geocentric position Io is an average of 15° farther from superior heliocentric conjunction in the first half of an apparition than in the second half. If the linear-increase-in-separation theory were strictly true, sources A and C should be approximately 4° farther apart in the histogram from the first half of an apparition than in that from the second half. In studying the 18, 20, and 22-MHz source centroids computed before and after opposition, the average difference was 1.8°. This result is inconclusive since the large number of subtractions involved in the computation causes an error of the same magnitude as the result. The smaller-than-expected difference is more realistic in the sense that the temperature of the ionosphere will not continually increase, but will start to decline at some time in the Jovian afternoon. Also, conditions are more favorable for radio reception near opposition and this will effectively decrease the average value of  $\beta$ .

As a side note, in the course of the study outlined above it was found that the average occurrence probability decreased from a value of 0.055

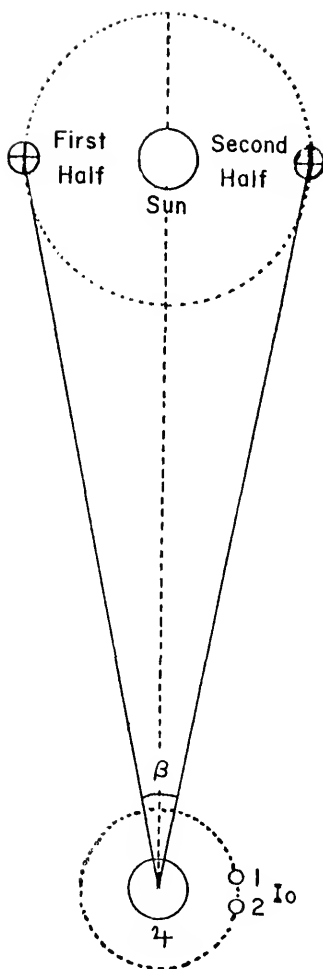


Figure V-6. Illustration of the maximum value of the angular change in the sun-Jupiter-earth angle from the first half of an apparition to the second half. When the earth is in the position shown during the first half of an apparition, Io must be in position 1 for Io-related source-B radiation to be received. The second position of Io is necessary for reception of Io-B radiation at the earth's indicated second-half position.

in the first half of all apparitions to 0.050 for the second half. This is not surprising since Jupiter is positioned in the early morning sky during the first half of an apparition, and the conditions for radio reception are generally better at that time. The change in the probability does, however, provide initial confirmation of an effect observed by Gruber (1965). He divided the apparitions into 15-day periods and discovered a large decrease in the reception probability just after opposition. Analysis of the Florida-Texas data base in a similar vein might be a worthwhile future project.

One major difficulty with the Goertz model seems to be the polarization. He predicts a larger ratio of left-hand polarization as the sub-Io longitude nears the north magnetic pole. This is based on the assumption that the radiation is emitted in the extraordinary mode with right-hand polarization emanating from the northern hemisphere and left-hand polarization from the southern hemisphere. The reverse seems to be true, because source C, the only major source of left-hand polarization that Goertz has included, is farther from the pole in sub-Io longitude than the dominant right-handed  $B_1$  source. If the left-hand polarization of source D were added to the picture the symmetry of polarization about the pole longitude would be more complete since Io-related D lies at sub-Io longitudes farther from the pole than sources A and  $B_2$ . In general, the source Goertz has considered to be  $B_2$  might be better labeled as source D, or a combination of the two. Indeed, the majority of theoreticians have called the radiation which has the beaming characteristics of  $B_2$ , as illustrated in Figure V-2, source D.

In summary, the separation of  $B_1$  and  $B_2$ , if such a division exists, is probably a phenomenon associated with the location of the north

magnetic pole and its effect on the surrounding plasma. Further arguments concerning the link between sources  $B_1$ ,  $B_2$ , and D will be presented shortly, but first let us consider some of the other theories in regard to wave propagation.

### 5.3 Beaming of the Sources

Hypotheses concerning the exact mechanism responsible for production of Io-related storms span a wide range of possibilities. We are more concerned with the subsequent propagation of the radiation away from the point of origin. In discussion of emission geometry theories fall into two categories—those in which the beaming is perpendicular, or nearly perpendicular, to the magnetic flux lines passing through Io, and those involving beaming in or close to the direction of the magnetic flux tube. The former category is by far the more popular. One notable exception to these two classes is the model of Gledhill (1967). In this case the point of origin was assumed to be near Io, as the satellite perturbed a disk of plasma while passing through it. This theory is generally disregarded today since it requires an inordinately high plasma density in Io's vicinity, which is inconsistent with Pioneer spacecraft findings.

Through the years, Ellis (1965) and McCulloch (1971) have developed a theory which represents the case of emission aligned with the magnetic field. In this model Io is assumed to generate whistler radiation and, as described by McCulloch, the waves propagate forward and backward to higher and lower longitudes than the sub-Io meridian. The finite time of travel in combination with the rotation of Jupiter under Io causes the rays to intersect the planet at asymmetrical angular distances from the sub-Io longitude. It is also assumed that the rays must intersect the planet at

magnetic latitudes between  $75^\circ$  and  $80^\circ$  so that the radiation generated will be beamed toward earth. The most efficient time for this to happen is when Io passes the longitude of the north magnetic pole. McCulloch finds that the sum of these conditions yields two peaks of radiation intensity corresponding to the positions of Io-related sources A and B. A  $\lambda_{III}$  versus  $\phi_{Io}$  contour plot of the predicted relative intensity near 30 MHz closely resembles the observed shape of source B. There is a projection similar to the  $B_2$  bulge found at 30 and 27 MHz. McCulloch also computes a one-dimensional Io-phase histogram of relative intensity. The source-B peak follows observed asymmetry since it rises slowly and falls off more rapidly with increasing Io phase. Unfortunately, the predictions for source A are not as successful. According to the theory, A behaves as a mirror image of B about the sub-Io longitude of the pole. The two-dimensional contour plot shows a projection to the high Io-phase, high longitude side of source A that does not match observations. The one-dimensional Io-phase peak rises rapidly and has a slower descent, which also opposes reality. It can be argued that the plots are of relative intensity rather than occurrence probability, but the probability should roughly follow the intensity profiles. McCulloch does not discuss sources C and D, but addition of southern hemisphere effects would probably be necessary to explain them. The model has its shortcomings, but its strengths should be kept in mind as an alternate method of beaming.

The great majority of the newer theories subscribe to the perpendicular beaming patterns illustrated in Figure V-2. This requires some explanation of the asymmetry of the position of Io about the earth-Jupiter line at the time of Io-controlled storms. Most theories invoke some system which allows the point of origin to occur at a longitude  $15^\circ$  lower than that under Io,



since this would symmetrize the starting positions. As an example, we have already discussed the Goertz model in which Io perturbs the magnetic field lines by its passage. MHD waves change the orientation of the flux lines and cause the disturbance created by Io to penetrate the ionosphere at a longitude  $15^\circ$  lower than the sub-Io longitude. Another explanation involves the assumption of high conductivity for Io as suggested by Goldreich and Lynden-Ball (1969) or Piddington and Drake (1968). In this case, charged particles are accelerated along the magnetic flux tube moving with Io. The motion of the flux tube gives rise to a magnetic torque which bends the field lines forward by  $15^\circ$ . Restoration of symmetry by bending of the field line is illustrated in Figure V-2 by the curves connecting Io to Jupiter. Finally, for one other example, Wu et al. (1973) assumed the disturbance to occur at the sub-Io longitude, but slow propagation of the radiation through the corotating magnetosphere prevents escape until the sub-Io longitude has increased by  $15^\circ$ .

If the Io-related radiation effectively originates from longitudes  $75^\circ$  on either side of the earth-Jupiter line, one must still explain why the storms are maximized for the  $75^\circ$  angle. The dominant theory for the emission mechanism is coherent cyclotron radiation by electrons moving in bunches up or down the flux lines. In the frame of reference moving with the electrons the radiation is emitted perpendicular to the field lines. To the outside observer radiation emerges in a conical sheet about the direction of motion at an angle near the required  $75^\circ$ . If the cone is beamed toward the planet it will be reflected without loss of cone angle by increased plasma densities at lower levels.

As a final step in using perpendicular beaming, some method of modulation must be invoked to explain why the cone of radiation can be

received on earth only for particular ranges of sub-Io longitude. We have seen that Cavaliere and Speranza limit the emission regions by the boundaries of the non-Io-related A and B sources, and Goertz believes sufficient amplification of the radiation can occur only when Io is near the north magnetic pole. Goldreich and Lynden-Bell theorized that radiation is strong only in parts of the emission cone. Only at times when the active portion of the cone points toward the observer will storms be received. In the original work by Dulk (1965) it was suggested that the orientation of the magnetic field may allow intersection of the radiation cone and the ecliptic plane containing the earth only when Io is in northern magnetic latitudes and, therefore, in the longitudes surrounding the north magnetic pole.

The diversity of theories which share similar explanations of beaming geometry stresses the importance of this aspect of emission. It is possible to generalize these similarities and use them in conjunction with models of the magnetic field in order to predict the source structure. Schatten and Ness (1971) calculated emission directions for both the dipolar magnetic offset from the center of Jupiter as suggested by Warwick (1963) and a centered, tilted magnetic dipole. They assumed the radiation emanates in a cone at angles between  $80^\circ$  and  $100^\circ$  to the line of magnetic flux. Predictions of probability for  $30^\circ$  by  $30^\circ$  intervals in Io phase and System III longitude were computed. General agreement with the positions of the four Io-related sources was found, but the constraints were insufficient for determination of structure.

Recent measurements of the Jovian magnetic field geometry by two magnetometers aboard the Pioneer spacecraft (Smith *et al.*, 1975; Acuna and Ness, 1976) have provided a more definitive basis for calculations.

Both sets of investigators described the magnetic field in terms of a spherical harmonic analysis of the magnetic potential as represented below.

$$V = \sum_{n=1}^k \left(\frac{r}{a}\right)^n T_n^e + \left(\frac{a}{r}\right)^{n+1} T_n^i \quad (V-1)$$

where

$$T_n^e = \sum_{m=0}^n P_n^m(\cos\theta) [G_n^m \cos m\phi + H_n^m \sin m\phi] \quad (V-2)$$

$$T_n^i = \sum_{m=0}^n P_n^m(\cos\theta) [g_n^m \cos m\phi + h_n^m \sin m\phi] \quad (V-3)$$

The superscript *e* refers to external contributions to the field, *i* stands for internal field sources, *a* is the radius of Jupiter, and *k* is the maximum order to which the analysis is applied. The  $P_n^m(\cos\theta)$  are the Schmitt-normalized associated Legendre functions, and  $G_n^m$ ,  $H_n^m$ ,  $g_n^m$ , and  $h_n^m$  are the Schmitt coefficients. Finally,  $\theta$  and  $\phi$  are the co-latitude and Jovian east longitude, respectively. The magnetic field can be determined by computing

$$\vec{B} = -\nabla V \quad (V-4)$$

Usually the external source coefficients contribute negligibly (see Smith et al., 1975) for points close to the planet and they are neglected in the present analysis. Each group of investigators carried out their computation to include octopolar moments of the field ( $k=3$ ). The calculated coefficients are summarized in Table V-1.

Once the coefficients are known, it is a simple matter to compute the location of the intersection with the Jovian surface of the magnetic field lines passing through Io. Beginning at Io, the flux lines are

Table V-1  
Octopolar Field Coefficients

	Smith et al. (1975)	Acuna and Ness (1976)
$g_1^0$	4.129	4.218
$g_1^1$	-0.492	-0.440
$h_1^1$	0.531	0.563
$g_2^0$	0.042	-0.203
$g_2^1$	-0.738	-0.871
$g_2^2$	0.324	0.331
$h_2^1$	-0.050	-0.037
$h_2^2$	-0.381	-0.402
$g_3^0$	0.092	-0.233
$g_3^1$	-0.413	-0.357
$g_3^2$	0.335	0.506
$g_3^3$	-0.239	-0.292
$h_3^1$	-0.084	-0.463
$h_3^2$	0.002	0.096
$h_3^3$	0.118	0.233

followed in iterative steps to the points of interest at or near the planet's cloudtop level. Comparison of the source morphology with sample beaming patterns computed at selected points is now possible. The radiation will be assumed to emerge from the selected location in a conical sheet opening at an angle  $\gamma$  about the magnetic flux line. In coherent cyclotron radiation the angle  $\gamma$  is determined by the speed  $v$  of the electron along the magnetic field.

$$\gamma = \frac{\pi}{2} - \frac{v}{c} \quad (V-5)$$

Inward or outward pointing of the cone axis does not matter since inward-directed waves will be reflected at lower levels, leaving the cone angle unchanged. The effects of stop zones and of refraction in the plasmasphere will not be included. They may be of importance to the beam propagation, but computation of their influence is a complicated process in which accuracy depends upon the validity of the assumed model of the plasma distribution. If the plasma were a major factor in the radiation propagation, any instabilities in the plasma should be noticeable as large changes of source structure. Consistency of the source morphology over many years suggests that modulation of emission direction by the plasma is small. Consequently, it will be neglected in this simple analysis of beaming geometry.

Figures V-7a and V-7b, adapted from Goertz (1973), illustrate the relevant variables for determination of the intersection of the radiation cone with the plane of the ecliptic, which is the earth's viewpoint. The radiation is beamed at an angle  $\mu$  on either side of the projection of the magnetic field line on the ecliptic plane. If  $\tau$  is the angle between the field line and the plane of the ecliptic, then  $\mu$  can be computed

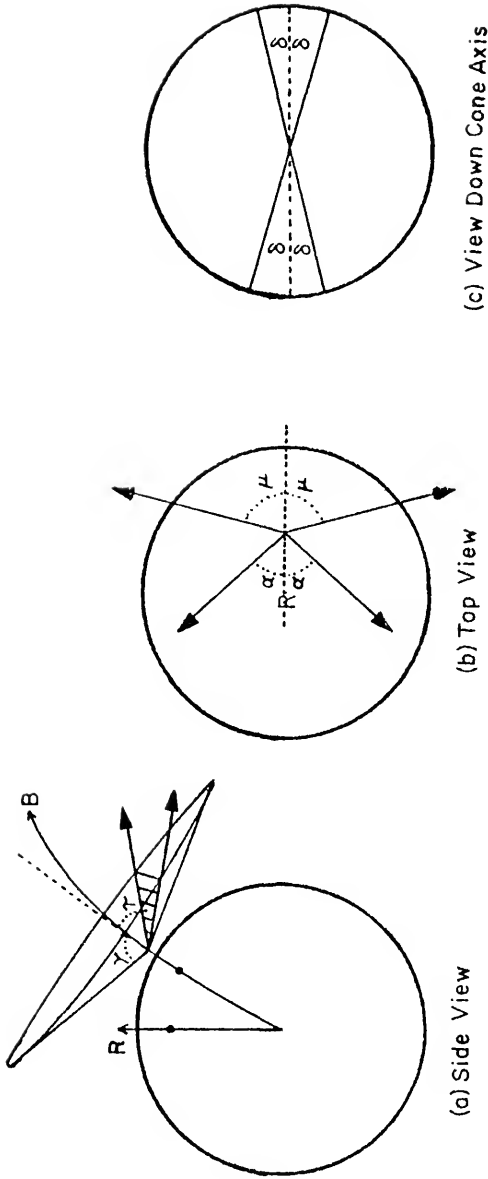


Figure V-7. Illustration of the variables used in calculation of beaming directions for radiation emitted in a conical sheet about the magnetic field line. Figure (a) is a view of Jupiter from the side showing the radiation cone opening at an angle  $\gamma$  about the magnetic flux line  $B$ . Figure (b) is a view from above the north pole of Jupiter displaying the intersection of the emission cone with the plane of the ecliptic at an angle  $\mu$  on either side of the projection of the field line. The angles  $\alpha$  in the top view represent the limits of radiation obscuration in the plane of the ecliptic caused by the planet. Obscuration will be discussed in a later section. Figure (c) looks down the cone axis and shows the angle  $\delta$  which determines what portion of the cone contains radiation. Further explanations are in the text.

from the equation

$$\tan^2 \mu = \tan^2 \gamma \cos^2 \tau - \sin^2 \tau \quad (V-6)$$

Unless the emission cone does not intersect the ecliptic plane, storms will be directed toward the earth for all sub-Io longitudes. As discussed previously, some form of modulation must be introduced to limit the emission range.

We will adopt the limit proposed by Goldreich and Lynden-Bell, that the radiation is emitted only within the portion of the cone defined by the angle  $\delta$  in Figure V-7c. In the figure, the cone is projected onto a plane perpendicular to the cone axis. Maximum emission occurs in the portion of the cone parallel to the lines of magnetic latitude, represented by the dashed line. Beyond an angle  $\delta$  on either side of the magnetic latitude line radiation is negligible. Reception of storms will be possible only when

$$\tan \tau \leq \tan \gamma \sin \delta \quad (V-7)$$

We will also assume that the flux lines will lead Io by  $15^\circ$  in longitude. This is effected by increasing the sub-Io longitude by  $15^\circ$  in the calculations. This is not the same as a warping of the magnetic field line, but the results should not be too different. The final assumption requires emission at the point where the electron gyrofrequency determined by the magnetic field strength equals the frequency of the emitted wave. Since comparison will be made with 18, 20, and 22-MHz source structure, the gyrofrequency of 20 MHz has been chosen.

Figure V-8 exhibits the calculated values of  $\lambda_{III}$  and  $\phi_{IO}$  for which radiation can be received from the northern hemisphere foot of Io's

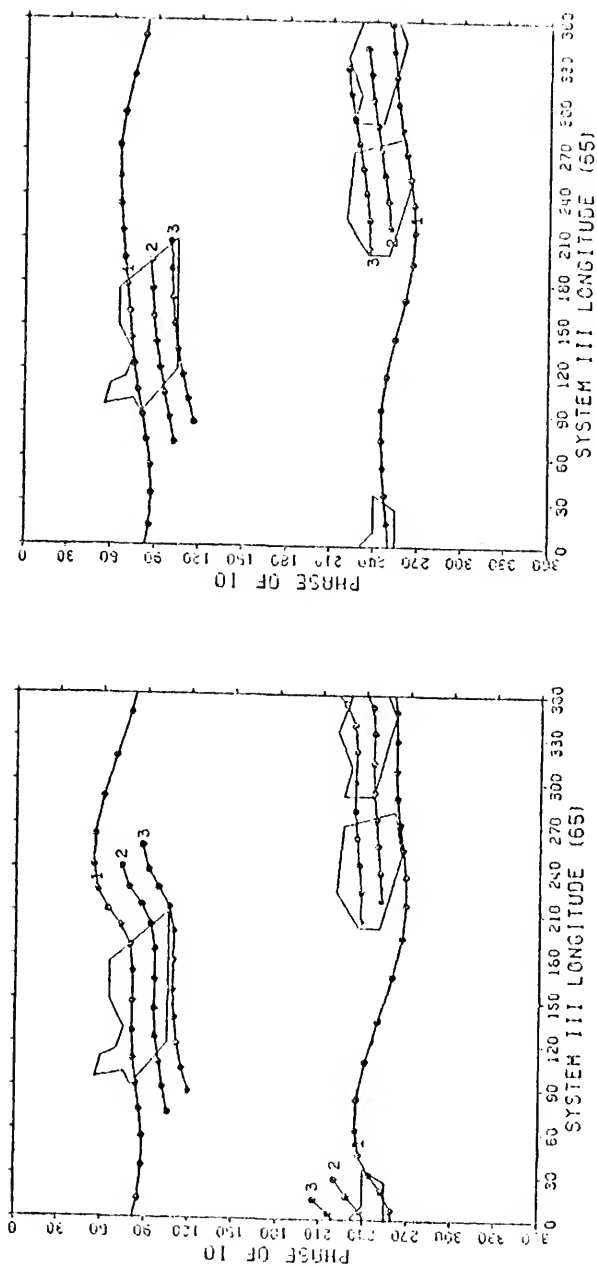


Figure V-8.

Predicted Io-phase and System III longitude (65) angles for which 20-MHz Io-related decametric radiation beamed from the northern hemisphere will be observed on earth. The points on the lines were determined by calculations based on the Goldreich and Lynden-Bell (1969) model made at  $20^\circ$  intervals in sub-Io longitude for three sets of parameters. The octopolar magnetic field model of Acuna and Ness (1975) was used for the diagram on the left, and the plot on the right employs the Smith et al. model. For the numbered curves, the values of the cone opening angle  $\gamma$  and cone limiting angle  $\delta$  were: (1)  $90^\circ$ , indeterminate; (2)  $79^\circ$ ,  $13^\circ$ ; and (3)  $70^\circ$ ,  $25^\circ$ .



flux tube with the given assumptions. The left diagram corresponds to use of the Acuna and Ness magnetic field model, and the diagram on the right utilizes the model of Smith et al. The points have been computed for  $20^\circ$  intervals in sub- $I_0$  longitude and the lines interpolate these values. Rough outlines of the mid-decametric sources, based on diagrams like Figures V-1 and V-4, have been provided for reference. To help visualize the effects of different values for the variables, three sets of parameters have been used.

The sources are well-covered by variations in cone angle between  $70^\circ$  and  $90^\circ$ . In source B, especially, the sharp cutoff of the lower edge is followed by the  $70^\circ$  curve. From equation V-5 this can be interpreted as a cutoff of about 30 keV for electron motion along the field line. As originally suggested by Dulk (1965), a cone angle of  $79^\circ$  passes through or very near the areas of maximum probability. The angle of  $90^\circ$ , corresponding to the least motion parallel to the field, covers the lower-probability upper part of source B. As a consequence, the asymmetry of the source-B peak in  $I_0$  phase implies a parallel velocity distribution for the radiating electrons. The number of electrons builds up slowly as parallel speed increases and reaches a maximum for a cone angle of  $79^\circ$ , followed by a rapid decline in the number at higher energies. The reverse would be the case for the opposite lower-frequency asymmetries.

From Figure V-8 we see that for any given asymmetry in  $I_0$  phase for B, A and C should have opposite skews since the cone angle increases with decreasing  $I_0$  phase in those sources. This opposing symmetry is not found.  $I_0$ -A and  $I_0$ -C have a higher mixture of non- $I_0$  radiation to confuse the identification, but their direction of skew is still unmistakable. One

possible differentiating influence is the aforementioned occurrence of A and C on the hotter afternoon side of the planet which may change the parallel velocity distributions.

For both magnetic field models in Figure V-8 part of source A extends beyond the  $70^\circ$  cutoff, implying higher speeds for the electrons along the field line, but this may be the confusion of the non-Io radiation blending into the source at those longitudes. The locations of the  $B_1$  and  $B_2$  bulges intimate cone angles greater than  $90^\circ$  which may in a sense be true. This discussion will be more apropos in the next section.

The longitudinal width predicted for the sources depends upon  $\delta$ . Inspection of equation V-7 shows confinement of radiation to the part of the cone determined by  $\delta$  to be the same as limiting the activity to a symmetrical longitude range about the north magnetic pole, since the angle  $\tau$  will be minimized at the pole longitude. Thus, the theory of Goldreich and Lynden-Bell is similar in effect to the models of Goertz, Cavaliere and Speranza, and many others, except in the case where  $\gamma$  is close to  $90^\circ$ . In that situation  $\delta$  makes no difference and, theoretically, emission occurs at all longitudes, but other considerations in the beaming process should provide a second limit. The value of  $13^\circ$  for  $\delta$  when  $\gamma=79^\circ$  was suggested by Goldreich and Lynden-Bell. The calculated width agrees well with sources A and C, but overextends source B. This is, of course, a revisiting of the problem of comparing sources  $B_1$  and  $B_2$  with sources A and C. Angular separation of sources A and C in sub-Io longitude is greater than the separation of sources  $B_1$  and  $B_2$ , and this prevents the calculated width of one of the source pairs from matching the observed extent for the other. An increase of  $\delta$  from  $13^\circ$  to  $25^\circ$  is necessary to achieve the same source width when  $\gamma$  changes from  $79^\circ$  to  $70^\circ$ . The overextension of B does reveal

that the radiation slants into the source-D region on the low-longitude side. Also, the Acuna-Ness model exhibits the upward turn often observed on the right side of source C. After the upward turn, the line of expected radiation follows the curve of the "bridge" observed between sources A and C at the lower frequencies. This will be discussed at greater length in the next section, where geometrical limits for the beaming directions are proposed.

#### 5.4 Radiation Obscuration

The hypothesis that the decametric radiation takes place near the intersection of Io's magnetic flux tube with the Jovian cloudtop layer brings up the question of when these regions will be obscured from view by the planetary limb. Alexander et al. (1975b) answered this query for the simplest configuration, in which the radiating region is assumed to be at the Jovian cloudtop layer. In that case, the active areas will be visible only when they are on the side of Jupiter facing the earth. In this situation the longitudes and phases of Io for which the radiation is obscured are the shaded sections of Figure V-9, which has been calculated according to the method of Alexander et al. assuming the declination of the earth to be zero. No warping of the Io flux tube or similar symmetrizing hypotheses have been included. Occultation in both the northern and southern hemispheres is shown. Similar calculations for the Smith et al. (1975) magnetic field model showed no significant differences. At first, the figure suggests the northern hemisphere origins of sources B and A, while C would propagate from the south. Emission from cloudtop level is not realistic, however. If radiation occurs at the altitude where the electron gyrofrequency equals the emitted frequency, then a totally different picture emerges.

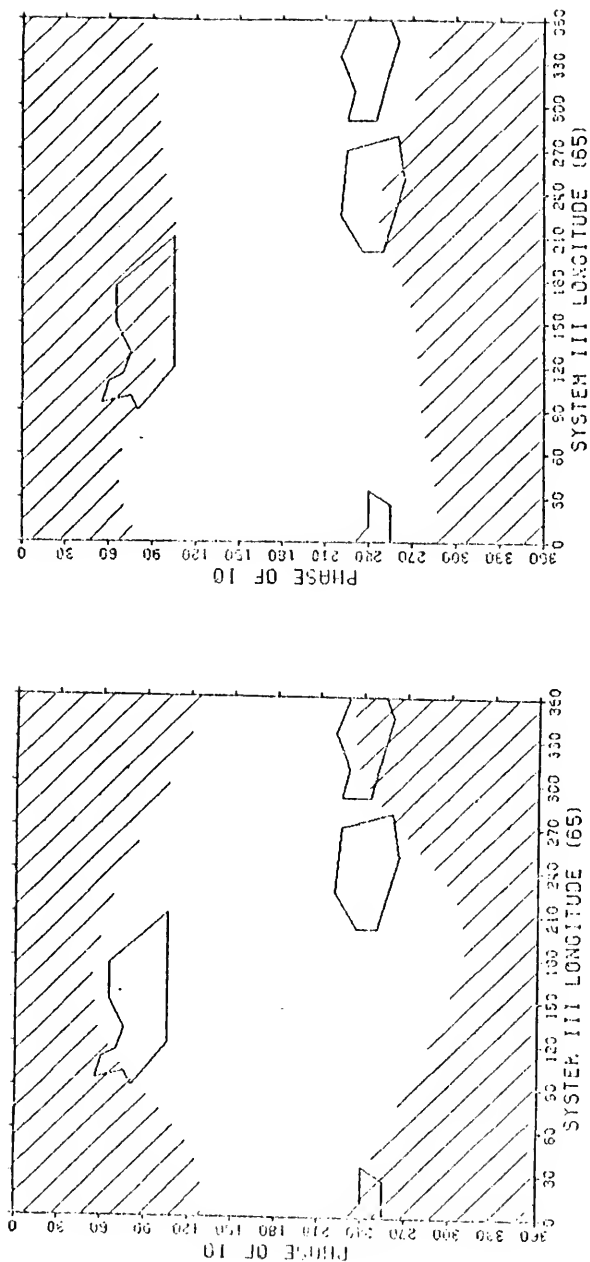


Figure V-9. Shaded regions indicate the predicted System III longitude (65) and Io-phase angles for which radiation emitted toward earth from the intersection of Io's magnetic flux tube with the Jovian surface will be occulted by the planetary disk, based on the octopolar magnetic field model of Acuna and Ness (1975) and a similar diagram by Alexander, et al. (1975b). The left diagram represents calculations for the northern hemisphere flux tube and the plot on the right shows the computations for the southern hemisphere flux tube. Io-related source outlines are included for comparison.

Calculation of angles of obscuration for points above the planet's cloud surface is simplest for the assumption that  $D_E$  is zero. Figure V-7b shows an example in which all radiation in the ecliptic plane within the angle  $2\alpha$  is cut off. Account must be taken of the rotational flattening of Jupiter, and this has been done through the equation

$$R = R_j (1 - \epsilon \cos^2 \theta) \quad (V-8)$$

where  $R$  is the planetary radius at co-latitude  $\theta$ ,  $R_j$  is the equatorial radius, and  $\epsilon$  is the ellipticity (see Table I-1). The correction is important since the appropriate gyrofrequency position may be so deep in the atmosphere that the density of gases makes emission impossible. For ease of calculation, the cloudbottom layer will be assumed to represent this depth.

Results of the calculations for the 20-MHz gyrofrequency level in both the northern and southern hemispheres are shown in Figure V-10. The northern hemisphere shaded regions have an interesting border with source B. We can infer that the high-longitude edge of the source may be cut off by the submersion of the 20-MHz emission region in the cloud layer. By the same argument, the right half of source C should not appear, or else we must again assume that C originates in the southern hemisphere. Strict belief in the calculated locations of the obscured areas is not advisable, since the equations are very sensitive to changes in altitude. For example, the shaded regions for the 22-MHz level in Figure V-11 would imply a narrowing of source B by nearly  $15^\circ$ , and the same computations performed for a frequency of 20 MHz with the Smith et al. (1975) magnetic field model (Figure V-12) show no danger of any source obscuration. We conclude that our knowledge of the magnetic field is insufficient for accurate

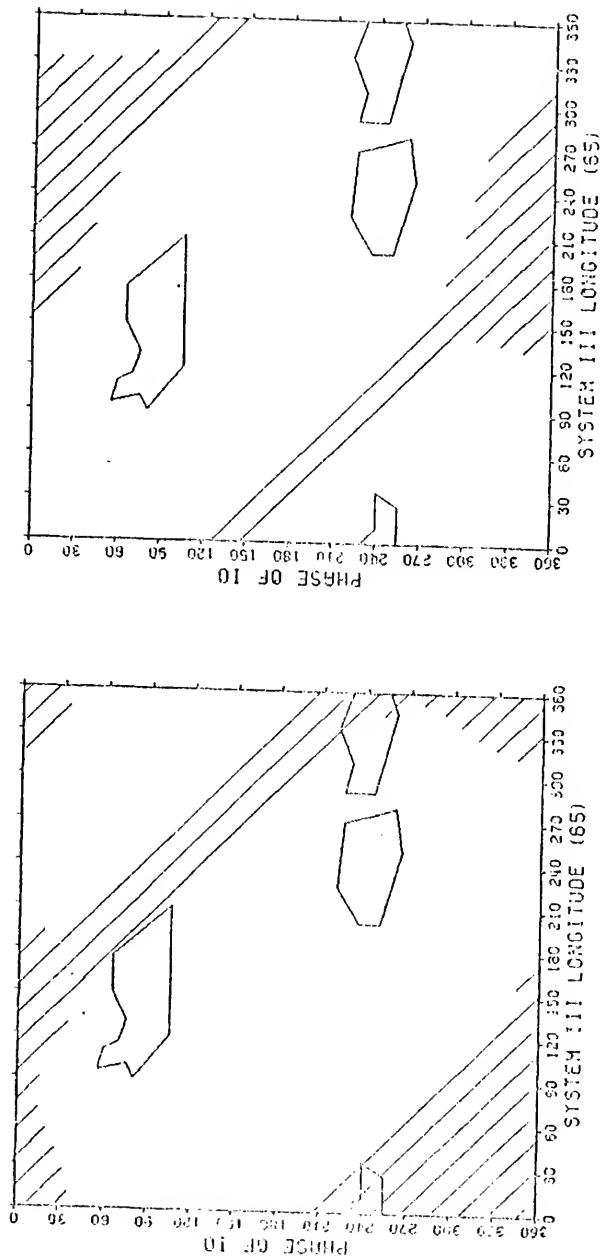


Figure V-10.

Shaded regions indicate the predicted System III longitude (65) and Io-phase angles for which 20-MHz radiation emitted toward earth from Io's magnetic flux tube will be occulted by the planetary disk. The calculations are based on the octopolar magnetic field model of Acuna and Ness (1975). Emission is assumed to occur at the point where the electron gyrofrequency equals 20 MHz. The left diagram represents calculations for the northern hemisphere flux tube and the plot on the right shows the computations for the southern hemisphere flux tube. Io-related source outlines are included for comparison.

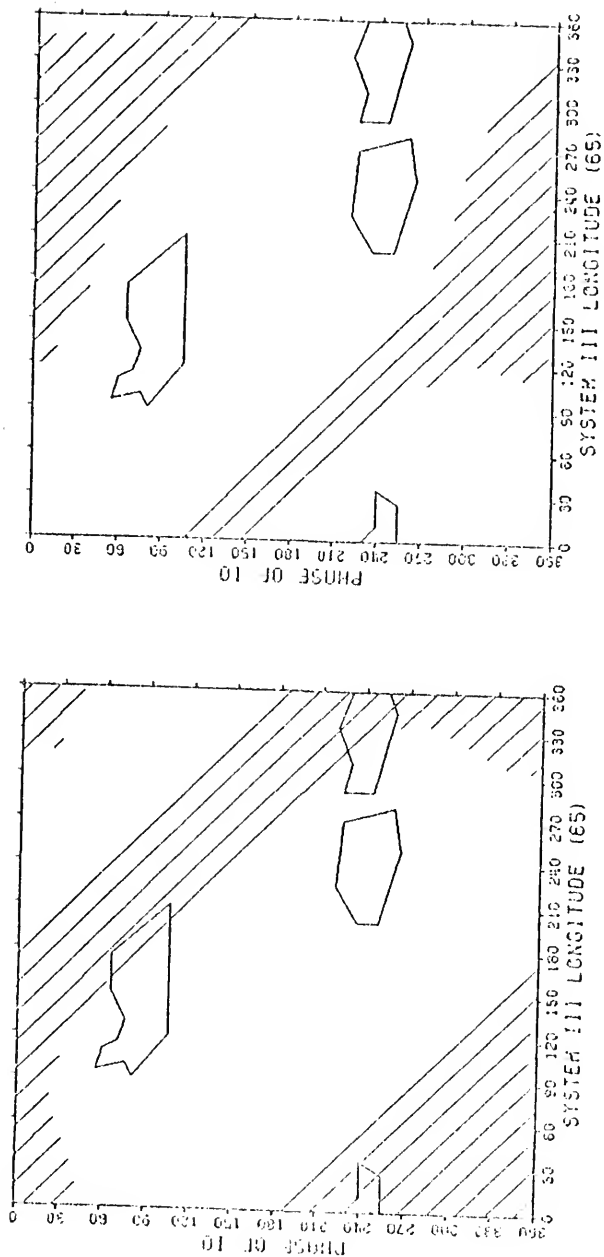


Figure V-11.

Shaded regions indicate the predicted System III longitude (65) and Io-phase angles for which 22-MHz radiation emitted toward earth from Io's magnetic flux tube will be occulted by the planetary disk. The calculations are based on the octopolar magnetic field model of Acuna and Ness (1975). Emission is assumed to occur at the point where the electron gyrofrequency equals 22 MHz. The left diagram represents calculations for the northern hemisphere flux tube and the plot on the right shows the computations for the southern hemisphere flux tube. Io-related source outlines are included for comparison.

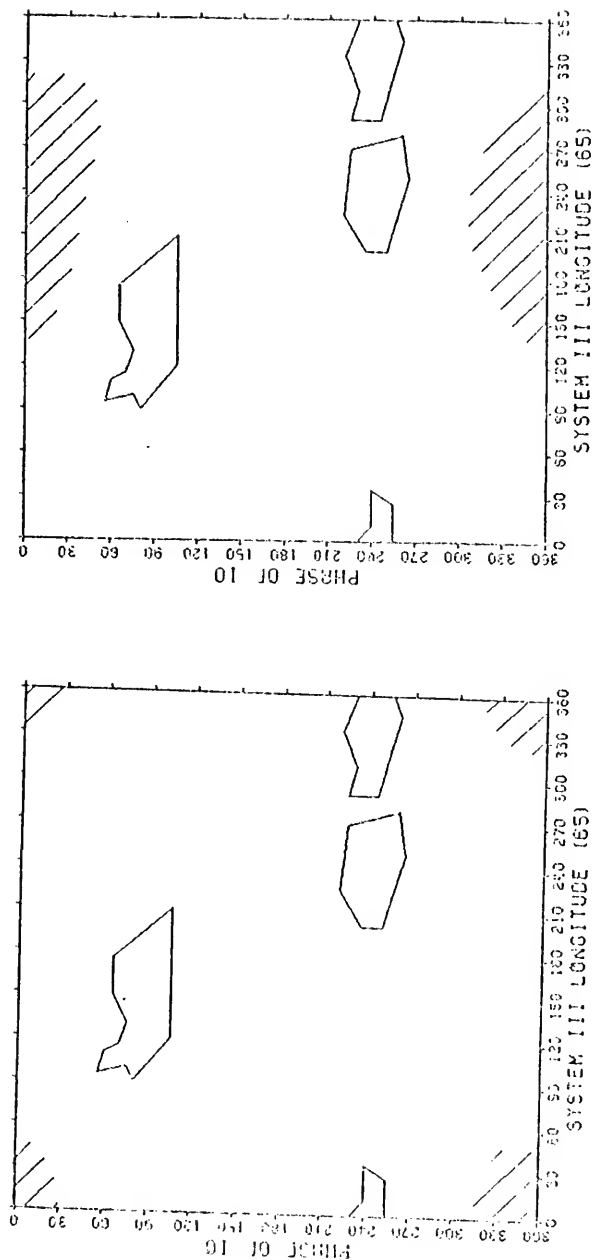


Figure V-12.

Shaded regions indicate the predicted System III longitude (65) and Io-phase angles for which 20-MHz radiation emitted toward earth from Io's magnetic flux tube will be occulted by the planetary disk. The calculations are based on the octopolar magnetic field model of Smith et al. (1975). Emission is assumed to occur at the point where the electron gyrofrequency equals 20 MHz. The left diagram represents calculations for the northern hemisphere flux tube and the plot on the right shows the computations for the southern hemisphere flux tube. Io-related source outlines are included for comparison.



calculations near the planetary surface. The Pioneer spacecraft did not pass close enough to Jupiter nor remain long enough for an accurate determination of the magnetic field near the clouds to be possible. The diagrams do indicate, however, some plausible explanations for source morphology in terms of obscuration.

The more likely altitude for cutoff of the decametric radiation is above the cloud layer and dependent on the plasma density. Refraction will also depend on this factor, and so the amount of obscuration may change from one side of the planet to the other as plasma parameters vary. With this in mind, it is possible to cut off the right side of source B by submersion of the radiating region without endangering a northern hemisphere source C. At many times the left side of source B also exhibits the linear slant characteristic of a submersion cutoff. If the left side of the source is masked at 20 MHz, then a decrease in gyrofrequency to 15 MHz would increase the emission altitude. This would allow radiation from the source D region on the left side of source B as shown in Figure V-8. At the same time removal of the cutoff would reveal the bridge of radiation between sources A and C. At still lower frequencies no obscuration occurs and there would be a continuous band of radiation at Io phases of  $90^\circ$  and  $240^\circ$ . Preliminary results of Desch and Carr (1977) around 4 MHz support this statement.

Finally, the  $B_1$  and  $B_2$  bulges could also be a facet of source visibility. An inward-directed radiation cone may not be entirely reflected, and some of the emission may escape by just grazing the top of the reflection layer. In this sense the cone angle will be greater than  $90^\circ$ . This is more likely to occur when the declination of the earth is positive, and that is the time the  $B_1$  and  $B_2$  bulges appear. The

intervening null zone would still be an effect of conditions directly over the magnetic pole, such as the lowered amplification factor proposed by Goertz. Variation of emission position with gyrofrequency would be a possible source of the fluctuation of the bulges with frequency.

### 5.5 Summary

In the course of Chapter V we have attempted to compare the second-order source characteristics with predictions of the relevant theories. Explanation of the source-B anomaly has led to speculations concerning the separate existence of sources  $B_1$  and  $B_2$  and their possible symmetry with sources A and C. The general locations of the Io-triggered sources in Io phase and System III longitude agree well with predictions assuming emission in a conical sheet opening at an angle from  $70^\circ$  to  $90^\circ$  about the magnetic flux line, based on the Pioneer 11 octopolar magnetic field models. Beaming directions have been calculated in the formalism of the Goldreich and Lynden-Bell model with activity occurring at longitudes  $15^\circ$  less than the sub-Io longitude and beamed into small sections of the conical sheet. The emission geometry proposed by many other perpendicular-beaming theories has been shown to be nearly interchangeable with the Goldreich and Lynden-Bell system. Finally, many of the second-order source attributes revealed in the previous chapters may be explained as occultation of the emission region by the planet's cloud surface or by an impenetrably dense plasma, but the magnetic field is not yet sufficiently determined for the effects to be computed accurately. Hope for the near future rests in the Voyager spacecraft, one of which is intended to penetrate the Io flux tube. At that time there should be a large advance in determining the origin of many of the above phenomena, yet, as in all past space ventures, we know many new enigmas will arise. In any event, Godspeed.

# LIST OF REFERENCES

- Acuna, M.H., and Ness, N.F., "The Main Magnetic Field of Jupiter," J. Geophys. Res., 81, 2917 (1976).
- Alexander, J.K., "Note on the Beaming of Jupiter's Decameter-Wave Radiation and Its Effect on Radio Rotation Period Determinations," Ap. J., 195, 227 (1975).
- Alexander, J.K., Kaiser, M.L., and Vaughan, S.S., "Decameter-Wave Radio Observations of Jupiter: Apparitions of 1970-1974," NASA-GSFC document X-693-75-48 (1975a).
- Alexander, J.K., Smith, R.A., Kaiser, M.L., Acuna, M.H., and Thompson, R.F., "Implications of Pioneer-11 Magnetic Field Models for Jupiter's Decametric Radio Emission," NASA-GSFC document X-693-75-258 (1975b).
- Allen, C.W., Astrophysical Quantities, Oxford University Press, Inc., New York (1973).
- American Ephemeris and Nautical Almanac, U.S. Government Printing Office, Washington, D.C. (1976).
- Anderson, J.D., Null, G.W., and Wong, S.K., "Gravity Results from Pioneer 10 Doppler Data," J. Geophys. Res., 79, 35 (1974).
- Berge, G.L., "An interferometric Study of Jupiter's Decimeter Radio Emission," Ap. J., 146, 767 (1966).
- Bigg, E.K., "Influence of the Satellite Io on Jupiter's Decametric Emission," Nature, 203, 1008 (1964).
- Bozyan, F.A., and Douglas, J.N., "Directivity and Stimulation in Jovian Decametric Radiation," J. Geophys. Res., 19, 3387 (1975).
- Bozyan, F.A., Douglas, J.N., and Gopala Rao, U.V., "Catalog of Decameter Observations of Jupiter," Publ. of the Dept. of Astron., The Univ. of Texas at Austin, Ser. II, 3, No. 8, (1972).
- Branson, N.F.B.A., "High Resolution Radio Observations of the Planet Jupiter," Mon. Not. Royal Astron. Soc., 139, 155 (1968).
- Brown, L.W., "Spectral Behavior of Jupiter near 1 MHz," Ap. J. (Letters), 194, L159 (1974a).

- Brown, L.W., "Jupiter Emission Observed near 1 MHz," *Ap. J.*, 192, 547 (1974b).
- Burke, B.F., and Franklin, K.L., "Observations of a Variable Radio Source Associated with the Planet Jupiter," *J. Geophys. Res.*, 60, 213 (1955).
- Carr, T.D., "The Possible Role of Field-Aligned Ducts in the Escape of Decametric Radiation from Jupiter," paper presented at NASA Conf. Jupiter, New York (1962).
- Carr, T.D., "Jupiter's Magnetospheric Rotation Period," *Ap. Letters*, 7, 157 (1971).
- Carr, T.D., "Jupiter's Decametric Rotation Period and the Source A Emission Beam," *Phys. Earth Planet. Interiors*, 6, 21 (1972).
- Carr, T.D., Brown, G.W., Smith, A.G., Higgins, C.S., Bollhagen, H., May, J., and Levy, J., "Spectral Distribution of the Decametric Radiation from Jupiter in 1961," *Ap. J.*, 140, 778 (1964).
- Carr, T.D., and Desch, M.D., "A Review of Recent Decametric and Hectometric Observations of Jupiter," *Jupiter: The Giant Planet*, edited by T. Gehrels, University of Arizona Press, Tucson (1975).
- Carr, T.D., and Gulkis, S., "The Magnetosphere of Jupiter," *Ann. Rev. Astron. Astrophys.*, 7, 577 (1969).
- Cavaliere, A., and Speranza, A., "Decametric Radio Emission from Jupiter," *Ap. Letters*, 10, 9 (1971).
- Desch, M.D., and Carr, T.D., "Decametric and Hectometric Observations of Jupiter from the RAE-1 Satellite," *Ap. J.* L57 (1974).
- Desch, M.D., and Carr, T.D., manuscript in preparation (1977).
- Desch, M.D., Carr, T.D., and Levy, J., "Observations of Jupiter at 26.3 MHz Using a Large Array," *Icarus*, 25, 12 (1975).
- Donivan, F.F., and Carr, T.D., "Jupiter's Decametric Rotation Period," *Ap. J. (Letters)*, 157, L65 (1969).
- Douglas, J.N., "Decametric Radiation from Jupiter," *IEEE Trans. Mil. Electron.*, MIL-8, 173 (1964).
- Douglas, J.N., and Smith, H.J., "Decametric Radiation from Jupiter. I. Synoptic Observations 1957-1961," *Astron. J.*, 68, 163 (1963).
- Douglas, J.N., and Smith, H.J., "Interplanetary Scintillation in Jovian Decametric Radiation," *Ap. J.*, 148, 885 (1967).
- Drake, F.D., and Hvatum, S., "Non-Thermal Microwave Radiation from Jupiter," *Astron. J.*, 64, 329 (1959).

- Dulk, G.A., "Io-Related Radio Emission from Jupiter," Ph.D. Dissertation, University of Colorado, Boulder, Colorado (1965).
- Duncan, R.A., "Jupiter's Rotation," *Planet. Space Sci.*, 19, 391 (1971).
- Ellis, G.R.A., "The Decametric Radio Emissions of Jupiter," *Radio Science*, 69D, 1513 (1965).
- Gallet, R.M., *Planets and Satellites*, edited by G.P. Kuiper and B.M. Middlehurst, Univ. Chicago Press (1961).
- Gledhill, J.A., "Magnetosphere of Jupiter," *Nature*, 214, 155 (1967).
- Goertz, C.K., "Variation of Source A Position of the Jovian Decametric Radiation," *Nature*, 229, 151 (1971).
- Goertz, C.K., "The Io-Controlled Decametric Radiation," *Planet. Space Sci.*, 21, 1431 (1973).
- Goldreich, P., and Lynden-Bell, D., "Io, A Jovian Unipolar Inductor," *Ap. J.*, 156, 59 (1969).
- Gruber, G.M., "Possible Contribution of Jupiter's Magnetospheric Tail to the Radio Emissions of the Planet in the Decametric Region," *Nature*, 208, 1271 (1965).
- Gulkis, S., and Carr, T.D., "Radio Rotation Period of Jupiter," *Science*, 154, 257 (1966).
- International Astronomical Union Information Bulletin, 8 (1962).
- Kennedy, D.J., "Polarization of the Decametric Radiation from Jupiter," Ph.D. Dissertation, University of Florida, Gainesville, Florida (1969).
- Leacock, R.L., "An Extended Analysis of Certain Features of Jupiter's Decametric Emission," Ph.D. Dissertation, University of Florida, Gainesville, Florida (1971).
- Lebo, G.R., "Decameter-Wavelength Radio Observations of the Planets in 1962," Ph.D. Dissertation, University of Florida, Gainesville, Florida (1964).
- Lecacheux, A., "Periodic Variations of the Position of Jovian Decameter Sources in Longitude (System III) and Phase of Io," *Astron. Astrophys.* 37, 301 (1974).
- McCulloch, P.M., "Theory of Io's Effect on Jupiter's Decametric Emissions," *Planet. Space Sci.*, 19, 1297 (1971).
- McCulloch, P.M., and Ellis, G.R.A., "Observations of Jupiter's Decametric Radio Emissions," *Planet. Space Sci.*, 14, 347 (1966).

- Miller, H.R., "Jupiter's Decametric Flux: A Consistent Two-Dimensional Analysis, 1957-1970," Ph.D. Dissertation, University of Florida, Gainesville, Florida (1970).
- Opp, A.G., "Scientific Results from the Pioneer 11 Mission to Jupiter," *Science*, 188, 447 (1975).
- Piddington, J.H., and Drake, J.F., "Electrodynamic Effects of Jupiter's Satellite Io," *Nature*, 217, 935 (1968).
- Register, H.I., "Decameter-Wavelength Radio Observations of the Planet Jupiter 1957-1968," Ph.D. Dissertation, University of Florida, Gainesville, Florida (1968).
- Register, H.I., and Smith, A.G., "A Two Component Model of Changes in Jupiter's Radiofrequency Rotation Period," *Ap. Letters*, 3, 209 (1969).
- Riddle, A.C., and Warwick, J.W., "Redefinition of System III Longitude," *Icarus*, 27, 457 (1976).
- Riihimaa, J.J., "Modulation Lanes in the Dynamic Spectra of Jupiter's Decametric Radio Emission," *Ann. Acad. Sci. Fenn.*, *AVI*, 1 (1974).
- Roberts, J.A., and Ekers, R.D., "The Position of Jupiter's Van Allen Belt," *Icarus*, 5, 149 (1966).
- Schatten, K.H., and Ness, N.F., "The Magnetic Field Geometry of Jupiter and Its Relation to Io-Modulated Jovian Decametric Radio Emission," *Ap. J.*, 165, 621 (1971).
- Smith, A.G., Carr, T.D., and Six, N.F., "Results of Recent Decameter-Wavelength Observations of Jupiter," *La Physique des Planetes*, 24, 543 (1962).
- Smith, A.G., Lebo, G.R., Six, N.F. Jr., Carr, T.D., Bollhagen, H., May, J., and Levy, J., "Decameter-Wavelength Observations of Jupiter: The Apparitions of 1961 and 1962," *Ap. J.*, 141, 457 (1965).
- Smith, E.J., Davis, L. Jr., Jones, D.E., Coleman, P.J. Jr., Colburn, D.S., Dyal, P., and Sonett, C.P., "Jupiter's Magnetic Field, Magnetosphere, and Interaction with the Solar Wind: Pioneer 11," *Science*, 188, 451 (1975).
- Smith, R.A., "Models of Jovian Decametric Radiation," Jupiter: The Giant Planet, edited by T. Gehrels, University of Arizona Press, Tucson (1976).
- Van Allen, J.A., Randall, B.A., Baker, D.N., Goertz, C.K., Sentman, D.D., Thomsen, M.F., and Flindt, H.R., "Pioneer 11 Observations of Energetic Particles in the Jovian Magnetosphere," *Science*, 188, 459 (1975).

- Warwick, J.W., "Dynamic Spectra of Jupiter's Decametric Emission, 1961," *Ap. J.*, 137, 41 (1963).
- Warwick, J.W., "Radio Emission from Jupiter," *Ann. Rev. Astron. Astrophys.*, 2, 1 (1964).
- Warwick, J.W., "Radiophysics of Jupiter," *Space Sci. Rev.*, 6, 841 (1967).
- Warwick, J.W., "Particles and Fields near Jupiter," NASA CR-1685, U.S. Government Printing Office, Washington, D.C., (1970).
- Warwick, J.W., Dulk, G.A., and Riddle, A.C., "Jupiter Radio Emission, January 1960--March 1975," Report PRA No. 3, Radio Astronomy Observatory of the University of Colorado (1975).
- Wilson, R.G., Warwick, J.W., and Libby, W.F., "Fifth Source of Jupiter Decametric Radiation," *Nature*, 220, 1215 (1968).
- Wu, C.S., Smith, R.A., and Zmuidzinas, J.S., "Theory of Decametric Radio Emissions from Jupiter," *Icarus*, 18, 192 (1973).

## BIOGRAPHICAL SKETCH

James Richard Thieman, son of Richard Frank and Agnes Marie Thieman, was born on August 8, 1947. During his first twenty-one years in Dayton, Ohio, he began his education at Holy Angels Grade School, continued through Chaminade High School, and graduated magna cum laude with a B.S. degree in physics from the University of Dayton. He served as president of the high school science club and of the University's chapter of the Society of Physics Students - Sigma Pi Sigma Honor Society.

He continued to pursue his interests in physics, astronomy, and computer science by taking up graduate studies in the Department of Physics and Astronomy at the University of Florida. He was supported at first as a graduate teaching assistant and later became a graduate research assistant. While in pursuit of the doctoral degree he had the good fortune of meeting Barbara Eve Brandes. They were married on September 29, 1973. She provided the encouragement necessary for successful culmination of this dissertation.



I certify that I have read this study and that in my opinion it conforms to acceptable standards of scholarly presentation and is fully adequate in scope and quality as a dissertation for the degree of Doctor of Philosophy.

Alex G. Smith

Alex G. Smith, Chairman  
Professor of Physics  
and Astronomy

I certify that I have read this study and that in my opinion it conforms to acceptable standards of scholarly presentation and is fully adequate in scope and quality as a dissertation for the degree of Doctor of Philosophy.

Thomas D. Carr

Thomas D. Carr  
Professor of Physics  
and Astronomy

I certify that I have read this study and that in my opinion it conforms to acceptable standards of scholarly presentation and is fully adequate in scope and quality as a dissertation for the degree of Doctor of Philosophy.

George R. Lebo

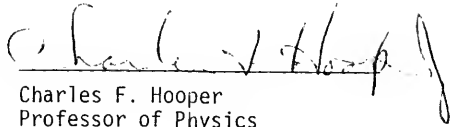
George R. Lebo  
Assistant Professor of Astronomy

I certify that I have read this study and that in my opinion it conforms to acceptable standards of scholarly presentation and is fully adequate in scope and quality as a dissertation for the degree of Doctor of Philosophy.

Stephen T. Gottesman

Stephen T. Gottesman  
Associate Professor of Astronomy

I certify that I have read this study and that in my opinion it conforms to acceptable standards of scholarly presentation and is fully adequate in scope and quality as a dissertation for the degree of Doctor of Philosophy.

  
Charles F. Hooper  
Professor of Physics

This dissertation was submitted to the Department of Physics and Astronomy in the College of Arts and Sciences and to the Graduate Council, and was accepted in partial fulfillment of the requirements for the degree of Doctor of Philosophy.

August, 1977

---

Harry H. Sisler, Dean  
Graduate School

UNIVERSITY OF FLORIDA



3 1262 08553 2959